75 2222

218p.

REPORT R-687 AUGUST, 1975 UILU-ENG 75-2222

CSL COORDINATED SCIENCE LABORATORY

MASTER COPY
Do Not Remove

DISCHARGE DYNAMICS OF THE AC PLASMA DISPLAY PANEL

LARRY FRANCIS WEBER

APPROVED FOR PUBLIC RELEASE. DISTRIBUTION UNLIMITED.

COLLEGE OF ENGINEERING DOCUMENTS OFFICE
UNIVERSITY OF ILLINOIS
112 ENGINEERING HALL
URBANA, ILLINOIS 61801

UNIVERSITY OF ILLINOIS – URBANA, ILLINOIS

SECURITY CLASSIFICATION OF THIS PAGE *(When Data Entered)*

REPORT DOCUMENTATION PAGE		READ INSTRUCTIONS BEFORE COMPLETING FORM
1. REPORT NUMBER	2. GOVT ACCESSION NO.	3. RECIPIENT'S CATALOG NUMBER
4. TITLE *(and Subtitle)* DISCHARGE DYNAMICS OF THE AC PLASMA DISPLAY PANEL		5. TYPE OF REPORT & PERIOD COVERED Technical Panel 6. PERFORMING ORG. REPORT NUMBER R-687; UILU-ENG 75-2222
7. AUTHOR(s) Larry Francis Weber		8. CONTRACT OR GRANT NUMBER(s) DAAB-07-72-C-0259;N00014-67-A-0305-0021;F30602-73-C-0370;DAAC-15-73-C-0077; NSF GK-21765
9. PERFORMING ORGANIZATION NAME AND ADDRESS Coordinated Science Laboratory University of Illinois at Urbana-Champaign Urbana, Illinois 61801		10. PROGRAM ELEMENT, PROJECT, TASK AREA & WORK UNIT NUMBERS
11. CONTROLLING OFFICE NAME AND ADDRESS Joint Services Electronics Program; Office of Naval Research; Rome Air Development Center; Army Research Office		12. REPORT DATE August, 1975 13. NUMBER OF PAGES 208
14. MONITORING AGENCY NAME & ADDRESS *(if different from Controlling Office)*		15. SECURITY CLASS. *(of this report)* UNCLASSIFIED 15a. DECLASSIFICATION/DOWNGRADING SCHEDULE

16. DISTRIBUTION STATEMENT *(of this Report)*

Approved for public release; distribution unlimited

17. DISTRIBUTION STATEMENT *(of the abstract entered in Block 20, if different from Report)*

18. SUPPLEMENTARY NOTES

19. KEY WORDS *(Continue on reverse side if necessary and identify by block number)*

Plasma Display
Gas Discharge Physics
Interferrometry

20. ABSTRACT *(Continue on reverse side if necessary and identify by block number)*

The AC plasma display panel is presently being sold by a number of large corporations and is satisfying a wide range of display applications. However most of its excellent characteristics have been achieved through empirical efforts. This thesis will present both theoretical and experimental results that begin to explain some of the detailed physical characteristics of this device.

DD FORM 1 JAN 73 1473 EDITION OF 1 NOV 65 IS OBSOLETE

SECURITY CLASSIFICATION OF THIS PAGE *(When Data Entered)*

UILU-ENG 75-2222

DISCHARGE DYNAMICS OF THE AC PLASMA DISPLAY PANEL

by

Larry Francis Weber

This work was supported in part by the Joint Services Electronics Program (U.S. Army, U.S. Navy and U.S. Air Force) under Contract DAAB-07-72-C-0259; Office of Naval Research under Contract N00014-67-A-0305-0021; Rome Air Development Center under Contract F30602-73-C-0370; U.S. Army under Contract DAAC-15-73-C-0077; and the National Science Foundation under Grant NSF GJ-31765.

Reproduction in whole or in part is permitted for any purpose of the United States Government.

Approved for public release. Distribution unlimited.

DISCHARGE DYNAMICS OF THE AC PLASMA DISPLAY PANEL

BY

LARRY FRANCIS WEBER

B.S., University of Illinois, 1969
M.S., University of Illinois, 1971

THESIS

Submitted in partial fulfillment of the requirements
for the degree of Doctor of Philosophy in Electrical Engineering
in the Graduate College of the
University of Illinois at Urbana-Champaign, 1975

Thesis Advisor: Professor Roger L. Johnson

Urbana, Illinois

DISCHARGE DYNAMICS OF THE AC PLASMA DISPLAY PANEL

Larry Francis Weber, Ph.D.
Coordinated Science Laboratory and
Department of Electrical Engineering
University of Illinois at Urbana-Champaign, 1975

The AC plasma display panel is presently being sold by a number of large corporations and is satisfying a wide range of display applications. However most of its excellent characteristics have been achieved through empirical efforts. This thesis will present both theoretical and experimental results that begin to explain some of the detailed physical characteristics of this device.

The theoretical effort is based on a one dimensional computer simulation of the discharge which includes calculation of the detailed electron dynamics and the effects of electric field distortion. The results show the existence of a plasma of density 10^{13} cm^{-3} that fills most of the discharge gap at the peak of the discharge current. This plasma lasts for many microseconds after the discharge peak.

Wall charge transfer curves are computed with the simulation and from these curves two physical effects that allow the plasma panel to exhibit memory are identified. One effect is strongly dependent on sustain voltage waveshape and the other is dependent on gas pressure.

Measurements are made of the capacitance variation and the microwave transmission of the plasma cell. These results verify the existence of the plasma predicted by the simulation, however they do not give the desired information about the plasma density. The plasma is shown to exist for periods as long as 100 microseconds. Significant changes in the sustain voltage cause the plasma to be swept out of the volume.

Attempts were made to measure the plasma density with optical interferometry. To accomplish this a very simple interferometer was developed that could routinely measure phase shifts smaller than 10^{-5} Å. These are believed to be the most sensitive optical phase change results ever published.

The optical plasma density measurements were not successful because of the large neutral atom density changes that caused index of refraction changes much greater than the anticipated electron density index change. However, much was learned about the neutral density variations. Sound waves that are initiated by the heating of the discharge activity in the cathode region were observed. These waves travel back and forth between the anode and the cathode for many microseconds after the discharge pulse. By measuring their velocity, one can determine the gas temperature. In a typical plasma cell with a standard gas mixture, the gas temperature of an on cell is only a few degrees centigrade above the off cell temperature.

ACKNOWLEDGEMENTS

Sincere appreciation goes to Professors Donald L. Bitzer, Roger L. Johnson and H. Gene Slottow for their continued encouragement, support and interest throughout the period of this study. Many others have contributed with useful discussions and technical assistance. They include Dr. Brij M. Arora, William J. Coates, Professor Joseph T. Verdeyen, Richard W. Blomme, Michael W. Walker and Robert K. Rader.

The assistance of a number of people was required for the completion of this work. Robert Baillie and Michael Ward wrote most of the necessary software. Jerry Sweeney set up and performed most of the microwave strip line experiments. Michael Marentic and Earl Payne built much of the equipment used in the other experiments.

I wish to thank the many members of the staff of the Coordinated Science Laboratory who contributed to the development of this research and to the preparation of this document.

TABLE OF CONTENTS

Chapter		Page
1	INTRODUCTION	1
2	COMPUTER SIMULATION	7
	2.1 Introduction	7
	2.2 Review of Previous Calculations	7
	2.3 Details of Calculations Presented Here	10
	2.4 Characterization of a Typical Discharge	21
3	THE EFFECTS OF PRESSURE AND SUSTAIN WAVEFORM ON THE CHARGE TRANSFER CURVE AND MEMORY	47
	3.1 Introduction	47
	3.2 Basic Charge Transfer Curve Theory	47
	3.3 Charge Transfer Curve Calculations	53
	3.3.1 Case of Square Wave Sustainer with No Field Distortion	55
	3.3.2 Case of Non-Square Wave Sustainer without Field Distortion	59
	3.3.2.1 Discussion of Mechanisms Causing the First Memory Effect	65
	3.3.3 Case of Square Wave Sustainer with Field Distortion	79
	3.3.3.1 Explanation of Second Memory Mechanism	79
	3.3.4 Case of Non-Square Wave with Field Distortion	87
	3.4 Comparison of These Results to Those of Others	87
	3.5 Experimental Results	97
4	PLASMA DENSITY MEASUREMENTS USING RF AND MICROWAVE TECHNIQUES	103
	4.1 Introduction	103
	4.2 RF Capacitance Measurements	103
	4.2.1 Resonance Technique	107
	4.2.2 Stub Technique	112
	4.3 Induced Plasma Decay Phenomena	116
	4.4 Microwave Measurements	121
	4.4.1 Experimental Technique	122
	4.4.2 Experimental Results	126
	4.5 Significance of the Existence of Plasma	131
5	A VERY SENSITIVE LASER INTERFEROMETRY SYSTEM	139
	5.1 Introduction	139
	5.2 Resolution Requirements	139

Chapter Page

5.3 Details of Interferometry System.....141
5.4 Sensitivity Tests.....153
5.5 Excess Noise.....156
5.6 Potential Improvements.....165
5.7 Conclusion.....166

6 OPTICAL INDEX OF REFRACTION MEASUREMENTS.....168

6.1 Introduction.....168
6.2 Experimental Cell Dimensions.....168
6.3 Cell Construction.....171
6.4 Cell Positioning in the Interferometer.....173
6.5 Experimental Results.....174
6.6 Neutral Density Measurements.....179
6.7 Neutral Temperature Measurements.....186
6.8 Electron Density Measurement.....190

7 CONCLUSION.....199

REFERENCES.....204

VITA.....208

CHAPTER 1

INTRODUCTION

The AC plasma display panel is now being used in a wide range of display applications. Devices are presently being sold in a variety of sizes and shapes that range from the large quarter million cell graphic display panels used by the PLATO system down to small 7 segment numeric digits used in digital clocks. The list of corporations presently marketing these devices continues to grow and presently includes IBM, Owens-Illinois, Fujitsu and Varian. Others, having significant research programs, include Control Data, Bell Labs and Burroughs.

The larger panels are having a major impact in the area of computer graphics. A list of advantages over the CRT includes: high brightness, high contrast ratio, no spatial distortion, long lifetime, inherent memory, no flicker and digital addressing. An example of the quality of this display can be seen in many of the figures in Chapters 2 and 3 of this thesis.

The basic panel design used for large displays is shown in Figure 1.1 [1]. A key feature of the AC plasma panel is that the electrodes are insulated from the gas by a suitable dielectric, which in most cases is glass [2]. Thus, in order to drive the panel an AC voltage is required. The glass dielectric serves two very useful purposes. It limits the current of the gas discharge and thus prevents a disastrous arc. The dielectric thus replaces the current limiting resistor necessary for a DC gas discharge. The second benefit is that it can be used to store charge. This charge can be used to keep the display cell in an on or off state and thus allow the AC plasma panel to have inherent memory [3].

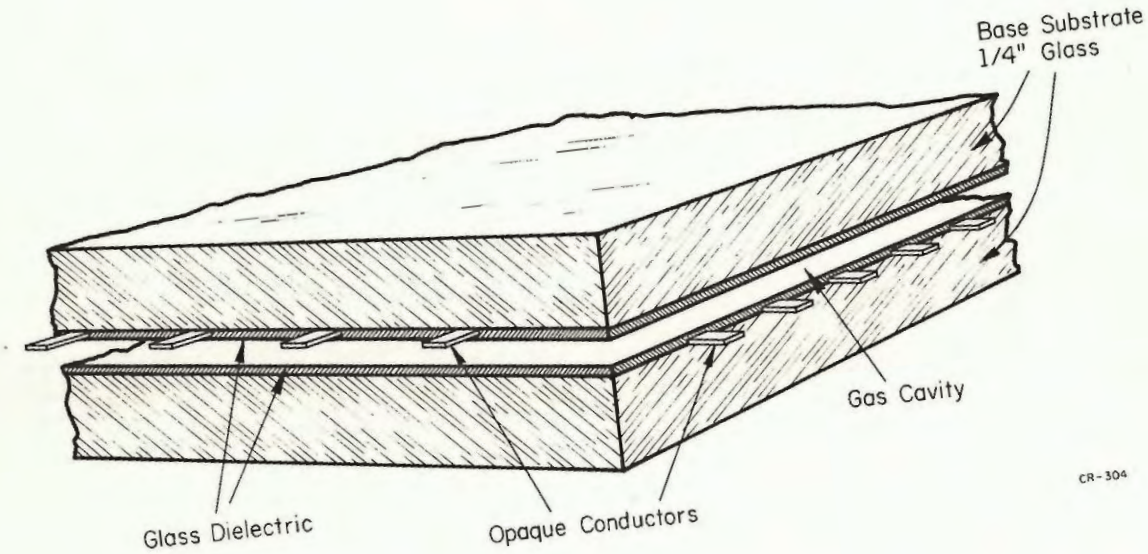

Figure 1.1. Basic design for large AC plasma display panels. The glass dielectric is typically 25 μm thick and the gas cavity is about 100 μm thick.

Figure 1.2 shows the typical electronic operation of this device [4]. The AC sustain voltage is applied constantly to all cells in a panel. Depending on its previous history each cell is either on or off. The on cells emit light pulses as shown. The voltage component associated with charge on the dielectric is commonly called the wall voltage. Its behavior depends on the state of the cell and is shown in Figure 1.2. A cell will be on if sufficient wall voltage exists so that the addition of the wall voltage and the sustain voltage across the gas is sufficient to cause a gas discharge. An off cell will have zero wall voltage. The amplitude of the sustain voltage alone must be insufficient to cause a discharge. A cell is turned on or off by adding appropriate address pulses to the sustain voltage in such a way as to cause a discharge that will bring the wall voltage to the desired level.

The above theory has been understood since the invention of the device. This theory has not been successful at prescribing how to design plasma display systems. Things such as gas mixture, cell geometry, and sustain voltage waveforms have all been derived empirically with little or no guidance from theory. Thus a more complete theory of operation is badly needed for the AC plasma display panel.

Unfortunately, there has been very little experimental work published on the device physics. Few advances have been made beyond the early works of Wilson [5] and Arora [6]. One reason for this is that this device has a very small anode-cathode gap spacing of about 100 μm. This makes it very difficult to apply conventional plasma diagnostic techniques such as microwave transmission or electric probes. Another complexity is the fact

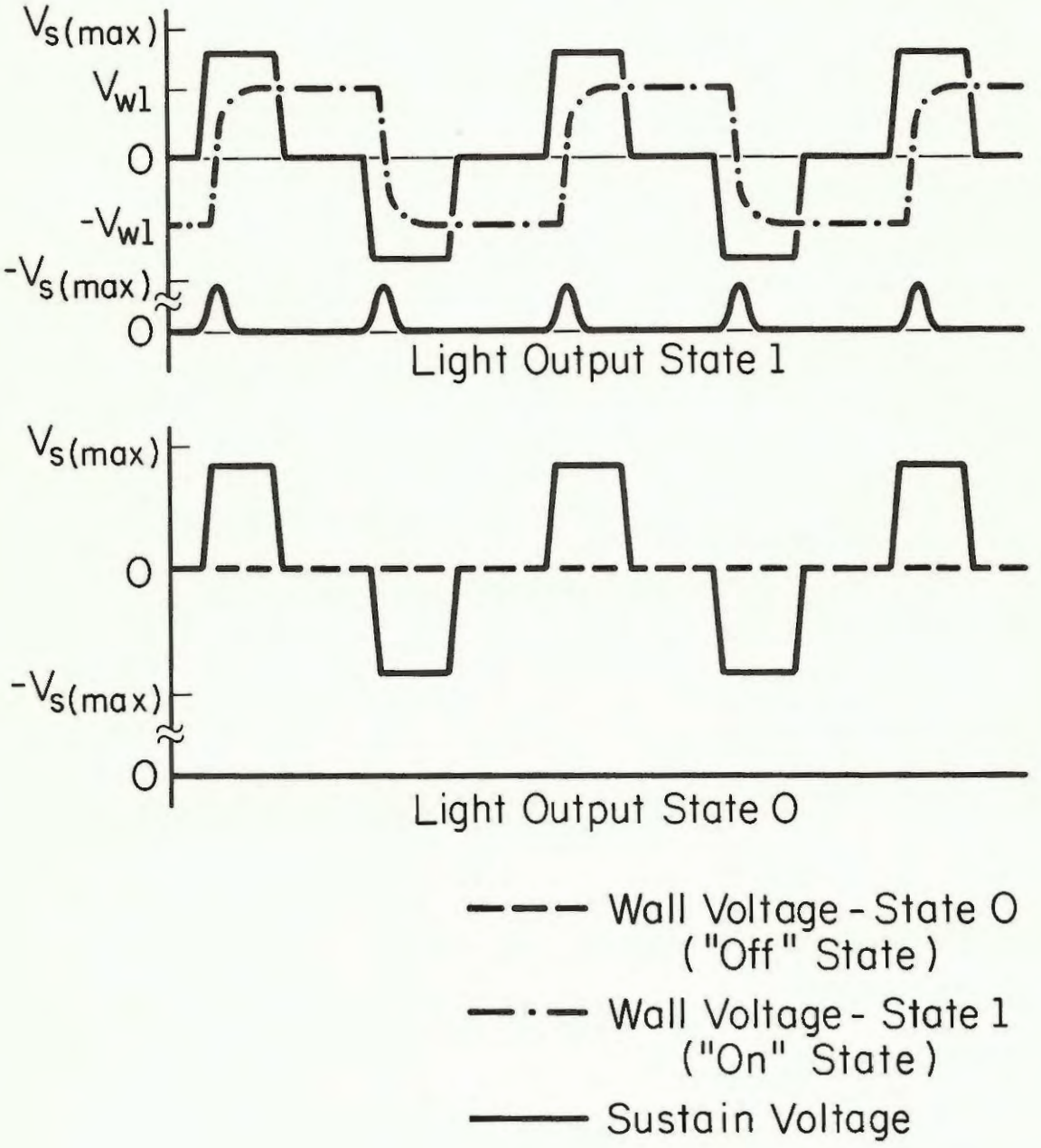

Figure 1.2. Voltage waveforms for cells in the on and the off state.

that the voltage across the gap is continually changing and is not directly measurable. This means that a steady state situation is never reached. This type of discharge fits between the well-known DC steady state discharge and the well-known RF AC discharge where wall effects are not important. A further complication is the fact that the cathode material used in this discharge is a dielectric and very few dielectrics have been studied for their cathode properties.

The purpose of this thesis is to provide a better understanding of the important physical process involved in the plasma panel gas discharge. It can be divided into 2 major parts: theoretical studies covered in Chapters 2 and 3, and experimental studies covered in Chapters 4, 5 and 6. A computer simulation based on simple Townsend gas discharge theory is used to gain insight to the nature of the discharge. The simulation is then used to present some major theoretical results concerning the electrical characteristic of the device. The simulation shows the existence of two mechanisms that allow this device to exhibit memory characteristics.

The experimental studies attempt to measure various physical quantities in the plasma panel. In the past only two quantities have been measured: discharge current and light output. Chapter 4 deals with measurements of the RF capacitance of this device. Also the microwave transmission properties are measured. Both of these measurements show the existence of a long lived plasma that remains in the gas volume for long periods after the end of the discharge current pulse. The existence of this plasma has important consequences for the operation of the device.

Chapters 5 and 6 deal with the measuring of the index of refraction of the gas volume. A spinoff of this research was the development of a very simple interferometry system capable of measuring optical phase changes smaller than 10^{-5} Å. Because of its importance to researchers in other areas, Chapter 5 is devoted to a discussion of this technique. Chapter 6 presents the results of index of refraction measurements on the gas volume of a plasma cell.

CHAPTER 2

COMPUTER SIMULATION

2.1 Introduction

In this study a digital computer was used to model a one dimensional plasma display cell. The basic philosophy of these calculations is to use them as a qualitative guide to the simple physical processes in a plasma display panel. For this reason, all calculations presented here will deal with only two particle species - ions and electrons. However, because of its importance, the field distortion due to the electrons and ions in the gas volume will be carefully calculated.

This chapter will present a review of the works of others and the details of the calculational technique presented here. Also the characteristics of a typical discharge are discussed. In Chapter 3 the calculational technique will be used to explain why this device has memory.

2.2 Review of Previous Calculations

Before the details of these calculations are presented, it is worthwhile to discuss the works of others. Verone and Wang [7] published the first calculations of a plasma display panel discharge. The results were for a single discharge in pure Neon gas, a 200 kHz sine wave sustain waveform, and what is commonly referred to as the U of I panel geometry which is now considered obsolete. Their calculations used a finite difference technique developed extensively by Ward [8,9,10,11,12].

This technique is very costly in terms of computer time. On a high speed computer this single discharge cycle took as much as 15 minutes

CPU time. This long time is basically due to convergence, criteria of finite difference techniques. The solution is obtained by dividing space into 15 mesh points and then dividing time into small steps. Values are calculated for all electron and ion densities for each mesh point for a particular time. Time is then incremented by one time step and again the calculations are made. The amount of CPU time needed for a given discharge time depends heavily on the size of the time step needed for a convergent solution. Ideally this time step, or Δt, should be infinitely small. For the obvious practical reasons it is made as large as possible. It can be shown [12] that the finite difference technique used here converges as long as Δt is smaller than the time for the electrons to get from one mesh point to the next. In plasma panel calculations Δt is typically 10^{-11} sec. Thus to calculate what happens in the plasma panel for one microsecond takes about 10^5 iterations. In each iteration the values of the ion and electron densities must be calculated for each mesh point. Thus it is clear that Ward's technique is very expensive to implement if a large number of discharge cycles is desired. Unfortunately, the nature of the plasma display panel necessitates calculating a long series of discharges due to the strong influence of one discharge on the following discharges in a sequence. Thus all other calculations discussed below do not use Ward's technique because of CPU time limitations.

Lay, Chu and Haberland [13] have done calculations of long series of discharges in plasma display cells. Unfortunately, they disregard the effects of electric field distortion. On the other hand, they include the effects of Neon metastables in a Penning mixture of Ne + Ar. To make the

calculations run at reasonable CPU times, they choose the time step Δt just shorter than the ion transit time between mesh points [12]. Since the ions travel at a much slower velocity than electrons, this technique runs by a factor of 10^2 to 10^3 faster. Unfortunately, this technique neglects all details of the electron motion in the discharge process.

Unlike Verone and Wang, Lay et al. clearly show that their discharge sequences have memory. The correct way to demonstrate memory is to run a series of sustain voltage pulses and show that the wall voltage can stabilize to both an on state and an off state, depending on the initial value of wall voltage. Since only one discharge is presented, one cannot tell if Verone and Wang's model has memory. Unfortunately, Lay et al.'s results cannot be viewed as accurate solutions because they neglect field distortion and the detailed effects of the electrons.

The work of Lanza [14] should be viewed with much greater interest. In this case, the effects of electric field distortion are included. Also the details of the electrons are not neglected. A very clever calculational technique is used that uses a Δt somewhere between the electron transit time and ion transit time. Thus Lanza's calculations are faster than Verone and Wang's but slower than Lay et al.'s. To determine the details of the electron motion across the gap, Lanza uses a novel estimation scheme that divides the gap into three regions that each have separate electron density calculational algorithms. He shows excellent agreement between his calculations and experimental values. In fact, this agreement is almost too good, in light of the many approximations needed for the calculations. He is the first to show the existence of a weak plasma region near the anode for a fraction of a microsecond close to the peak of the discharge current. He does not show

any series of discharges and thus it is not possible to show whether this technique has memory. In fact it is difficult to say whether this technique yields the correct solution. If it does, it is a very exciting way of decreasing the CPU time. However comparisons made later on in this thesis seem to indicate that it does not give the same solution as the more rigorous technique of Ward.

The most recent published work is that of Lanza et al. [15] in which they extend Lanza's original work to include not only the effects of neon ions and electrons, but other species including neon metastable states, neon imprisoned states, and Ne^+, Ar^+ and Ne_2^+, ion species. With the addition of all of these new species the calculational time is greatly increased to the point that it is almost equivalent to that required by Verone and Wang.

The calculational philosophy of Lanza et al. is considerably different than the philosophy taken in the techniques described below. They are trying to include as many known physical effects as is calculationally possible in order to achieve an exact simulation. The approach taken below uses a very simple model and attempts to learn all that it teaches. After the simple model is understood, then the perturbations of various other species in the discharge should be included.

2.3 Details of Calculations Presented Here

The calculational technique chosen here is the finite difference technique of Ward. These calculations are performed over a much wider range of cases than presented by Verone and Wang. The computer used is a CDC cyber 73 (6500) that is principally used by the PLATO computer-based

education system. This job was run in a background mode which would allow it a number of CPU hours each day. The calculations presented below represent a $2\frac{1}{2}$ year study involving more than 2000 hours of CPU time.

Although the exact calculational technique has been presented many times [7,8,9,10,11,12], a summary of the technique used here will be presented as a convenience.

In one dimension, the three basic equations to be solved are: the electron continuity equation

$$\frac{\partial n_e}{\partial t} = \alpha n_e V_e - \frac{\partial}{\partial x}(n_e V_e) \tag{2.1}$$

which states that the rate of change of electron density at a point in space $(\frac{\partial n_e}{\partial t})$ is equal to the rate of electron generation $(\alpha n_e V_e)$ plus the rate of the electrons coming in minus the rate of electrons going out of that point $(-\frac{\partial}{\partial x}(n_e V_e))$. Similarly the ion continuity equation is

$$\frac{\partial n_i}{\partial t} = \alpha n_e V_e + \frac{\partial}{\partial x}(n_i V_i) \tag{2.2}$$

where n_e is the electron number density, n_i is the ion number density, V_e is the electron velocity, V_i is the ion velocity, α is the Townsend coefficient that describes the number of electrons freed by the avalanche process per unit length, x is space, and t is time. The variables n_e, n_i, V_e, V_i, and α are all functions of both x and t. The variables V_e, V_i, and α are characteristic of the gas and are directly dependent on the value of the electric field E(x,t) which must be found from Poisson's equation:

$$\frac{\partial E}{\partial x} = \frac{q}{\epsilon_o} (n_i - n_e) \tag{2.3}$$

where q is the charge of the electron and ϵ_o is the dielectric constant of free space.

From the above three equations and knowledge of the functional relationship of V_e, V_i, and α on E, one can find the desired solution which is n_e and n_i for all values of space and time if the necessary boundary conditions and initial conditions are specified. In a gas discharge a number of physical effects can occur at the cathode that will define the cathode boundary conditions. If we define an electron current density $j_e(x,t) = n_e(x,t) \cdot V_e(x,t)$, then this cathode boundary condition is specified by the electron current from the cathode

$$j_e(0,t) = j_o + \gamma_i j_i(0,t) + \frac{\gamma_p}{d} \int_0^d \sigma(x,t)\ j_e(x,t)\ dx \tag{2.4}$$

where j_o is a very small constant current emitted from the cathode to get the discharge process started, $j_i(0,t)$ is the ion current at the cathode, γ_i and γ_p are the Townsend coefficients for electrons emitted from the cathode due to ion bombardment and photon bombardment respectively, d is the distance between the cathode and the anode and $\sigma(x,t)$ is a function that defines the number of photons per unit distance created in an avalanche by an electron. The value of $\sigma(x,t)$ is determined from $E(x,t)$ in much the same manner as is $\alpha(x,t)$. γ_i, γ_p and d are constants that characterize the discharge.

Since ions are not allowed to be emitted by the anode a further boundary condition is:

$$j_i(d,t) = 0 \tag{2.5}$$

To determine the boundary conditions for E(x,t), we must use Kirkhoff's voltage law and sum around the loop shown in Figure 2.1 that includes the plasma display cell and the applied voltage source (sustainer). The loop equation is

$$V_s = E_c \ell + E_a \ell + E_o d + \frac{q}{\epsilon_o} \int_0^d \int_0^{x'} (n_e - n_i)\, dx dx' \tag{2.6}$$

where E_c and E_a are the fields in the dielectric layers at the cathode and the anode, ℓ is the thickness of these dielectric layers, q is the charge of the electron, and E_o is the field in the gas volume at x=0. To find the values of the fields in the dielectric, E_c and E_a, one must know the value of the charges Q_o and Q_d at the dielectric gas interfaces. From the standard electric field boundary conditions one gets

$$\epsilon_r E_c - E_o = \frac{Q_o}{\epsilon_o} \tag{2.7}$$

and

$$E_d - \epsilon_r E_a = \frac{Q_d}{\epsilon_o} \tag{2.8}$$

where ϵ_r is the relative dielectric constant of the dielectric layers and E_d is the electric field in the gas volume at x=d.

The charges Q_o and Q_d are obtained by integrating all currents flowing into and out of the cathode and anode.

For initial conditions one must specify $n_e(x,0)$, $n_i(x,0)$, $Q_o(t=0)$, and $Q_d(t=0)$. The sustain voltage V_s is the desired function of time.

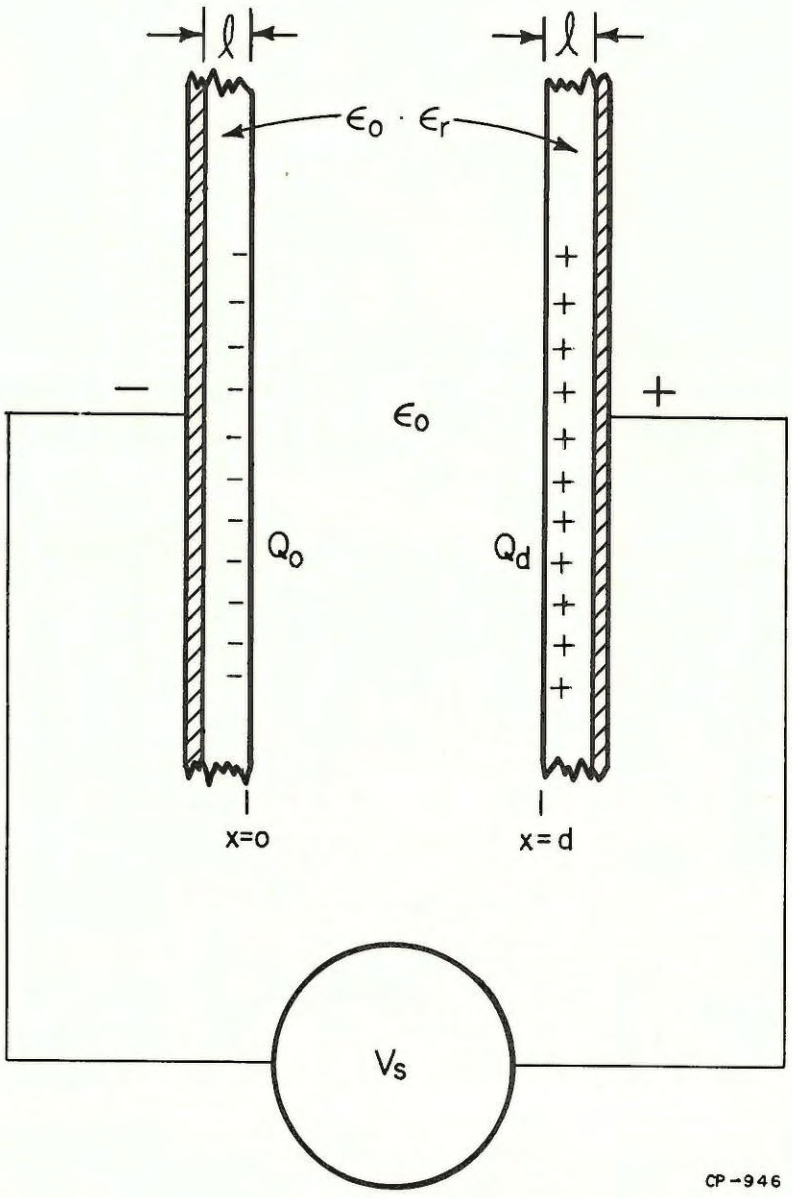

Figure 2.1. Cell geometry used in one dimensional computer simulation.

The gas parameters are those given by Ward [8]. The dependence of α, V_e, and V_i on the E field is

$$\alpha = pA \exp[-B(p/E)^{\frac{1}{2}}] \tag{2.9}$$

where p is the gas pressure and A and B are constants characteristic of the gas. Also,

$$V_e = \frac{\mu_- E}{p} \tag{2.10}$$

where μ_- is the electron mobility. For ions,

$$V_i = \frac{\mu_+ E}{p}\left(1 - \frac{CE}{p}\right), \quad E/p \leq W_1 \tag{2.11 a}$$

$$V_i = \frac{k_+ E^{\frac{1}{2}}}{p^{\frac{1}{2}}}\left(1 - DE^{-3/2}p^{3/2}\right), \quad E/p > W_1 \tag{2.11 b}$$

where μ_+, k_+, C, D, and W_1 are constants characteristic of the gas. Ward [8] gives values of these constants for various gases. Pure Ne was used and has the following constants:

$A = 8.2 \text{ cm}^{-1} \text{ torr}^{-1}$

$B = 17.0 \text{ volt}^{\frac{1}{2}} \text{ cm}^{-\frac{1}{2}} \text{ torr}^{-\frac{1}{2}}$

$C = 6 \times 10^{-3} \text{ torr cm volt}^{-1}$

$D = 41.98 \text{ volt}^{3/2} \text{ cm}^{-3/2} \text{ torr}^{-3/2}$

$\mu_- = 10^6 \text{ cm}^2 \text{ torr volt}^{-1} \text{ sec}^{-1}$

$\mu_+ = 2.9 \times 10^3 \text{ cm}^2 \text{ torr volt}^{-1} \text{ sec}^{-1}$

$k_+ = 1.7 \times 10^4 \text{ cm}^{3/2} \text{ torr}^{\frac{1}{2}} \text{ volt}^{-\frac{1}{2}} \text{ sec}^{-1}$

$W_1 = 35 \text{ volt cm}^{-1} \text{ torr}^{-1}$

In finite difference calculations, each iteration produces a solution advanced by a time increment Δt. This value is chosen from a convergence criteria [12]:

$$\frac{\Delta t}{\Delta x} < \max\left|V_e(x,t)\right|_x \tag{2.12}$$

where Δx is the distance between mesh points. This relation simply states that one must calculate the next iteration before the fastest electrons have time to get from one mesh point to the next. Failure to obey (2.12) causes the calculation to blow up. For 30 mesh points across the discharge gap used here and for typical plasma panel conditions, Δt is about 10 ps. Thus for 1 μs of plasma panel data, the following sequence is iterated 10^5 times.

1. Given the initial values of Q_o, Q_d, $V_s(t)$, $n_e(x,t)$, $n_i(x,t)$, calculate $E(x,t)$ for all x from (2.3), (2.6), (2.7), and (2.8).
2. Calculate $V_e(x,t) = \frac{\mu_-}{p} E(x,t)$ for all x.
3. Calculate $j_e(x,t) = V_e(x,t)\, n_e(x,t)$ for all x.
4. Calculate $V_i(x,t)$ for all x from (2.11).
5. Calculate $j_i(x,t)\, n_i(x,t)$ for all x.
6. Determine $\Delta t = \frac{0.9 \cdot \Delta x}{\max\left|V_e(x,t)\right|_x}$.
7. Calculate $t = t + \Delta t$.
8. Calculate $n_e(x,t)$ from a difference equation derived from (2.1) with the aid of (2.4) for all x.
9. Calculate $n_i(x,t)$ from a difference equation derived from (2.2).

10. Calculate $Q_o = Q_o + \Delta t \cdot j_i(0,t)$

$$Q_x = Q_x - \Delta t \cdot j_e(d,t)$$

11. Return to step 1.

A number of different panel geometries, gases, and glass surface coefficients were used in these studies. However most of the calculations were performed on one set of conditions in order to fully understand the effects of voltage waveform and gas pressure on the discharge properties. The one dimensional panel geometry was chosen to conform approximately with Owens-Illinois Digivue Panels [1]. Referring to Figure 2.1,

$$d = .015 \text{ cm}$$

$$\ell = .0025 \text{ cm}$$

and

$$\epsilon_r = 14 .$$

Equation (2.9) with constants for pure neon was consistently used. It is well known that the typical gas mixture used in plasma panels is neon plus small admixtures of other inert gases. In this model, the complication of the additional ion species introduced by the admixed gases was not desired. Thus the single gas data was used without complications such as the Penning effect.

The properties of the glass surface are very important to the operation of this device. However, very little is known about how glass dielectrics behave as gas discharge cathodes. The two physical effects included in the calculational technique by means of equation (2.4) are ejection of electrons from the glass by ion and by photon bombardment.

From experiments performed by this author, the ion effect is believed to be stronger. Thus, for simplicity, the photon effect was assumed to be negligible. In the calculations presented here

$$\gamma_i = 0.16$$

and

$$\gamma_p = 0 \quad .$$

Thus the third term in equation (2.4) was not calculated. The small external current needed to initiate discharge activity was usually arbitrarily chosen at about

$$j_o = 10^{-8} \text{ Amps} \cdot \text{cm}^{-2} \quad .$$

All sustain voltage rise and fall times were set at 100 ns. One half sustain period was typically set at 3 μsec. This is shorter than the 10 μs half period used in typical panels and was arrived at in an effort to reduce the CPU time per discharge. It is justified since only qualitative results are desired for this model.

A series of discharges was initiated with the desired value of wall charge and zero charge in the volume. The sustain voltage was then applied so as to give the proper electric field polarity. When the electric field reversed due to the fall of the sustain pulse, the problem was inverted in space so that the electric field would again have the original polarity. In this way long series of discharges could be run with the remaining wall charge, ion densities and electron densities of the last discharge automatically becoming the initial conditions of the present discharge.

A key feature of this calculational effort was the use of a PLATO terminal having a plasma display panel to present the results. More effort was spent in writing programs for displaying the information that was spent for programming the calculational routines. Figure 2.2 shows the options page in the PLATO lesson that is used to display the calculated data. Calculations are usually performed on a particular discharge sequence for a few days and stored on disk. Then the results are interpreted by viewing the various display options labeled in Figure 2.2. The ability to quickly review any portion of the calculated data in virtually any form desired has eliminated the many tedious aspects of data collection. Thus much more data can be reviewed and the patterns in the solution can be more easily and quickly recognized. Most of the results and understandings achieved through these calculations would not have been realized without these displays. When a human is forced to sift through reams of computer printout to get the numbers he wishes to plot in order to get the achieved results, the tendency will usually be to examine only a small amount of the data. Thus the effort spent on these displays was well worth it.

Most of the data presented here is taken directly off of the plasma display panel. Data is plotted as functions of both space and time. Although data was calculated for 30 points in space and for about every 10^{-11} seconds in time, it is impractical to store and display all of this data. Usually only 15 points in space and time steps of 10^{-7} seconds were displayed. In some cases, where the data changes abruptly, this can cause significant errors, but most of the time it worked quite well. Straight lines were drawn between all of the plotted points which usually gave a smooth curve appearance in all cases except those where changes occurred abruptly.

1 Common Variables
2 J(t) -- Current Density
3 $Q_a(t)$ and $Q_c(t)$ -- Wall Charges
4 E(x,t) -- Electric Fields
5 $q_+(x,t)$ -- Positive Ion Charge Density
6 $q_-(x,t)$ -- Electron Charge Density
7 $J(\alpha)$ vs $(Q_a(\alpha)-Q_c(\alpha))$ -- I-V Characteristic
8 Cell Wall Voltage and Cell Applied Voltage
9 Log(J(t)) -- Log of Current Density
a $j_-(x,t)$ -- Electron Current Density
b Log (abs($j_-(x,t)$))
c $j_+(x,t)$ -- Ion Current Density
d Log (abs($j_+(x,t)$))
e Light
f Log(Light)
g Transfer curve
h $\mu(t)$
i log(E(x,t))

Figure 2.2. Option page seen on PLATO terminal, used for selecting displays of computer simulation data.

2.4 Characterization of a Typical Discharge

There are, in general, two classes of results obtained from these calculations. The first is an estimation of the magnitudes of variables such as electron and ion densities, electric field intensities, and wall charges. Since these quantities have not been measured, these calculations can provide considerable insight into their magnitudes. The results presented by all previous authors mentioned above fit into this category. The second class of results attempts to explain the electrical characteristics of the panel in terms of the simple Townsend gas discharge theory. Central to these results is the question of why this device has memory. There has been no complete explanation of this question to date. The results of these calculations have shown the existence of two memory mechanisms in AC plasma display panels. This will be discussed in Chapter 3.

In this chapter, a typical discharge has been selected from a long stable sequence that has been shown to be operating within the bi-stable region. A square wave sustain voltage is applied. The pressure is 500 torr. Figure 2.3 shows the discharge current and applied sustain voltage. Discharge currents typically peak at $\sim$ 1 A/cm^2 which is close to experimentally measured values. Figure 2.4 shows the wall charge as a function of the same time interval. The charge for both the anode and the cathode are shown since they are typically not equal during the discharge. It should be remembered that these calculations solve only the one dimensional problem so that the units of current and charge should be A/cm^2, and C/cm^2. More useful to the device engineers is the plot of wall voltage and sustain voltage shown in Figure 2.5. The wall voltage is similar to, and directly

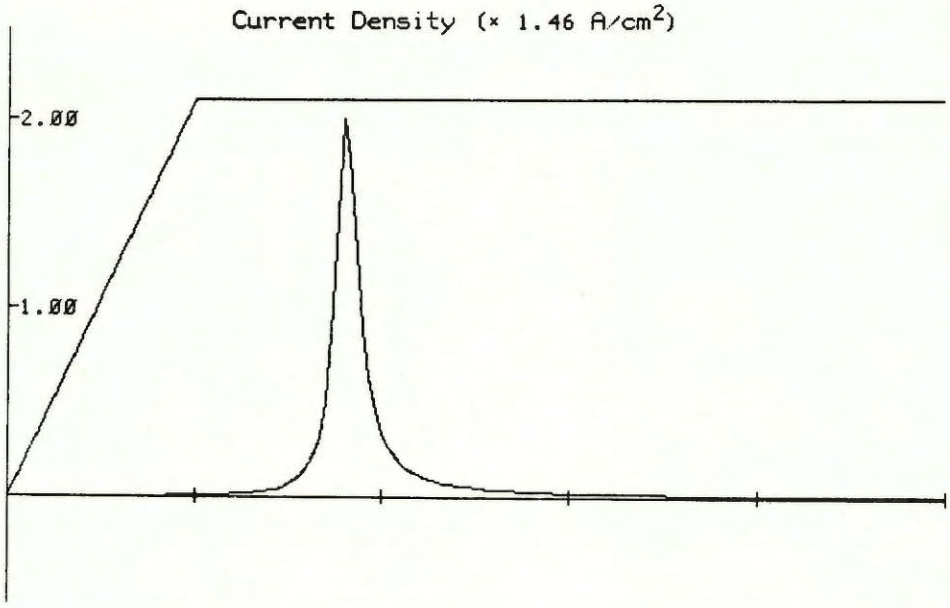

Figure 2.3. Discharge current and applied sustain voltage as a function of time for a typical discharge. Each vertical division is scaled at 1.46 A/cm^2 and 100 volts. The horizontal divisions are 100 ns.

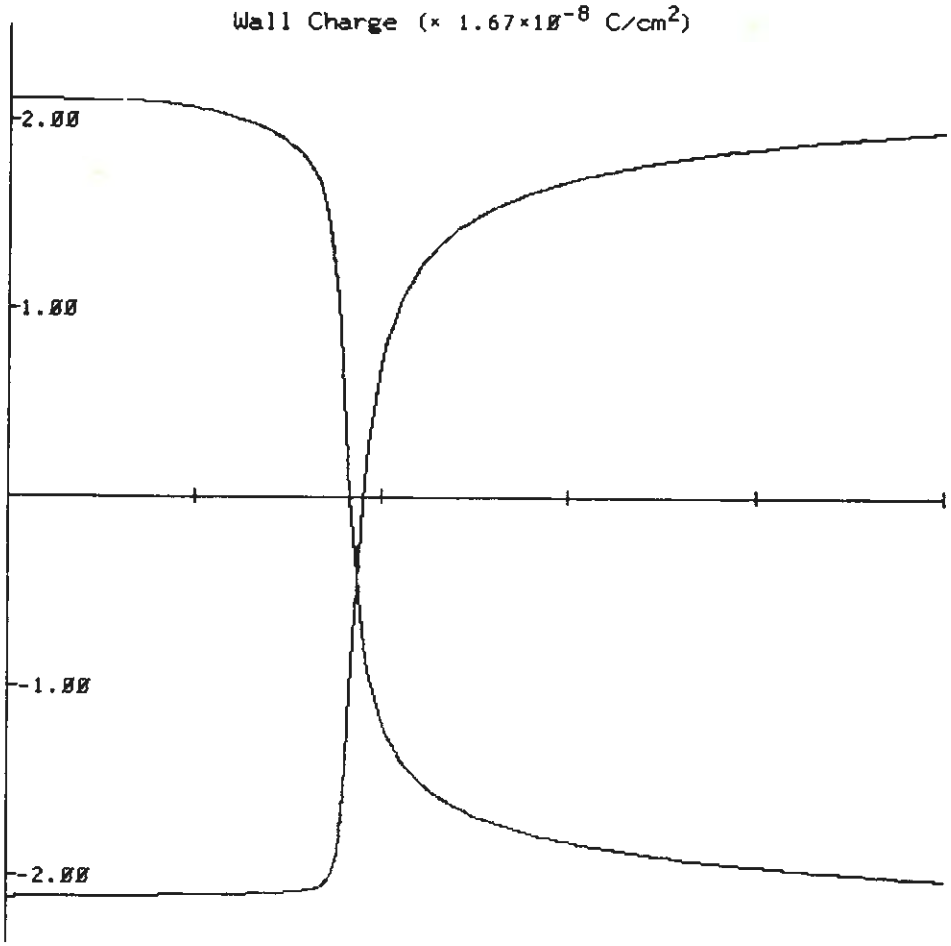

Figure 2.4. Wall charge for both the cathode and the anode. The vertical scale is 1.67 x 10-8 C/cm^2. Horizontal scale is the same as in Figure 2.3.

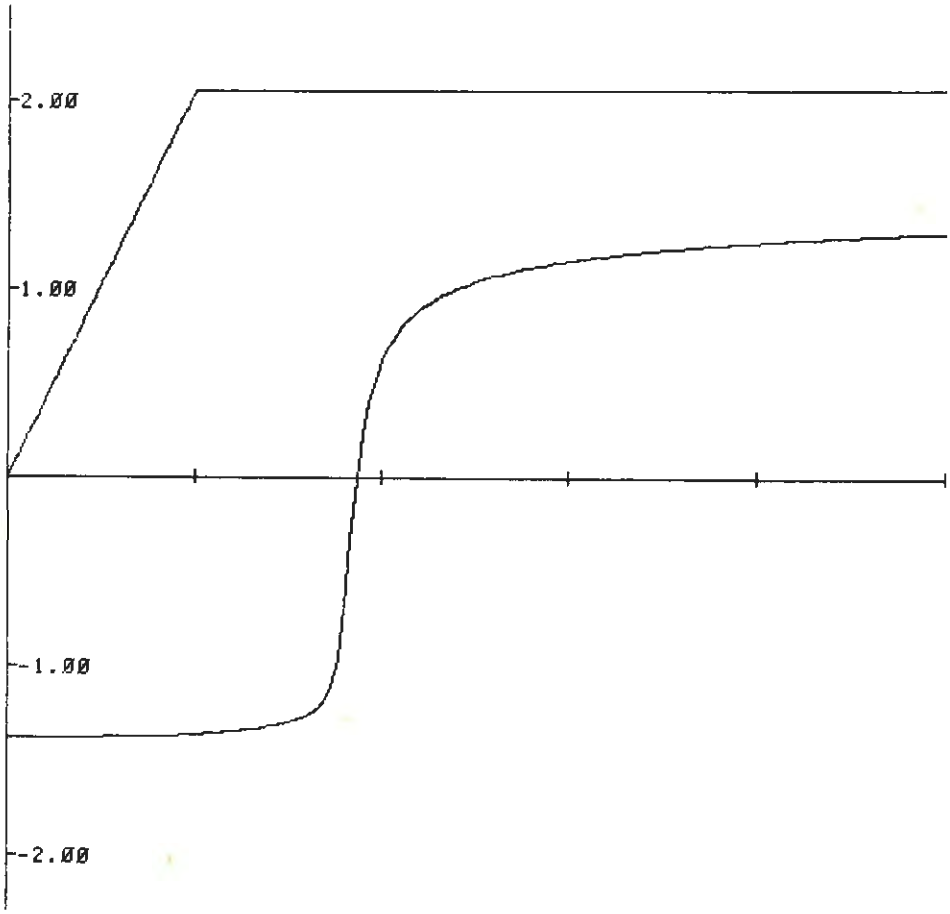

Figure 2.5. Wall voltage and sustain voltage component. The distance between these two curves represents the voltage across the gas. Vertical scale is 100 volts per division. The horizontal is 100 ns/division.

calculated from, the wall charge shown in Figure 2.4. The wall voltage typically does not rise to much greater than 70% of the sustain voltage as shown in Figure 2.5.

The data presented in the last three figures is qualitatively identical to all data presented by other authors. There is a sharp departure between these calculations and those of others with respect to the electron and ion densities, and electric fields shown in Figures 2.6 through 2.11. These figures show these three quantities as functions of space and time. The distance between the cathode and the anode is plotted along the horizontal axis. In these figures the cathode is on the left. Time should be plotted on a third axis, which on these figures is normal to the paper. Thus the various lines in these figures represent solutions for succeeding time steps. The solutions are labeled with sequence numbers that increase as time advances. Sequence number 1 corresponds to time zero in Figures 2.3, 2.4 and 2.5. Figures 2.6, 2.7 and 2.8 show data from time zero to the peak of the discharge current seen in Figure 2.3. Each curve is separated by a time step of 10 ns. Figures 2.9, 2.10 and 2.11 show the decay of the discharge starting from the current peak. For this data the time step is 33.3 ns. It should be remembered that some of the effects seen in these figures, where the values change abruptly in space, are due to the fact that only 15 spatial points are actually presented and straight lines connect all of these points.

Of major significance is the fact that the electron and ion densities grow to the peak value of about 10^{-6} C/cm^3. At the peak of the discharge, the gap is almost completely filled with ions and electrons of equal density. The field in this region is also very small. Thus the

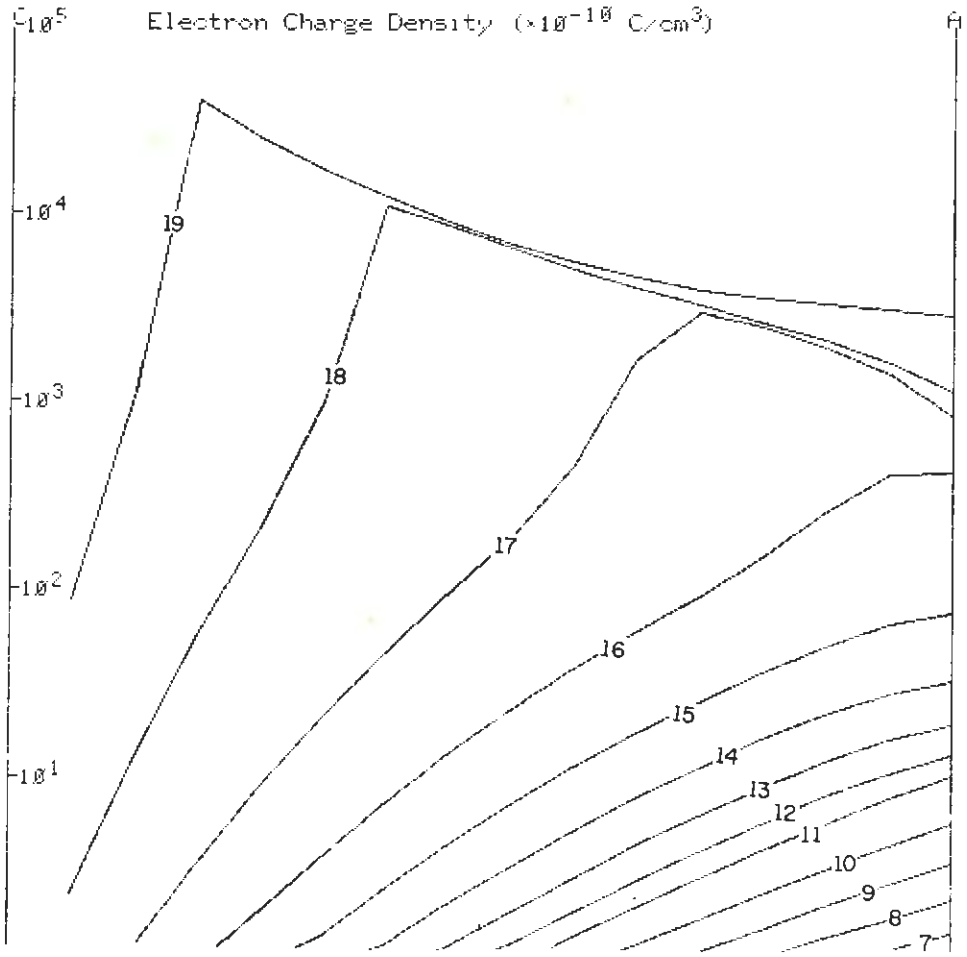

Figure 2.6. Electron charge density for space and time during the growth of the discharge shown in Figure 2.3. The vertical scale is a log scale with the origin corresponding to 10^{-10} C/cm^3. Thus the points along the 10^4 scale mark correspond to 10^{-6} C/cm^3. The horizontal scale is the space between the cathode and anode. The cathode is on the left. This density is plotted as time advances for every 10 ns.

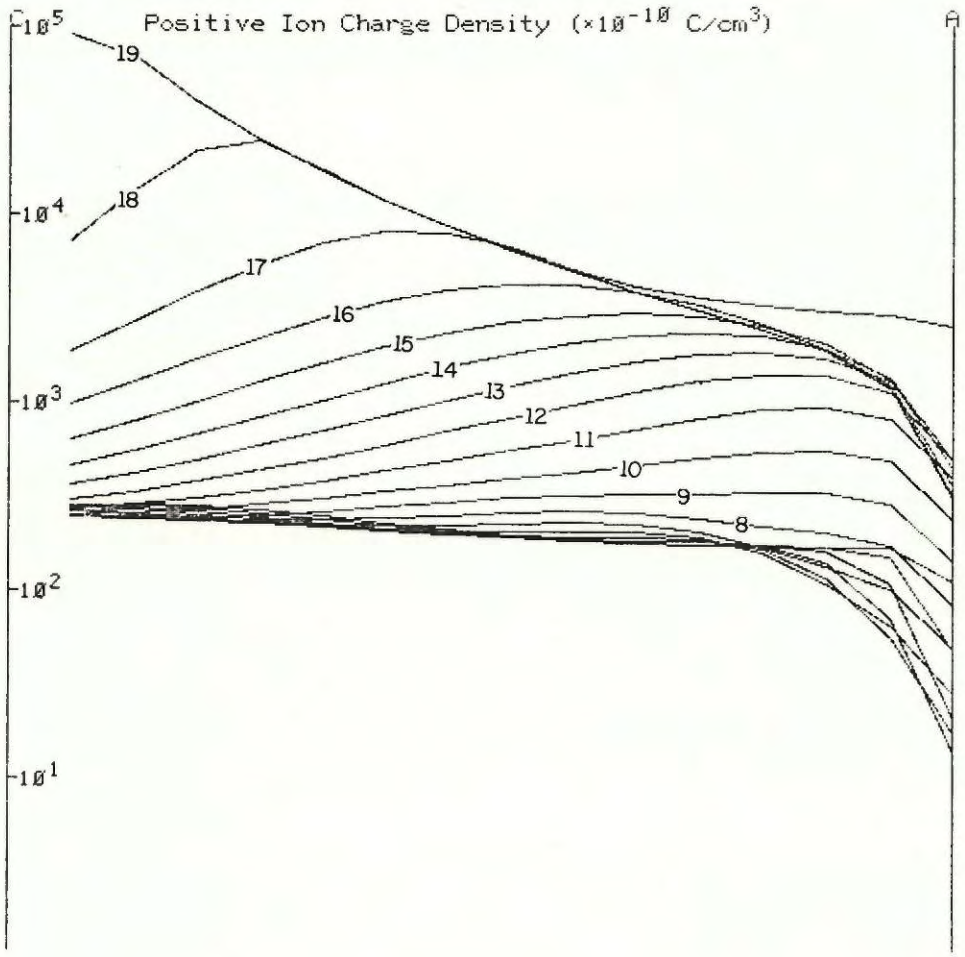

Figure 2.7. Positive ion charge density as a function of space and time during the discharge growth. The scale is the same as used in Figure 2.6.

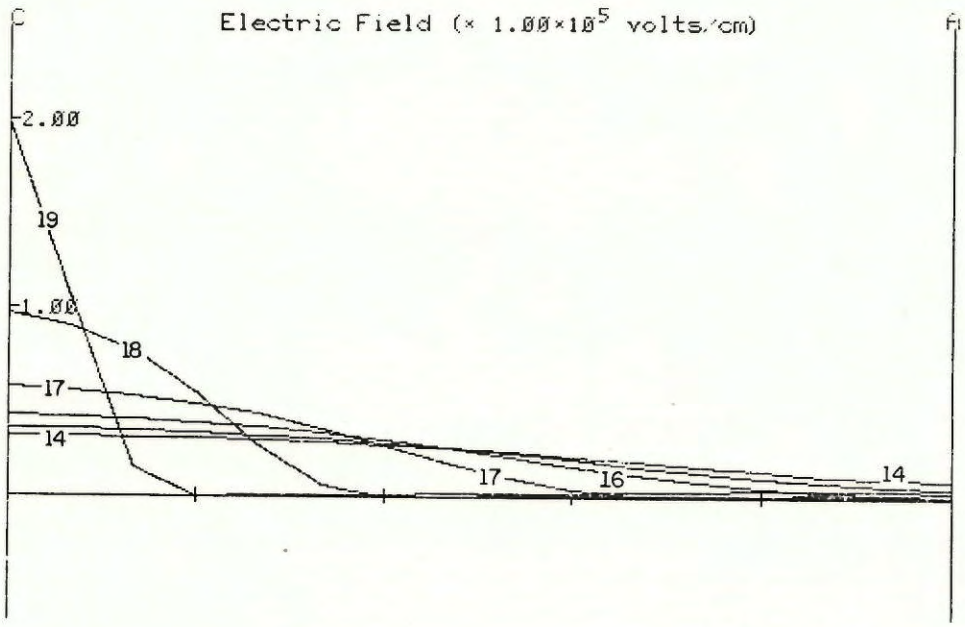

Figure 2.8. Electric field as a function of space and time for the discharge growth. The vertical scale is 10^5 V/cm per division. The horizontal scale is the same as that of Figure 2.6.

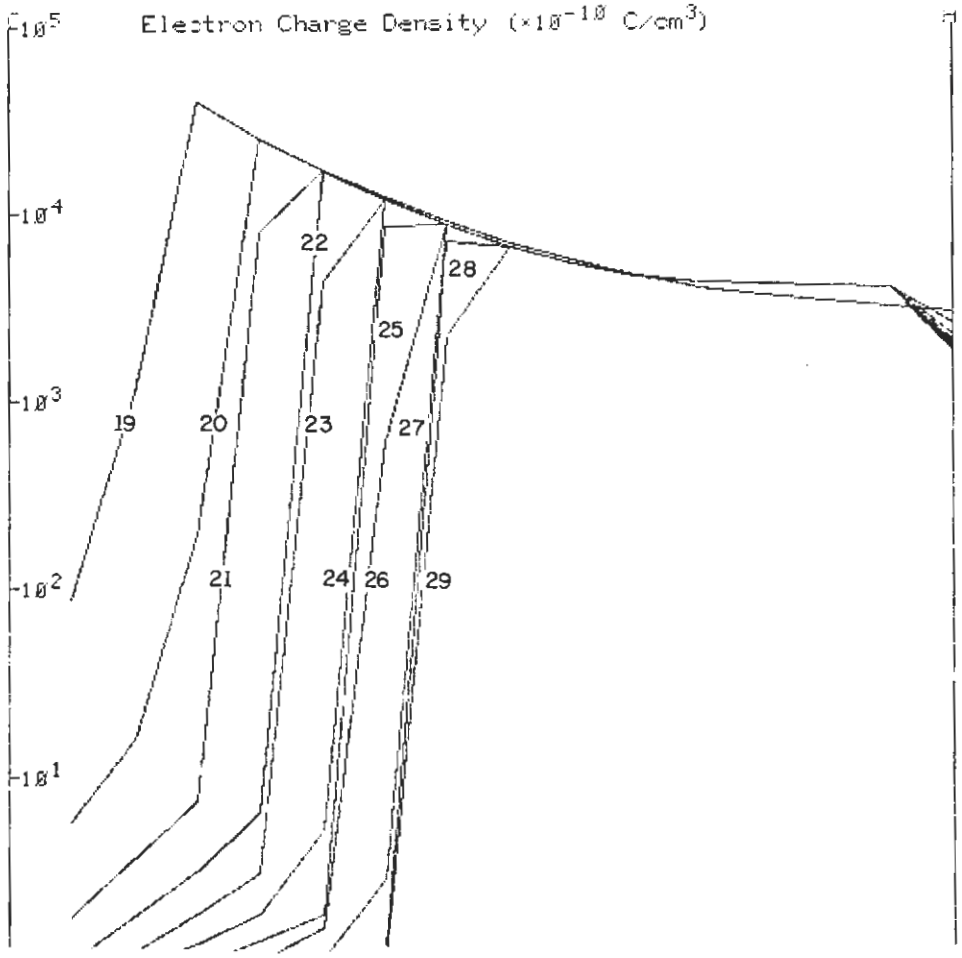

Figure 2.9. Electron charge density as a function of space and time for the decay of the discharge shown in Figure 2.3. The scale is the same as in Figure 2.6. The time step between curves is 33.3 ns.

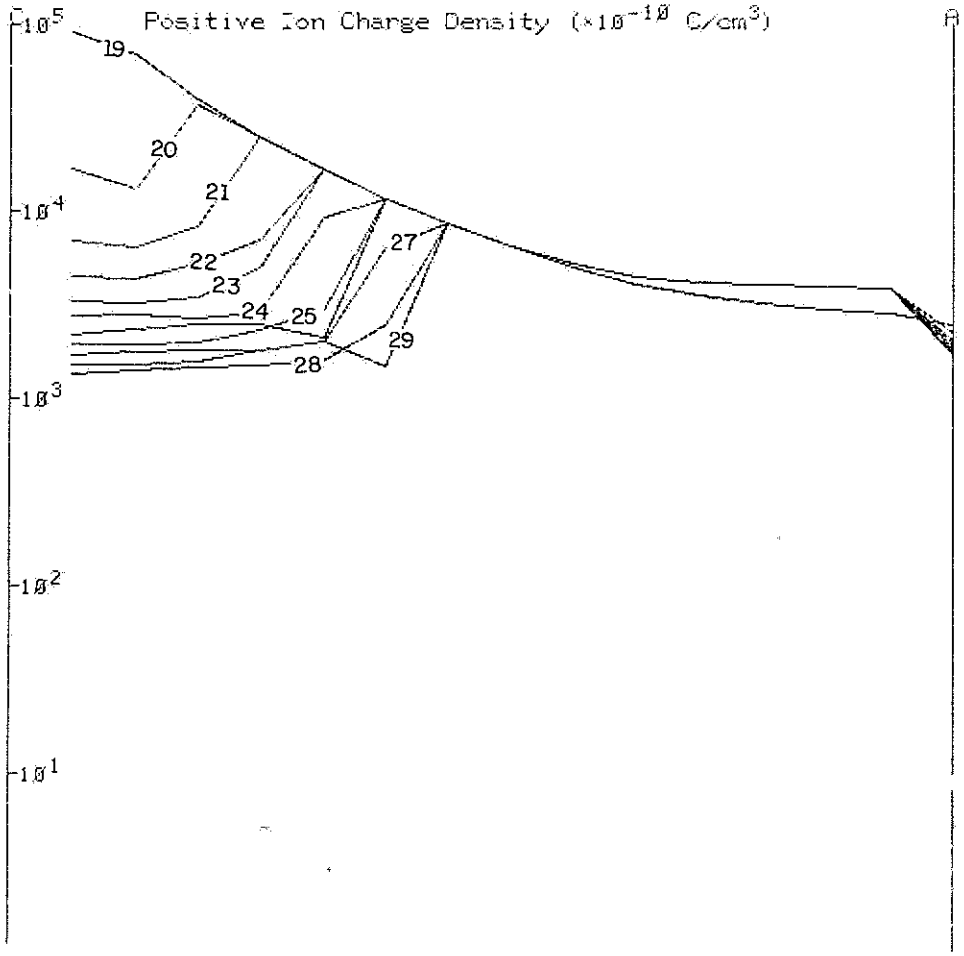

Figure 2.10. Positive ion charge density for space and time during the discharge decay. The scale is the same as for Figure 2.9.

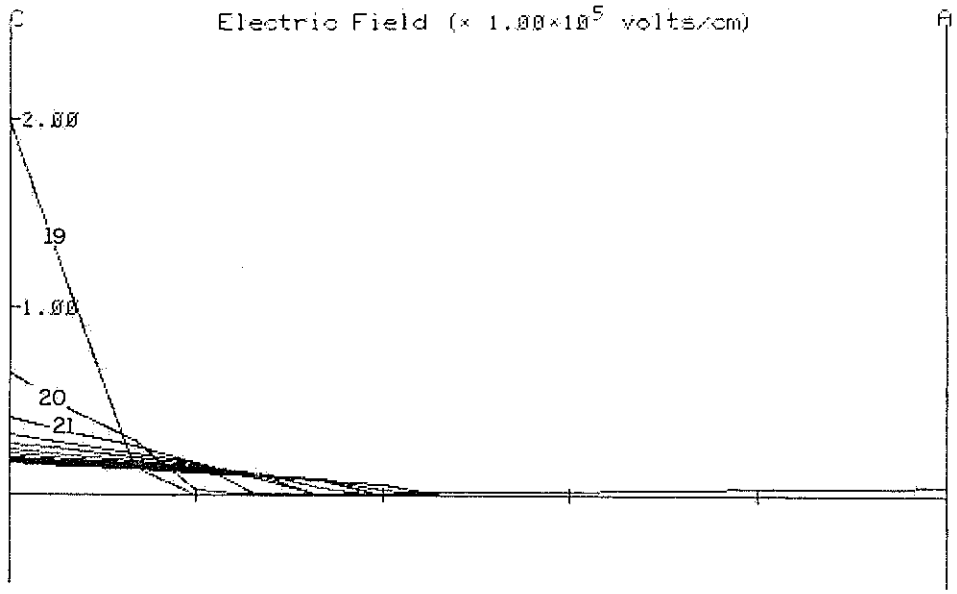

Figure 2.11. Electric field as a function of space and time for the discharge decay. The scale is the same as for Figure 2.8. The time step between curves is 33.3 ns.

electron and ion densities are so great that they cancel out the field. With no field to push them out, they are trapped in the volume. This is a plasma in the strict sense that the Debye length is much shorter than the size of the container. For the density of 10^{-6} C/cm^3 the Debye length is smaller than 1 μm for an electron temperature of 1000°K. Since the spacing between the cathode and anode is 150 μm, it is safe to say that this is indeed a plasma.

The growth of the discharge to a plasma shown in Figure 2.6 is typical of most discharges studied here. In the early stages, the electrons grow across the gap in an exponential fashion. The ions, which move much slower than the electrons, initially grow to greater densities than the electrons and significantly distort the field. The electrons then try to neutralize the field set up by the ions until the plasma fully develops near the peak of the discharge activity. The discharge current then dies down as the wall charge accumulates and the field in the cathode region diminishes; however, the plasma remains. Ordinarily such plasmas decay by ambipolar diffusion and by electron-ion recombination. Neither of these effects was included in these calculations, however Ward [10] has shown that a small amount of diffusion is implicit in the calculational technique. Thus this could account for the slow decay seen in Figure 2.9. A general rule observed in these calculations is that the greater the plasma density, the slower this decay becomes. In some discharges, no evidence of decay is seen even after 3 μsec. In others the plasma lasts for only a few hundred nanoseconds. However, there is typically plasma left in the volume near the anode for at least 2 μs and usually until the end of the discharge cycle of 3 μs. The existence of this very strong, long lived plasma was not shown by any of the

previous authors and is thought to be one of the very significant results of these calculations. In later chapters of this thesis, experimental results are presented that confirm the existence of this plasma.

It is interesting to note from the data in Figure 2.8 that the peak field at the cathode is 2×10^5 V/cm. This is typical for the discharges studied here. This is a strong enough field so that field emission might be considered an important mechanism for electron ejection out of the cathode [16]. This might be especially important if the glass cathode has small protrusions or is rough so that the field in these areas would be especially high [6].

Figure 2.12 shows the log of the current shown in Figure 2.3. Another type of current growth seen frequently in other discharges is shown in Figure 2.13. This data clearly shows that the discharge current grows exponentially soon after the application of the sustain voltage pulse. This exponential growth continues until field distortion becomes important. The The field distortion typically causes the current to increase faster than the previous exponential growth until the effects of wall charge set in and cause the current to decrease in intensity. The explanation of why the discharge current increases at a faster rate shortly before the peak of the discharge can be seen by looking at the quantity

$$\mu = \gamma_i (\exp(\alpha d)-1) . \qquad (2.13)$$

This is defined as the number of secondary electrons ejected from the cathode for every initial single electron that starts from the cathode and causes an avalanche [17]. This quantity is very important to Townsend discharge theory since the voltage where $\mu = 1$ defines the threshold for a self-sustained gas

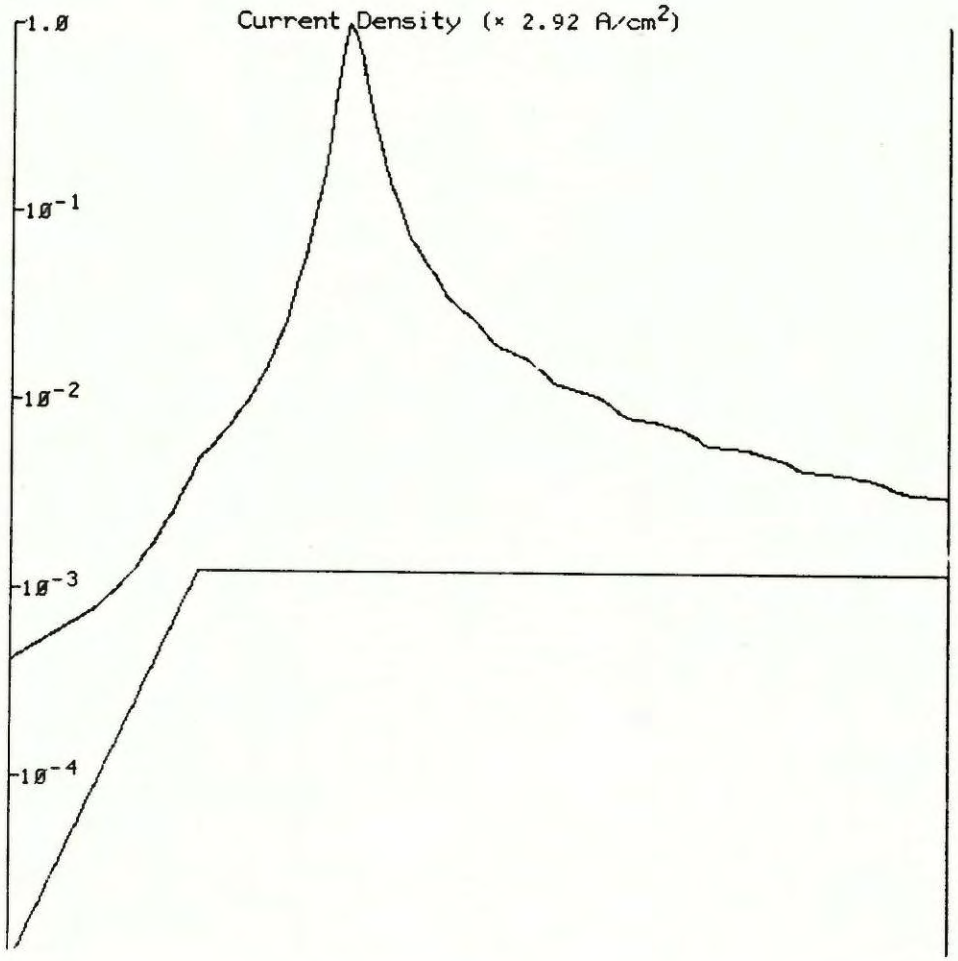

Figure 2.12. Log of discharge current shown in Figure 2.3. The vertical scale division marked 1.0 corresponds to 2.92 A/cm^2. The applied sustain voltage is seen in the lower curve. The time scale is the same as in Figure 2.3. The small oscillations seen in the current decay are due to error in the calculational technique.

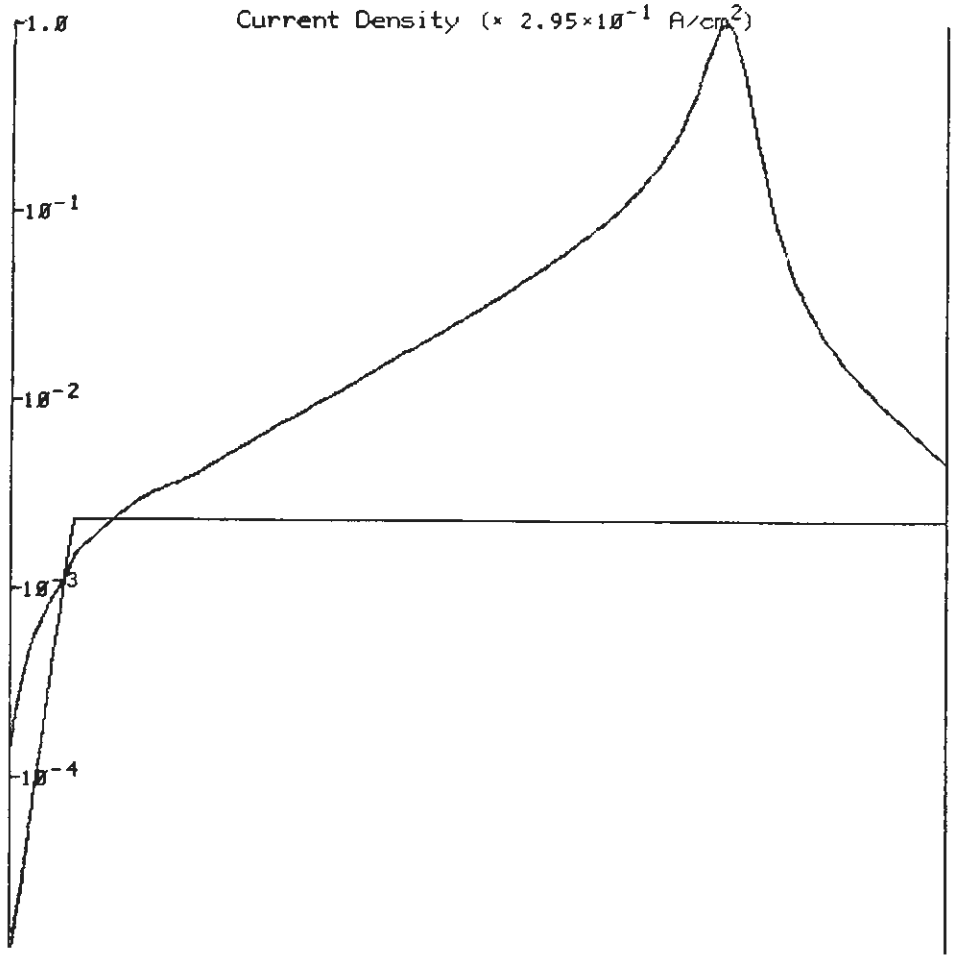

Figure 2.13. Log of discharge current showing the behavior seen in many discharges. The vertical scale division marked 1.0 corresponds to .295 A/cm^2. The total horizontal time span is 1.5 μ s.

discharge. It can be shown analytically that if μ is a constant greater than one, and no field distortion is present, the discharge current will grow exponentially [18]. This theory explains completely the early exponential growth of the discharge current shown in Figure 2.13. When field distortion sets in, the situation becomes more complicated. The Townsend coefficient α, which is a constant in equation (2.13), now becomes a function of x and t. Thus the following equation must be used in place of (2.13).

$$\mu(t) = \gamma_i \left(\exp\left[\int_0^d \alpha(x,t)dx \right] - 1 \right) \tag{2.14}$$

In this case $\alpha(x,t)$ is found from equation (2.9) and the value of $E(x,t)$. Figure 2.14 shows a plot of $\mu(t)$ for the discharge shown in Figure 2.13. In the early exponential growth stages of the discharge, μ is nearly constant. However, as field distortion sets in, the field becomes larger near the cathode and smaller near the anode. If conditions are right, this will cause μ to increase. Since more secondary electrons are now returning for every primary electron, the discharge current grows faster as shown in Figure 2.13. Finally the effects of wall charge decrease μ to a very low value and the discharge extinguishes. More will be said about the conditions necessary for μ to increase as shown in Figure 2.14 in Chapter 3, since this effect is closely tied to one of the memory mechanisms found in the plasma display panel.

The plot of $\mu(t)$ for the discharge of Figures 2.3 through 2.12 is shown in Figure 2.15. It shows a peak very similar to that in the discharge of Figures 2.13 and 2.14. The difference in these two discharges is that in Figure 2.12, the initial current is large due to the large number of ions

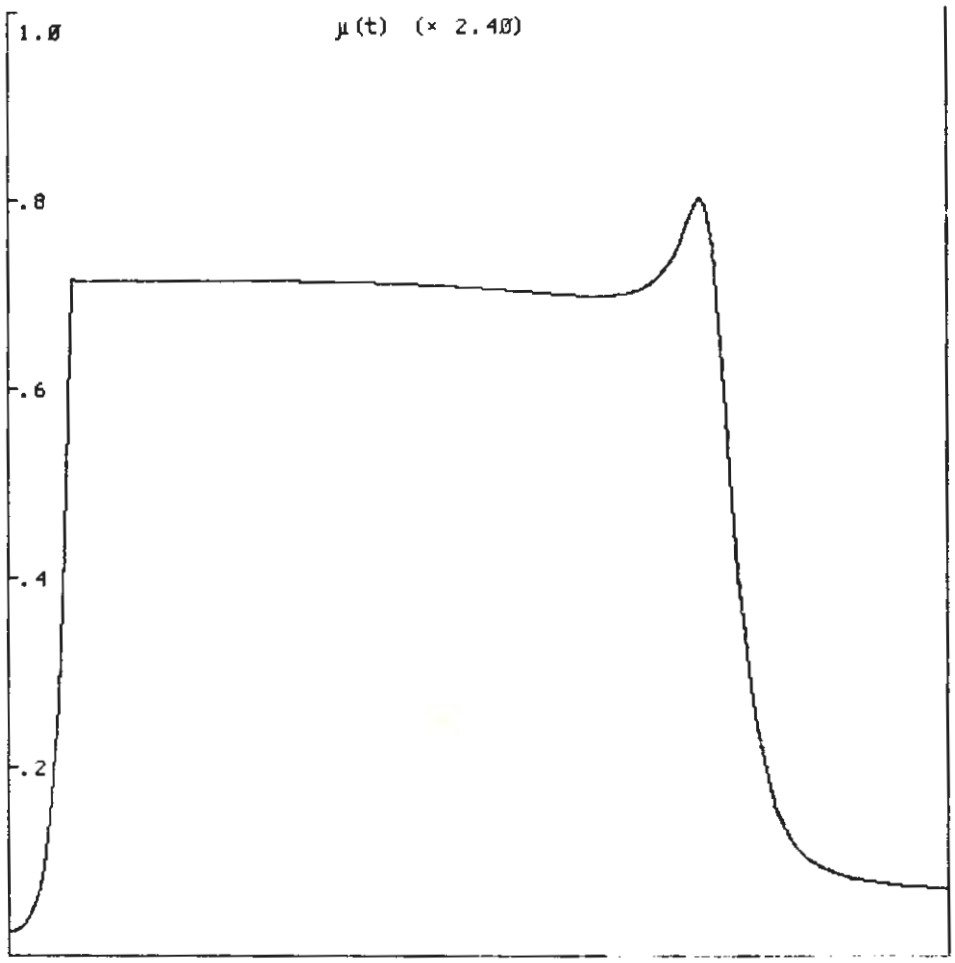

Figure 2.14. The value of $\mu(t)$ for the discharge shown in Figure 2.13. The vertical scale mark of 1.0 corresponds to $\mu = 2.40$. The time scale is the same as in Figure 2.13.

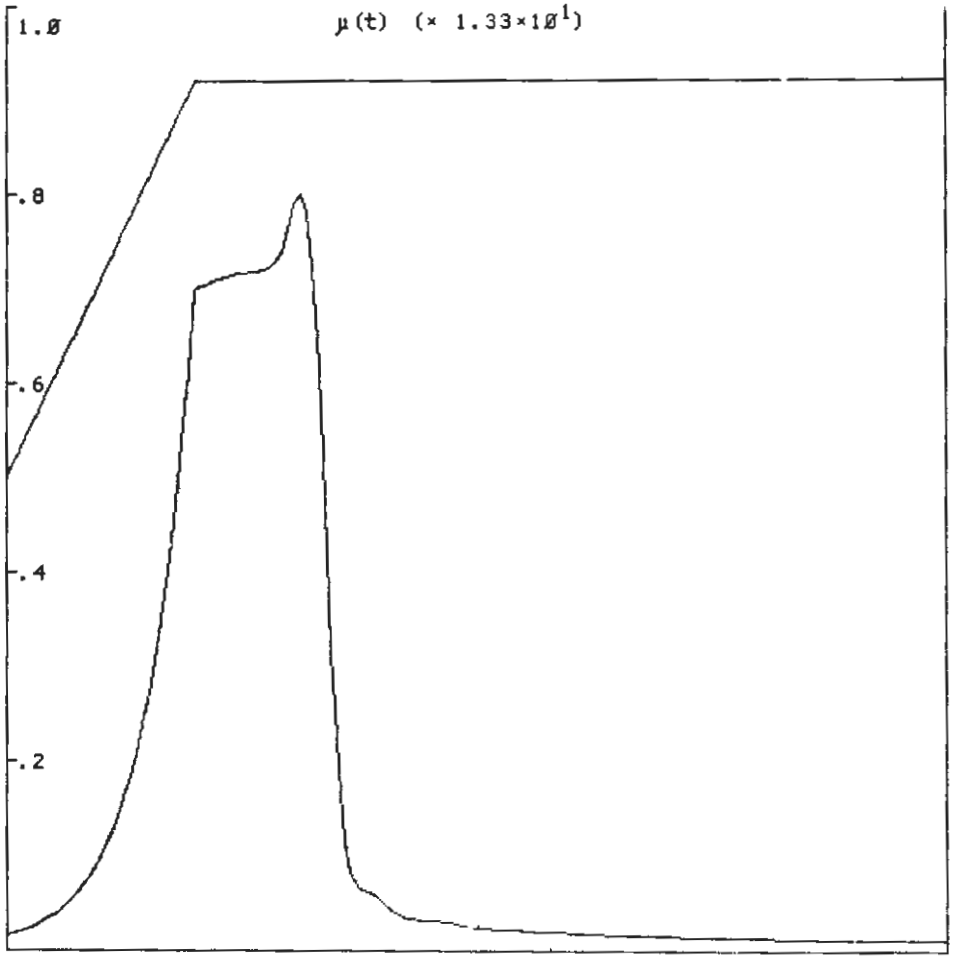

Figure 2.15. The value of $\mu(t)$ for the discharge shown in Figures 2.3 through 2.12. The vertical scale mark of 1.0 corresponds to $\mu = 13.3$. The applied sustain voltage is also shown. The time scale is the same as in Figure 2.3.

left from the previous discharge. These ions are seen in Figure 2.7. The discharge of Figure 2.13 has a much lower initial number of ions, and thus it grows exponentially until field distortion sets in. The effects of field distortion are seen almost immediately in the data of Figure 2.12.

A very interesting quantity to observe is the light emitted from the discharge as a function of space and time. This light output can be approximated by the quantity $\alpha(x,t) \cdot j_e(x,t)$, which is the number of electron ion pairs created at a given place and time. Since $\alpha \cdot j_e$ is generally a measure of discharge activity, it should be very nearly proportional to the actual light output. Figure 2.16 shows a log plot of this quantity for the discharge of Figure 2.3. The sequence is the same as in Figures 2.6, 2.7 and 2.8, showing the activity up to the discharge current peak. The light output increases exponentially in space for the early periods of the discharge. This is due to the expected growth of the avalanches. However, as field distortion sets in, a light wave grows out of the anode and moves toward the cathode where the most intense light is emitted. This light behavior has been experimentally measured by Anderson [19] in plasma display cells having large gap spacings. He noticed that these light waves traveled toward the cathode at a velocity of $\sim 7 \times 10^5$ cm/sec. The waves shown here travel at $\sim 2 \times 10^5$ cm/sec. This is a reasonable qualitative agreement since the geometries, gas mixture and sustain voltage of the two cases are vastly different.

Anderson also showed a light pulse that occurs near the anode at the same time as the peak occurs at the cathode. This peak near the anode is clearly shown in periods 18 and 19 of Figure 2.16. The reason for this peak

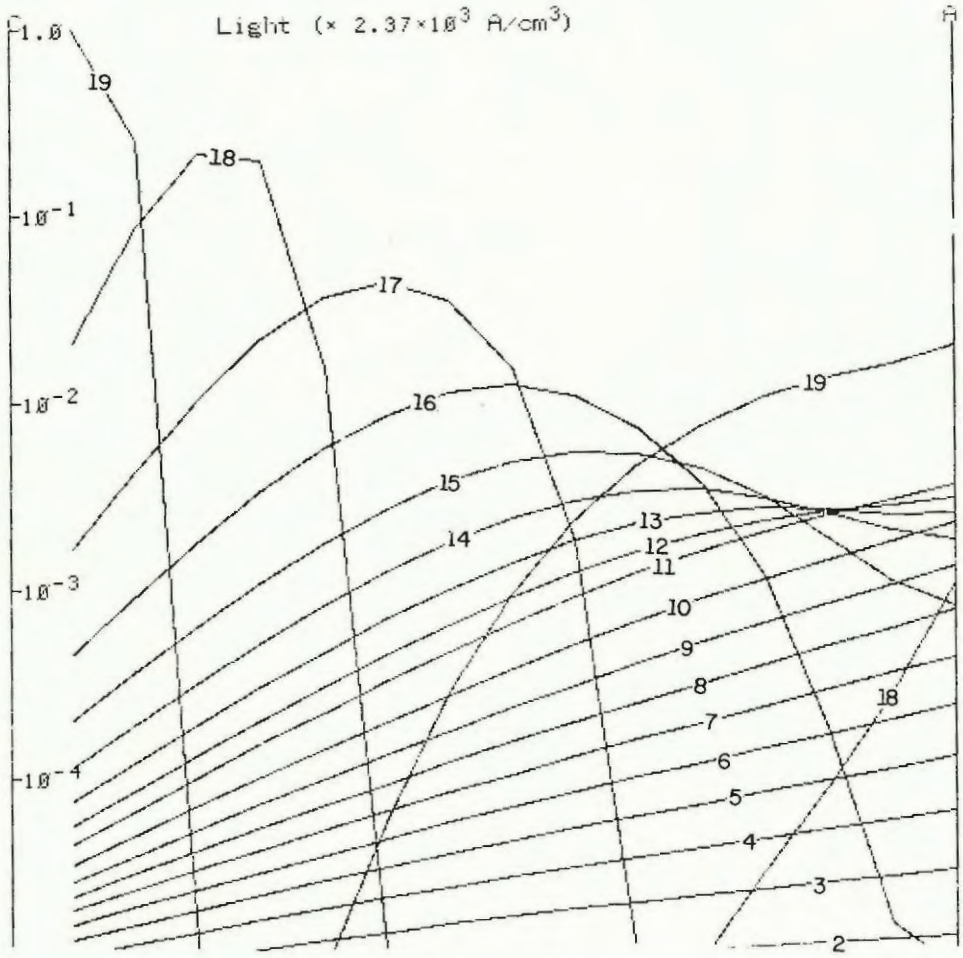

Figure 2.16. Discharge activity described by the quantity $\alpha(x,t) \cdot j_e(x,t)$. This quantity is approximately proportional to the light output. The horizontal scale is the space between the cathode and anode and is the same as in Figure 2.6. The vertical scale is the log of the intensity with the 1.0 scale mark equal to 2.37 x 10^3 A/cm^3. The time step is 10 ns.

can be seen by analyzing the electric field near the anode region. Because the plasma is in this region, a linear electric field plot such as shown in Figure 2.8 shows the field to be almost zero. In order to see the field variation more clearly, a log plot of the field is shown in Figure 2.17. From this it is clearly seen that the field near the anode is considerably greater than the field near the center of the cell. The higher E means a higher α in the anode region. Since the current through the plasma is nearly constant as a function of space, it seems reasonable that $\alpha \cdot j_e$ should be larger near the anode than near the center of the cell.

Other quantities of interest are the current densities $j_e(x,t)$ and $j_i(x,t)$ shown in Figures 2.18 through 2.21. As in the previous figures, Figures 2.18 and 2.19 represent the growth of the discharge to the current peak, and Figures 2.20 and 2.21 represent the decay. In the early stages the growth of j_e is exponential in space just as in the electron and ion density displays. After field distortion sets in, the ion current is predominant in the high field region and the electron current is predominant in the plasma region. As in a DC cathode glow, the density of the ions at the cathode is much greater than the density of the electrons, so that only the ions contribute significantly to the current. In the plasma region, the electron and ion densities are equal, so that the electrons contribute most significantly because of their much greater velocity.

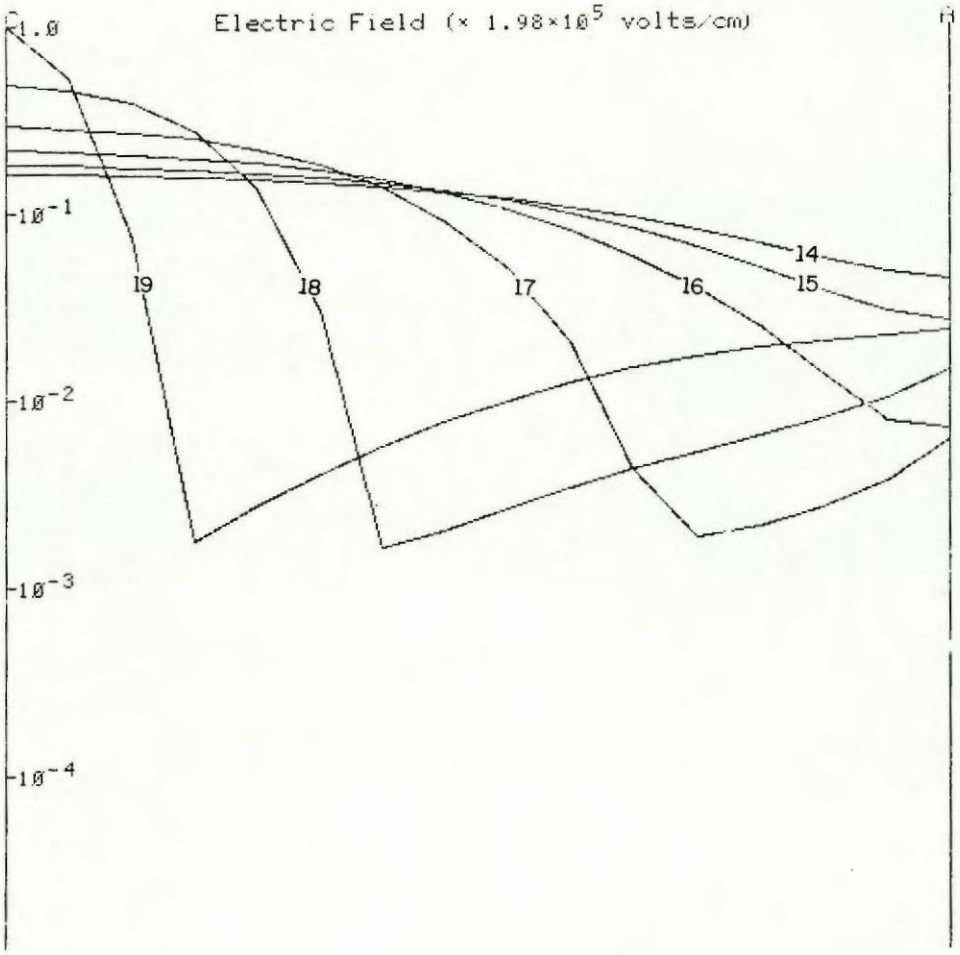

Figure 2.17. Log of the electric field intensity as a function of space and time. This is the same data as seen in Figure 2.8. The vertical scale mark of 1.0 corresponds to 1.98×10^5 V/cm. The horizontal scale is space and the time step is 10 ns.

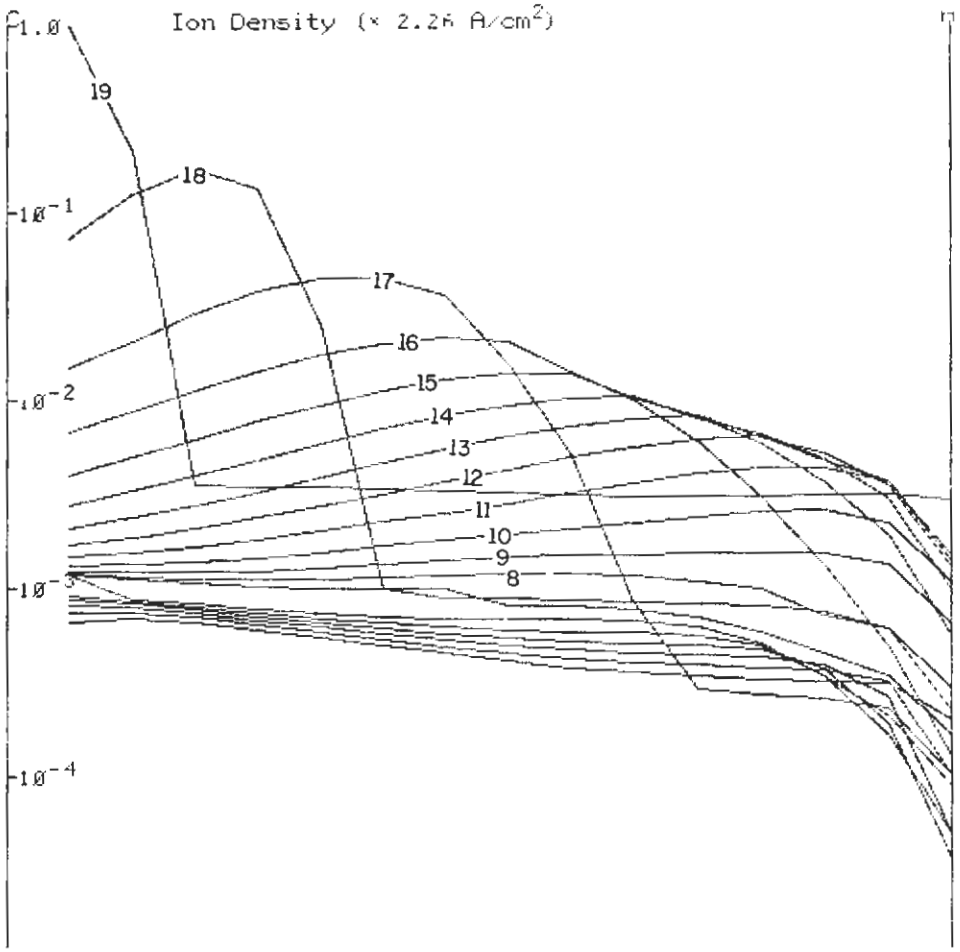

Figure 2.19. Log of ion current density, $j_i(x,t)$, for the growth of the discharge. The vertical scale mark of 1.0 corresponds to 2.26 A/cm^2. The horizontal scale is space and the time step is 10 ns.

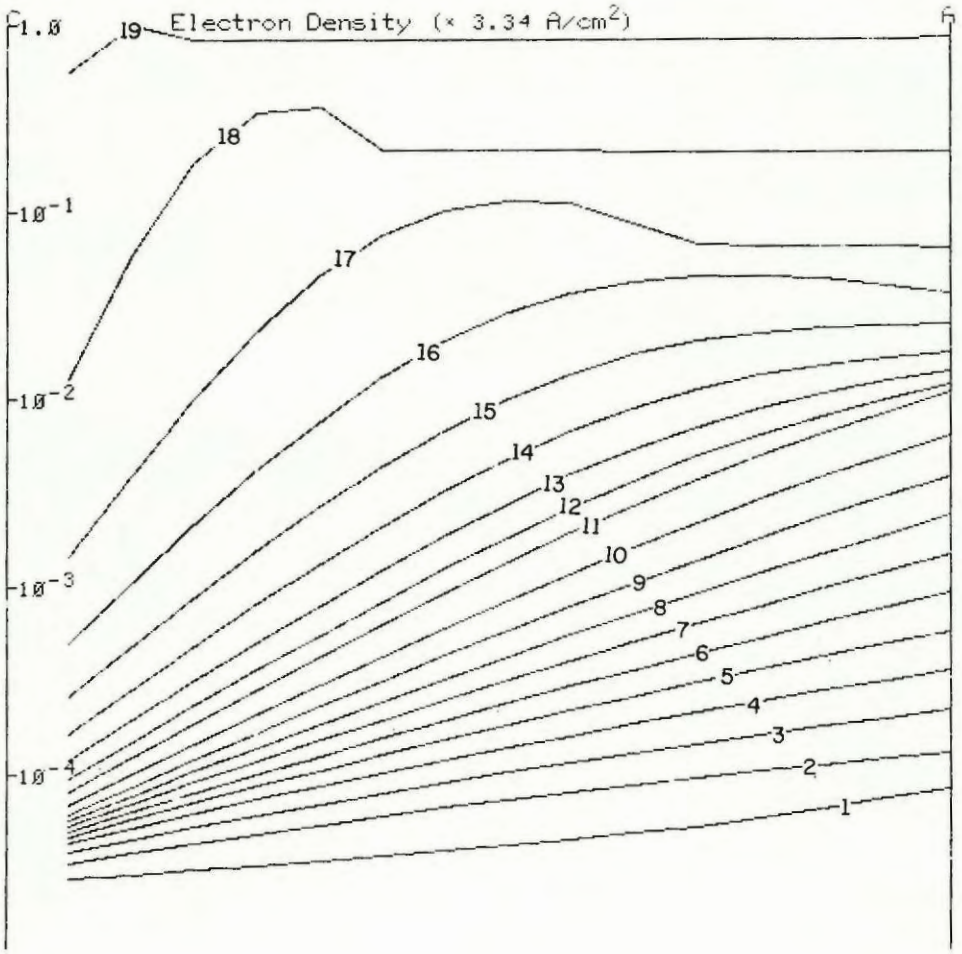

Figure 2.18. Log of electron current density, $j_e(x,t)$, for the growth of the discharge. The vertical scale mark of 1.0 corresponds to 3.34 A/cm^2. The horizontal scale is space and the time step is 10 ns.

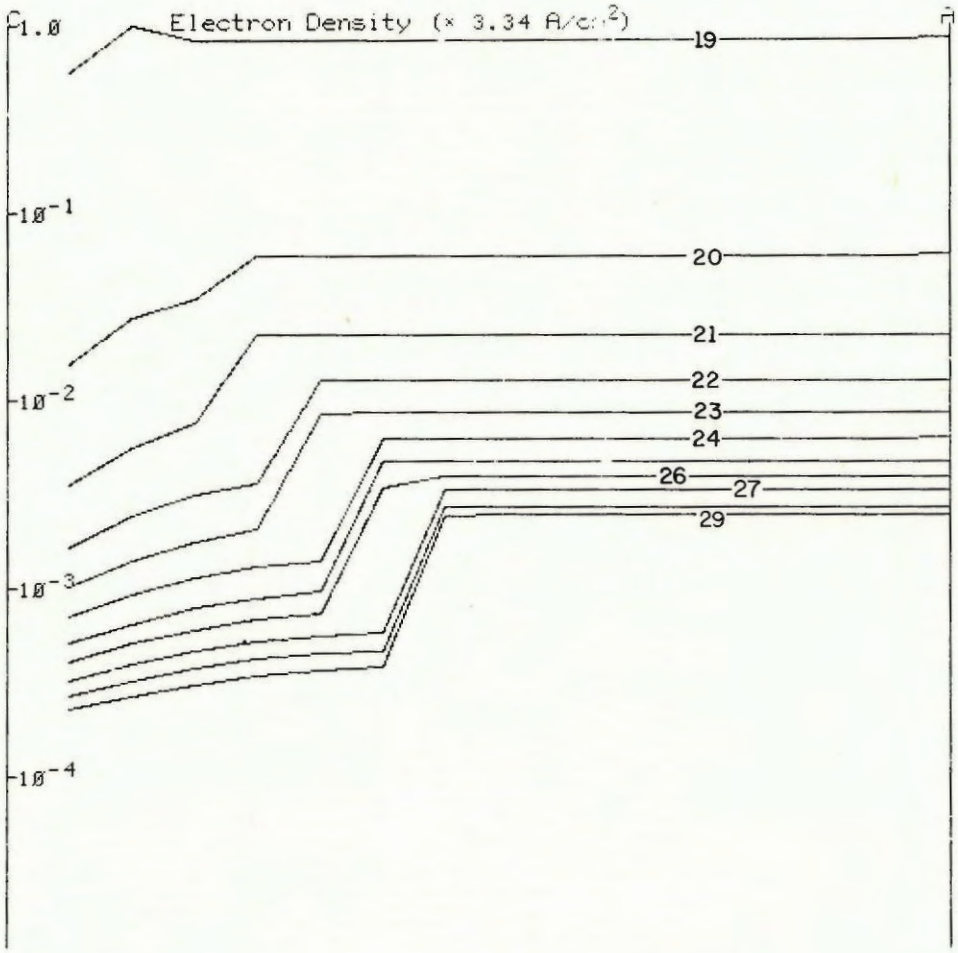

Figure 2.20. Log of electron current density for the decay of the discharge. The scale is the same as for Figure 2.18. The time step is 33.3 ns.

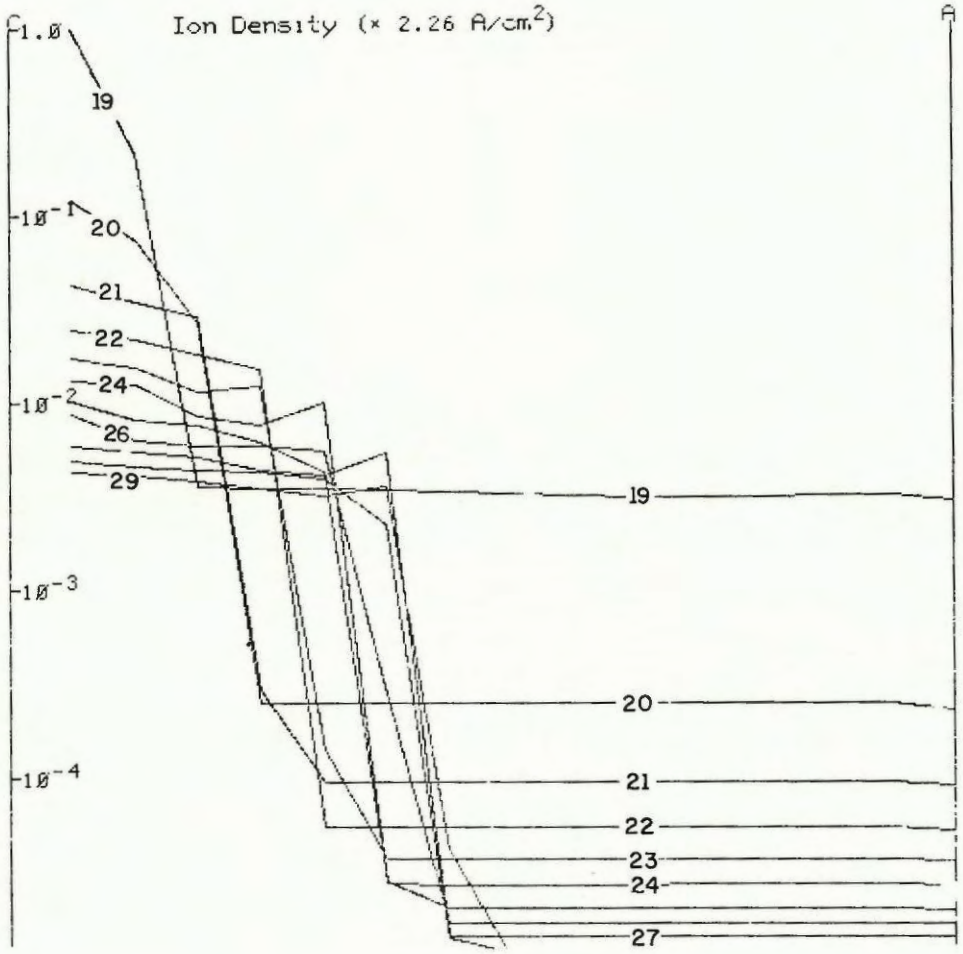

Figure 2.21. Log of the ion current density for the decay of the discharge. The scale is the same as for Figure 2.19. The time step is 33.3 ns.

CHAPTER 3

THE EFFECTS OF PRESSURE AND SUSTAIN WAVEFORM ON THE CHARGE TRANSFER CURVE AND MEMORY

3.1 Introduction

In this section the computer calculations are used to gain information about what parameters effect the important electrical characteristics of the AC plasma display cell. A central theme of this part is the question "why does this device exhibit memory?" This question has not been completely answered by other researchers. There exists a theory that states that the cell will have memory if the gas discharge exhibits certain characteristics. However, the explanation, based on gas discharge physics, of why the discharge exhibits the necessary characteristics has never been presented. The results of these calculations have shown the existence of two memory mechanisms. One varies strongly on the sustain voltage waveform and the other varies strongly with the gas pressure.

3.2 Basic Charge Transfer Curve Theory

To start this discussion, one must understand the results of the basic stability theory for this device, originally formulated by Arora and Slottow [20] and later revised by Slottow and Petty [21]. To determine the electrical characteristics of the cell, one can construct a characteristic curve for the device called a charge transfer curve. This curve plots the response, ΔV_w, or change in wall voltage for a discharge as a function of the driving force, V_c, which is the total voltage across the gas at the beginning of the discharge. V_c is commonly referred to as the cell voltage.

Figure 3.1 shows these voltages for a stable series of discharges. A typical shape for the charge transfer curve is shown in Figure 3.2. The threshold properties of the gas discharge exhibit themselves by the fact that V_c must be above a threshold value before ΔV_w becomes greater than zero. The slope = 1 line drawn through the origin sets a limit to the excursion of the charge transfer curve. Since ΔV_w must be less than V_c, the line $\Delta V_w = V_c$ sets the limit and defines the case in which the wall charge completely cancels out the electric field across the gas volume imposed by the applied sustain voltage.

A stable sequence of discharges, such as shown in Figure 3.1, would operate at one point on the curve of Figure 3.2, since for each discharge, ΔV_w and V_c are the same as their respective values of the previous discharges. The theory states that there are stable and unstable regions of the charge transfer curve. In a stable region, if, for whatever reason, a discharge is stronger or weaker than the average equilibrium discharge intensity, then the following discharges will adjust their intensity to compensate for this perturbation and force the sequence back to the equilibrium point on the transfer curve. However, in an unstable region, the discharges following a small perturbation would act to drive the discharge sequence away from the original equilibrium point until the sequence finds a new equilibrium point on a stable region of the transfer curve.

The theory further states that stable regions of the curve will have a slope less than 2, and unstable regions will have a slope greater than 2. Thus for the curve in Figure 3.2, as V_c increases, there is a stable region where ΔV_w is very small. A further increase in V_c pushes the sequence

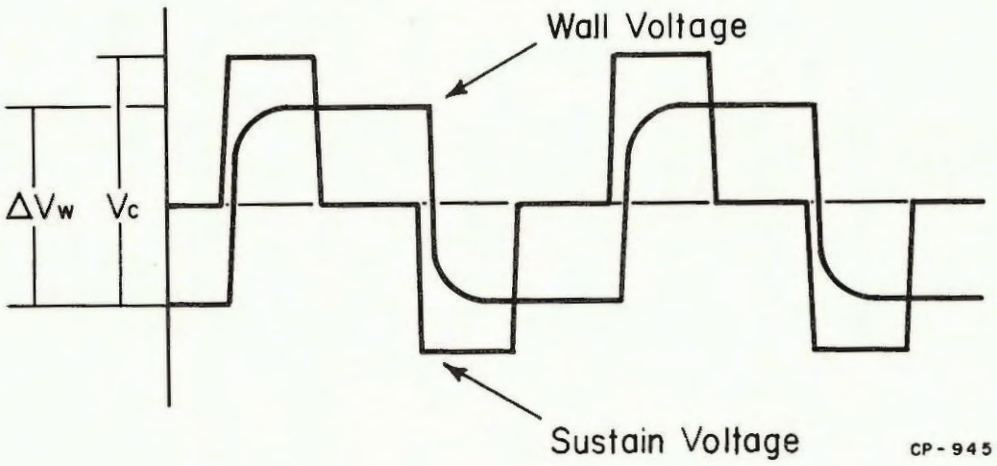

Figure 3.1. Sustain voltage and wall voltage for a cell in the on state. V_c is the initial voltage across the gas and ΔV_w is the change in wall voltage due to the discharge.

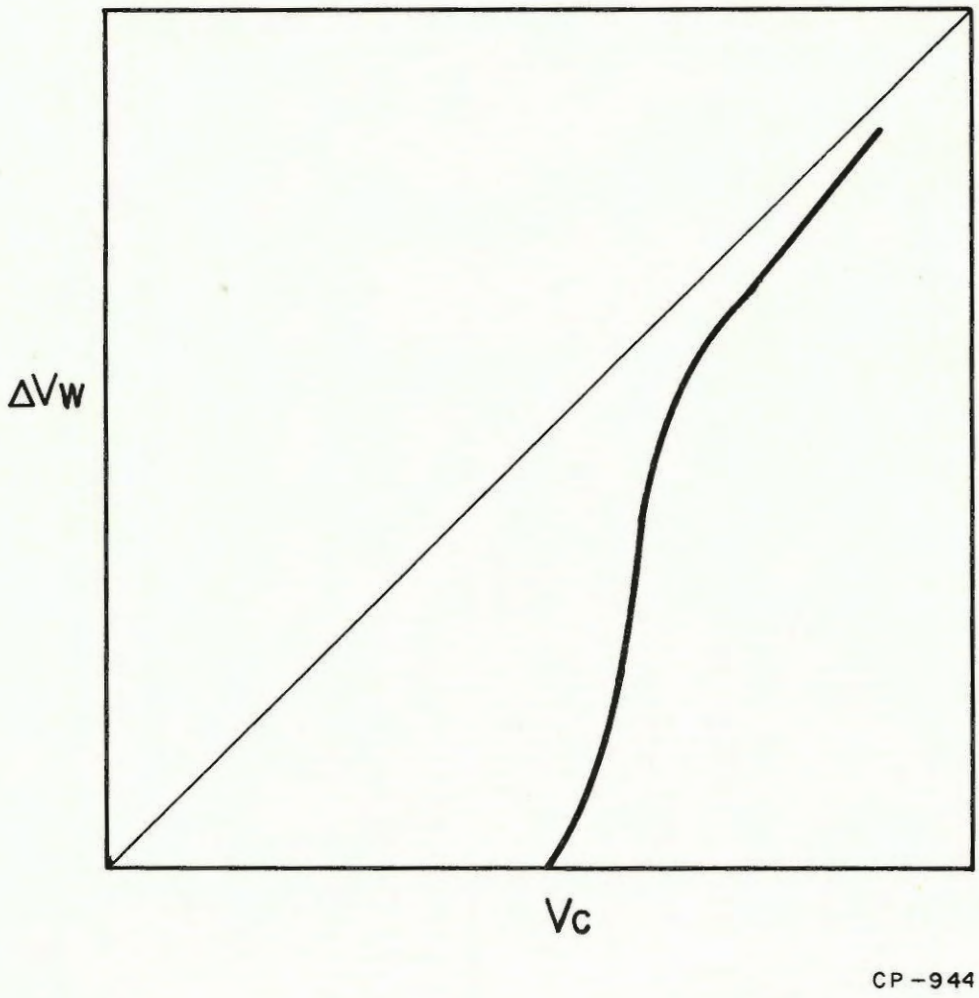

Figure 3.2. A typical wall charge transfer curve showing the total change in wall voltage as a function of the initial voltage across the gas.

into an unstable region having intermediate values of ΔV_w. As V_c becomes high, a stable region is entered. Thus there are two stable regions separated by one unstable region. The lower stable region corresponds to an off cell and the upper stable region corresponds to an on cell. The unstable region serves the very important purpose of separating the two stable regions. If there is no unstable region, then the two stable regions merge into one. With only one stable region the cell will not exhibit any memory effects, since there is only one possible stable state for any possible sustain voltage. Thus it is clear that to obtain memory in a plasma display cell, the charge transfer curve must have a region where the slope is greater than 2.

Once the shape of the charge transfer curve is known one can easily find such parameters as the firing voltage and minimum sustain voltage by a simple construction shown in Figure 3.3. A straight line intersecting the V_c axis at the value of the applied sustain voltage V_s and having a slope of 2 will intersect the charge transfer curve at all possible operating points. Figure 3.3 shows that three possible operating points exist for the value of sustain voltage V_s. Two of these points are stable and correspond to the on and off states and the third operating point is unstable. If V_s is lowered in value so that the slope 2 line becomes tangent to the upper part of the charge transfer curve, then any further decrease in V_s would allow the cell to operate at only one point - the off state. This is defined as the minimum sustain voltage or $V_{s_{min}}$ and is shown in Figure 3.3. Similarly if V_s is raised to a point where the slope 2 line is tangent to the lower part of the curve, one defines the firing voltage or $V_{s_{max}}$.

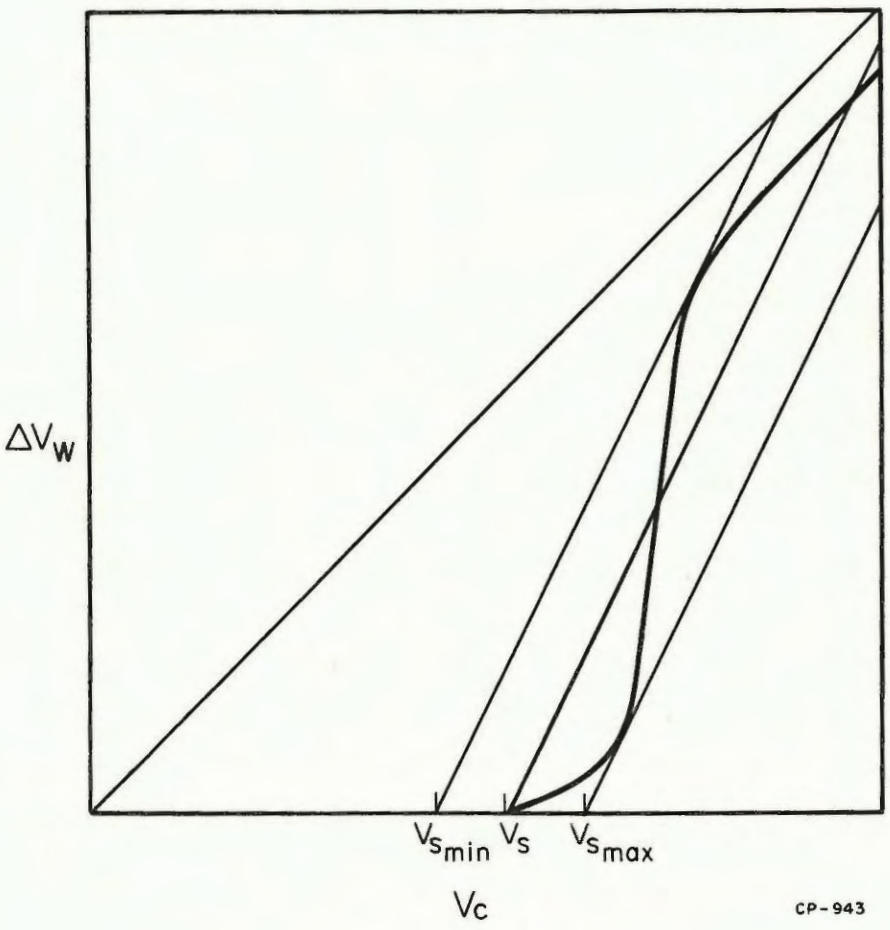

Figure 3.3. Charge transfer curve showing various slope = 2 lines that define the operating points of a discharge sequence. From these constructions one can find the minimum sustaining voltage, $V_{s_{min}}$, and the firing voltage, $V_{s_{max}}$.

3.3 Charge Transfer Curve Calculations

The charge transfer curve serves as a very useful characteristic curve for this device which can explain some of its important electrical characteristics. The above review of the stability theory does not tell the complete story. There has never been an explanation of the shape of the charge transfer curve in terms of basic gas discharge physics. Fortunately, nature does provide devices with charge transfer curves having regions of slope greater than 2. Without this there would be no memory and perhaps no one would be interested in AC plasma display panels. All configurations of sustain voltage waveforms, gas mixtures, and cell geometries have not produced memory effects. However, through tedious empirical efforts, various manufacturers have found the configurations that work best for them in giving the greatest memory margins. Since the shape of the charge transfer curve is so important in determining the electronic characteristic of the device, and since such little is known about how it behaves as a function of various parameters, it was decided to devote the major part of the CPU time available to calculating the charge transfer curve for various situations.

Unfortunately, the calculations of charge transfer curves take a very large amount of CPU time, usually about 50 hours per curve. The basic reason for this is that one discharge gives only one point along the charge transfer curve. Thus a long series of discharges is necessary to get the complete shape of the curve.

There are a number of problems associated with getting useful charge transfer curves. One major problem is that one starts with poor knowledge of what the curve looks like and thus it is difficult to determine

what initial sustain voltage should be used. In the lab it is easy to increase the sustain voltage until the cell fires, but here, one must choose a voltage and then compute a few cycles to see if it looks like the discharge series will travel along the charge transfer curve in a way that will give information about the curve. Many of these trials give very uninteresting results that do nothing but eat up valuable CPU time. However in the later stages of this study, a good model of the properties of the charge transfer curve was achieved so that very little trial and error was needed. The proper sustain voltage could quite often be chosen within a few volts to give the desired curve.

Inspite of this limitation, charge transfer curves were constructed from discharge sequences having various physical conditions. In this study only three things were varied, and they are:

1. The sustain voltage waveform, shape, and amplitude.
2. The gas pressure.
3. The effects of field distortion.

In the first two cases, the variables are ones commonly changed in the laboratory in order to achieve the best memory margins. In the third case, the effects of the ions and electrons on the value of the electric field in the volume were either turned on or turned off. Since Maxwell's equations do not allow one to experimentally turn off the effects of charged species on the electric field value, these calculations can give insight on how field distortion effects the shape of the charge transfer curve in ways not possible experimentally.

The results will be presented in a logical order that resulted from a total understanding of the effects of the variables. Four cases will be discussed covering the combinations of 2 types of sustain waveform and the presence or absence of field distortion. For each case the effects of gas pressure and sustain voltage amplitude will be thoroughly covered.

3.3.1 Case of Square Wave Sustainer with No Field Distortion

The simplest cases to study are those in which field distortion is turned off. Also, the square wave sustain waveform offers the simplest choice. Charge transfer curves were obtained for various gas pressures. Figure 3.4 shows the growth of a discharge sequence by displaying the applied sustain voltage and the resulting wall voltage. Figure 3.5 shows the same variables for a discharge sequence that is dying out to the off state. Discharge sequences that are either growing or dying can be used to give the desired shape of a charge transfer curve.

Figure 3.6 shows 4 charge transfer curves, with the parameter being the gas pressure. These curves all have an astonishing regularity. They all have slopes very close to 2 for nearly their entire excursion. They all appear to be nearly straight lines. All of these curves seem to intersect the V_c axis at the value of the dc breakdown voltage, which is marked on Figure 3.6. This breakdown voltage is determined from equations (2.13) and (2.9), and the condition that $\mu = 1$. The high end of the transfer curves seems to run directly into the slope = 1 line and will continue to follow this line if the sustain voltage is great enough.

The results of Figure 3.6 seem so predictable that one could probably find an analytical mathematical solution to this behavior. Since

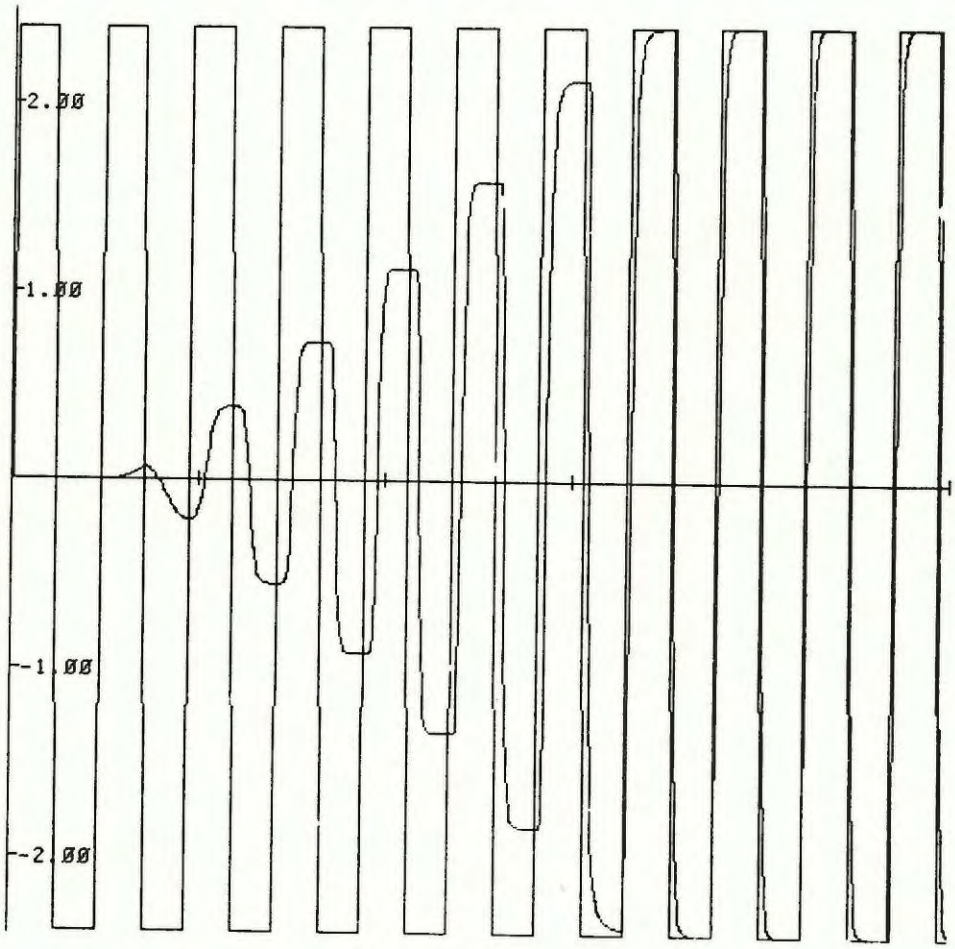

Figure 3.4. Applied sustain voltage and resulting wall voltage for a growing sequence of discharges. The vertical scale factor is 110 volts. Each sustain half cycle lasts 3 μsec. The gas pressure was 700 torr and the effects of field distortion were neglected.

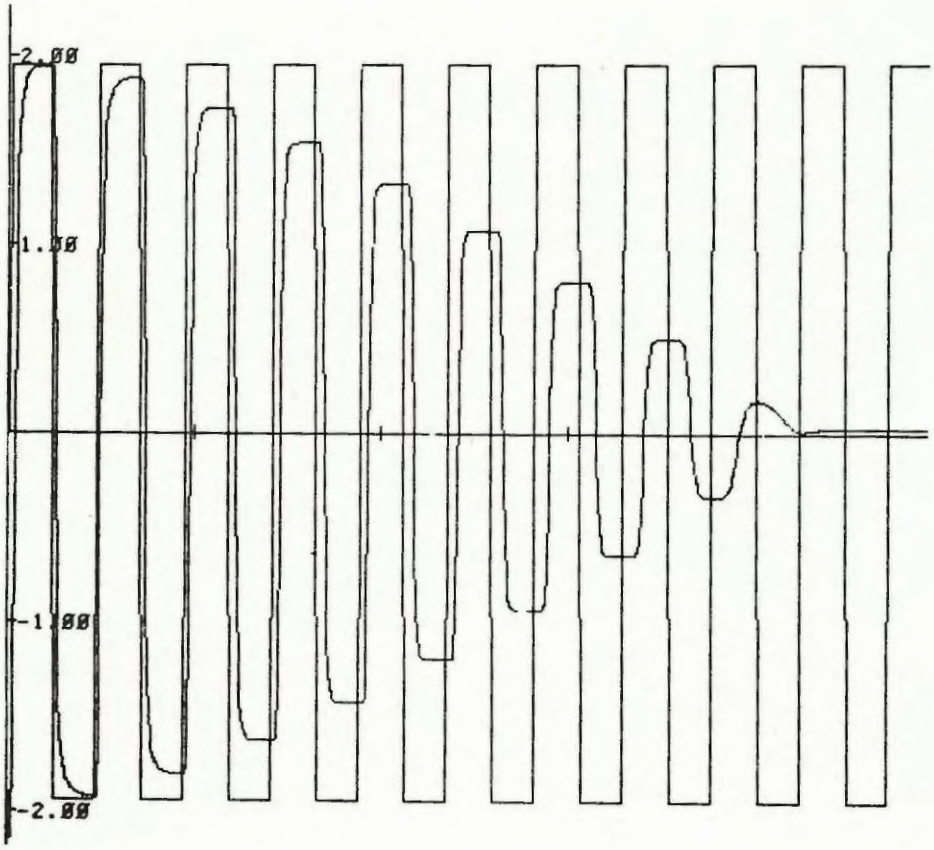

Figure 3.5. Applied sustain voltage and resulting wall voltage for a decaying discharge sequence. The vertical scale factor is 110 volts. The gas pressure was 500 torr.

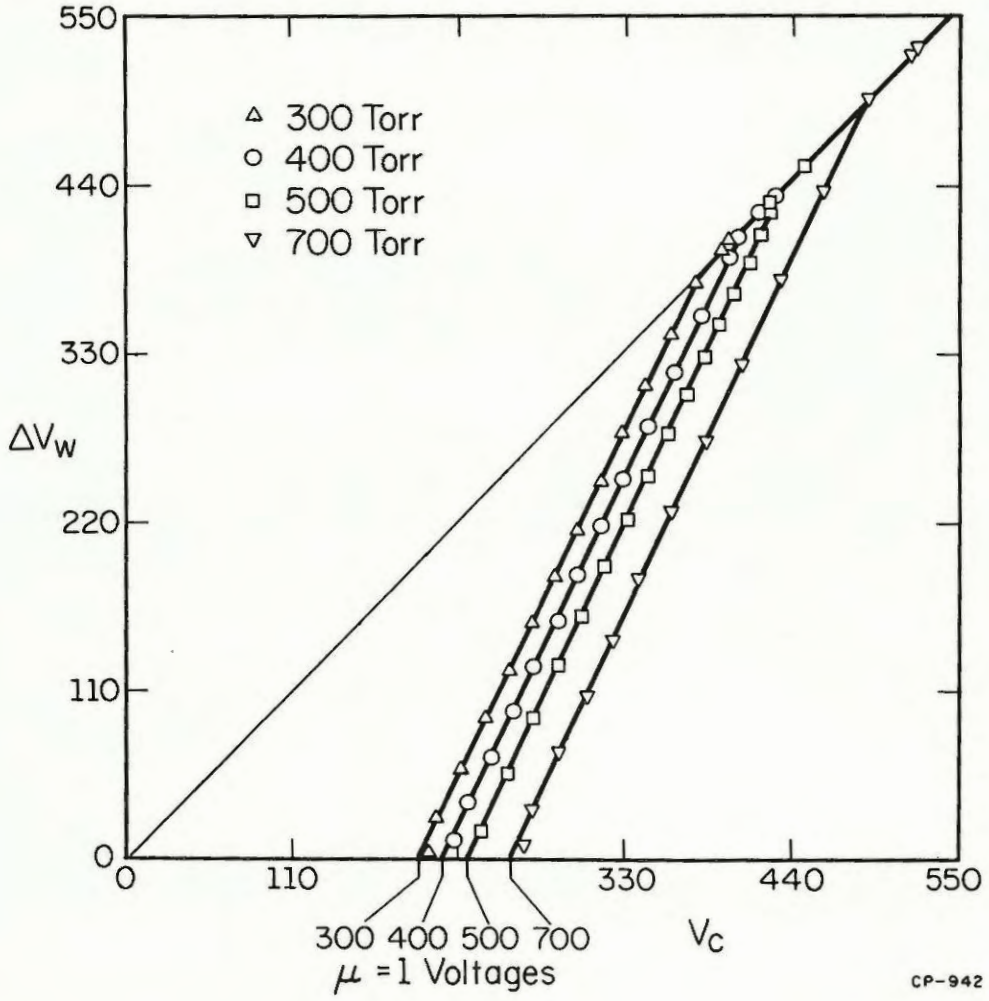

Figure 3.6. Calculated charge transfer curves for 4 different gas pressures. The sustain waveform was a square wave and electric field distortion was neglected.

field distortion is turned off for these results, it does not pose an obstacle to an analytical solution. The fact that all four curves have a slope of 2 is the same as saying that if V_c is V_x volts above the $\mu = 1$ voltage before the discharge, then the final cell voltage will be V_x volts below the $\mu = 1$ voltage. Or similarly, $\Delta V_w = 2V_x$. It is not clear why this relationship should hold; however, some good analytical work should provide some answers.

From Figure 3.6 it is clear that panels operating with these wall charge transfer curves would not exhibit any memory characteristics. If the sustain voltage is above the $\mu = 1$ voltage, then the discharge series will grow until it hits the slope = 1 line. If the sustain voltage is below the $\mu = 1$ voltage, the discharge series will eventually extinguish itself. Thus the case of a square wave and no field distortion would not be of practical interest to the experimenter. It does, however, serve as a theoretical base for the cases that follow.

3.3.2 Case of Non-Square Wave Sustainer without Field Distortion

Figure 3.7 shows a series of discharges taken at p = 500 torr with no field distortion and with a non-square wave sustain waveform. The sustain wave had the shape shown in Figure 3.8. This shape is typical of that used in many commerical plasma display panels [22]. As seen in Figure 3.7, this discharge sequence matured rather abruptly to very strong discharges, thus leaving large gaps in the plot of the charge transfer curve shown in Figure 3.9. To rectify this situation, the sustain voltage was slowly lowered until a sustain voltage was found where the discharge sequence died out as shown in Figure 3.10. The charge transfer curve for both the increasing sequence and the decreasing sequence is found in Figure 3.11.

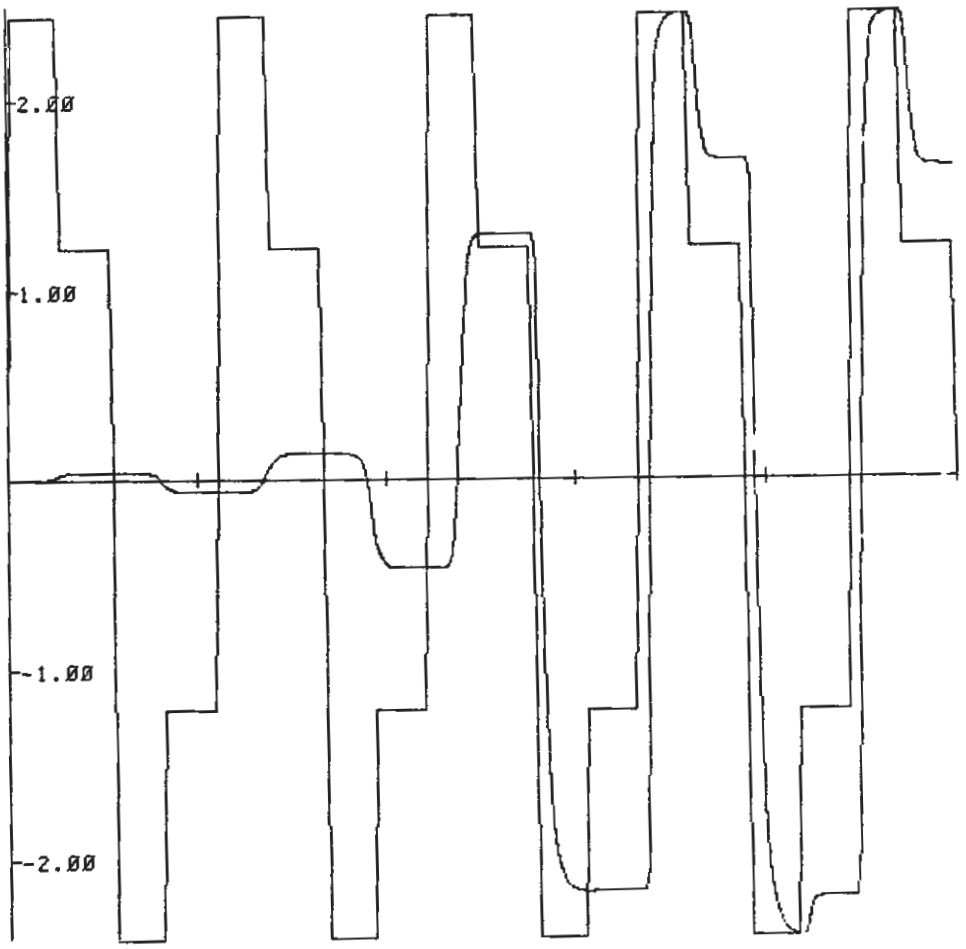

Figure 3.7. Sustain voltage and wall voltage for a growing series of discharges. The vertical scale factor is 110 volts. Each sustain half cycle is 3 μs. The pressure was 500 torr. Field distortion is neglected.

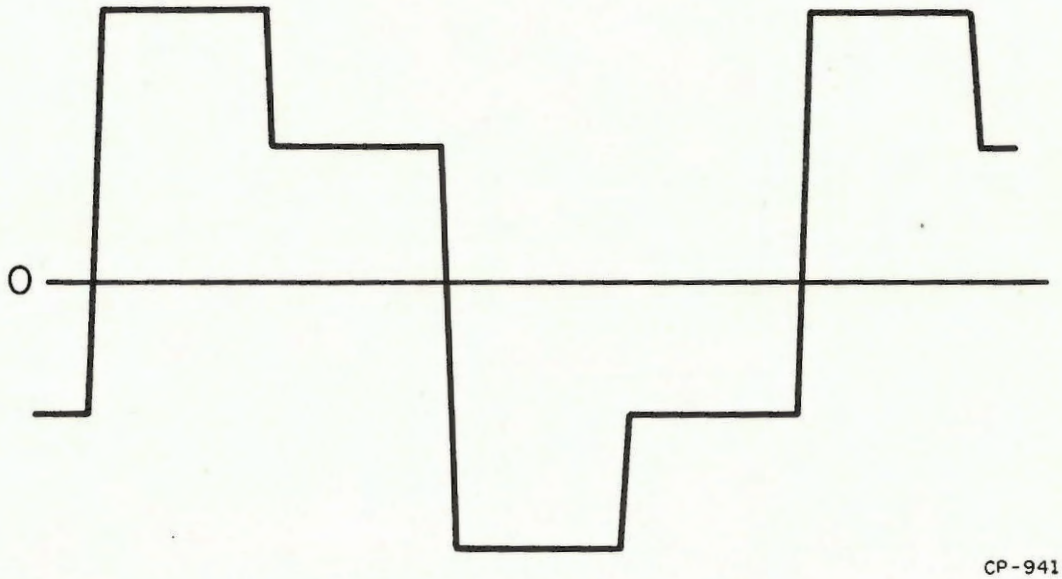

Figure 3.8. Non-square wave sustain waveform.

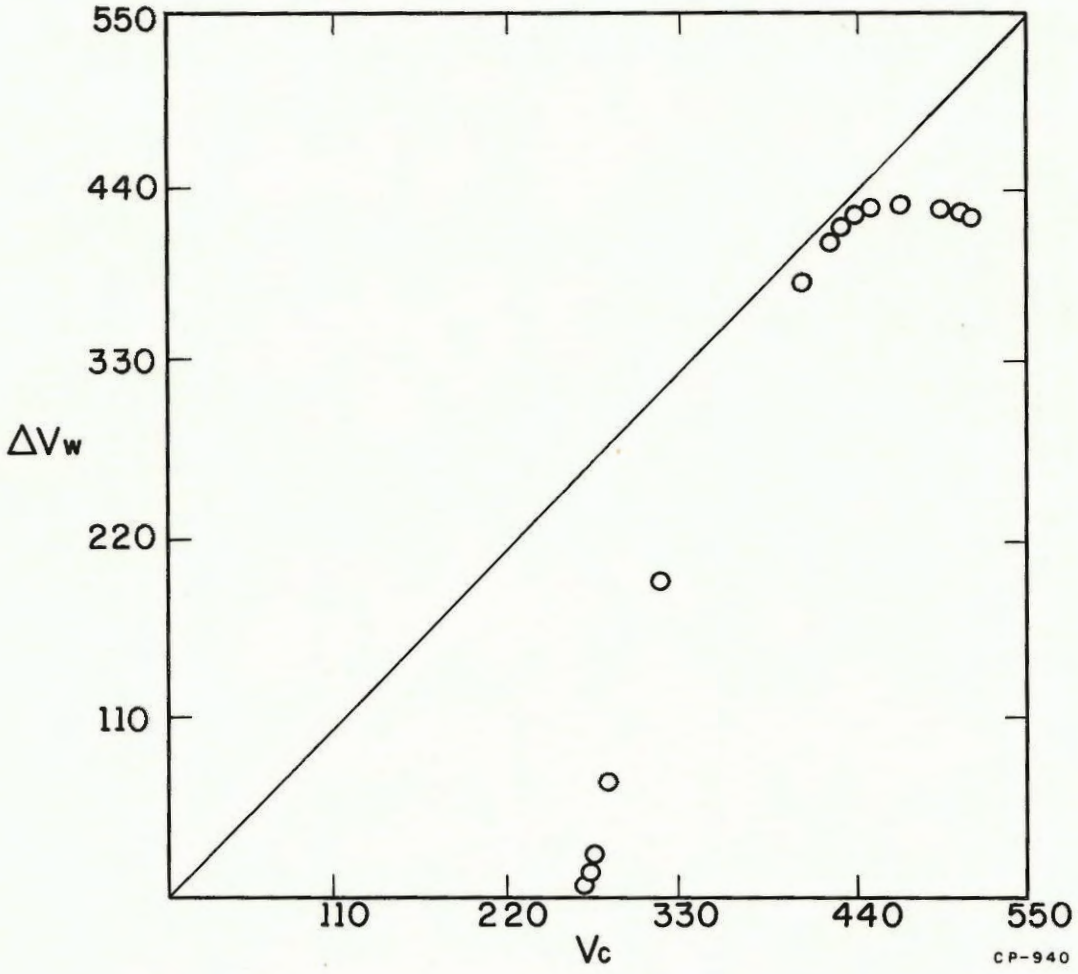

Figure 3.9. Charge transfer curve plotted from the discharge sequence of Figure 3.7.

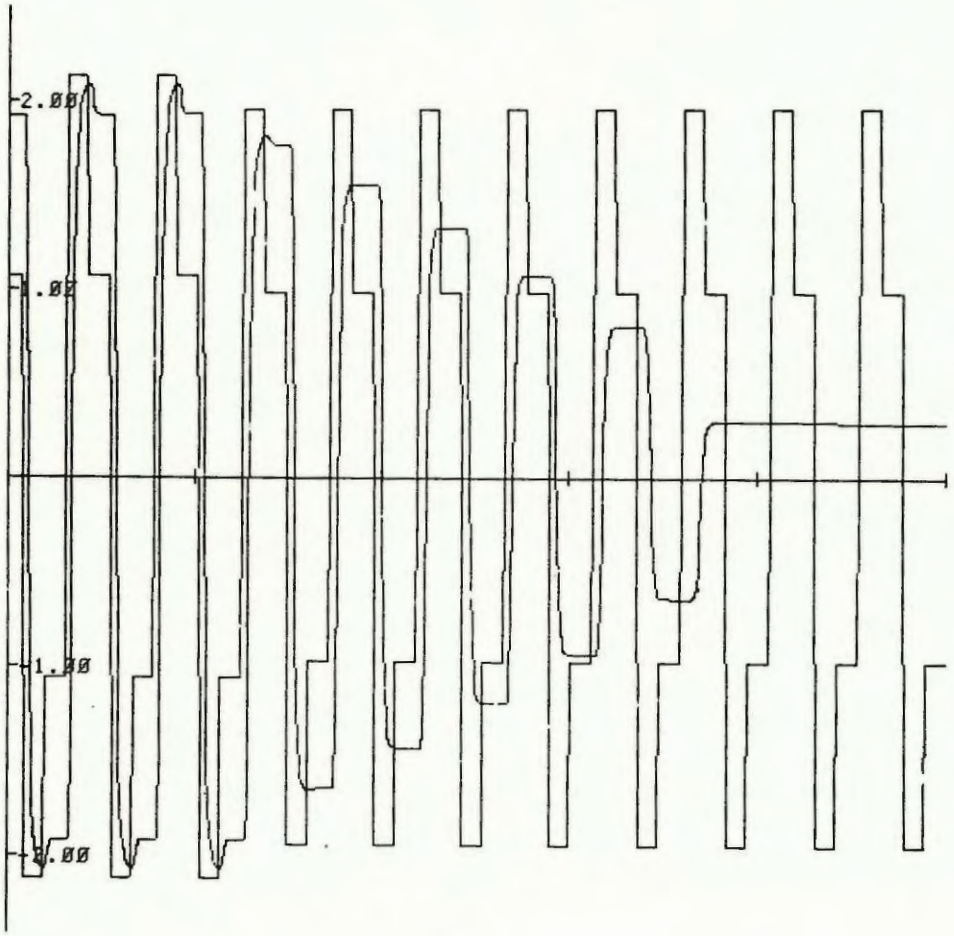

Figure 3.10. Sustain voltage and wall voltage for a decaying discharge sequence. This data is for the same conditions as in Figure 3.7, except the sustain voltage amplitude is reduced.

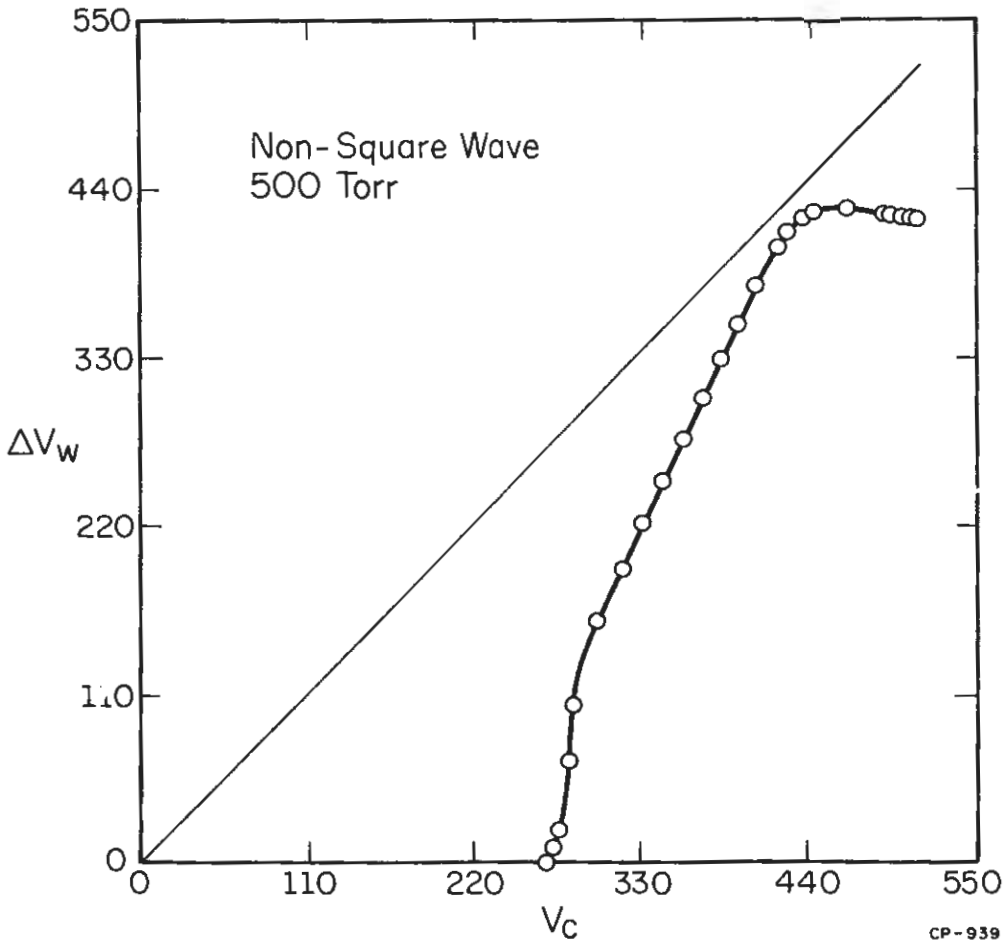

Figure 3.11. Charge transfer curve for the data of Figures 3.7 and 3.10.

The first thing of interest is the large region with slope greater than two near the bottom of the curve. This is a charge transfer curve that will exhibit memory. This shows the existence of the first type of memory mechanism to be discussed in this chapter.

The second point of interest is found in the comparison of the 500 torr curve from the square wave data shown in Figure 3.6 with the curve in Figure 3.11. For convenience these two curves are superimposed in Figure 3.12. These curves are clearly identical in their mid-regions. However, in the lower region there is the significant departure that is the cause for the memory effect in the non-square wave data. The cause for this behavior is discussed in the next section.

3.3.2.1 Discussion of Mechanisms Causing the First Memory Effect

In order to understand the physical causes of this memory mechanism, one must first examine the reason why the transfer curves shown in Figure 3.6 all intersect the V_c axis at the $\mu = 1$ voltage. This is best explained by observing the current growth for sustain voltages near the $\mu = 1$ voltage. Figure 3.13 shows the sustain voltage and discharge current for a slowly growing discharge sequence in which the initial wall charge was zero. The peak sustain voltage is only slightly above the $\mu = 1$ voltage. The current is still very weak since the series has just started. After a number of discharges following those shown in Figure 3.13, the series develops into a very strong on type discharge.

A better way to observe this current growth is to plot the log of the absolute value of the current as shown in Figure 3.14. Here it is seen

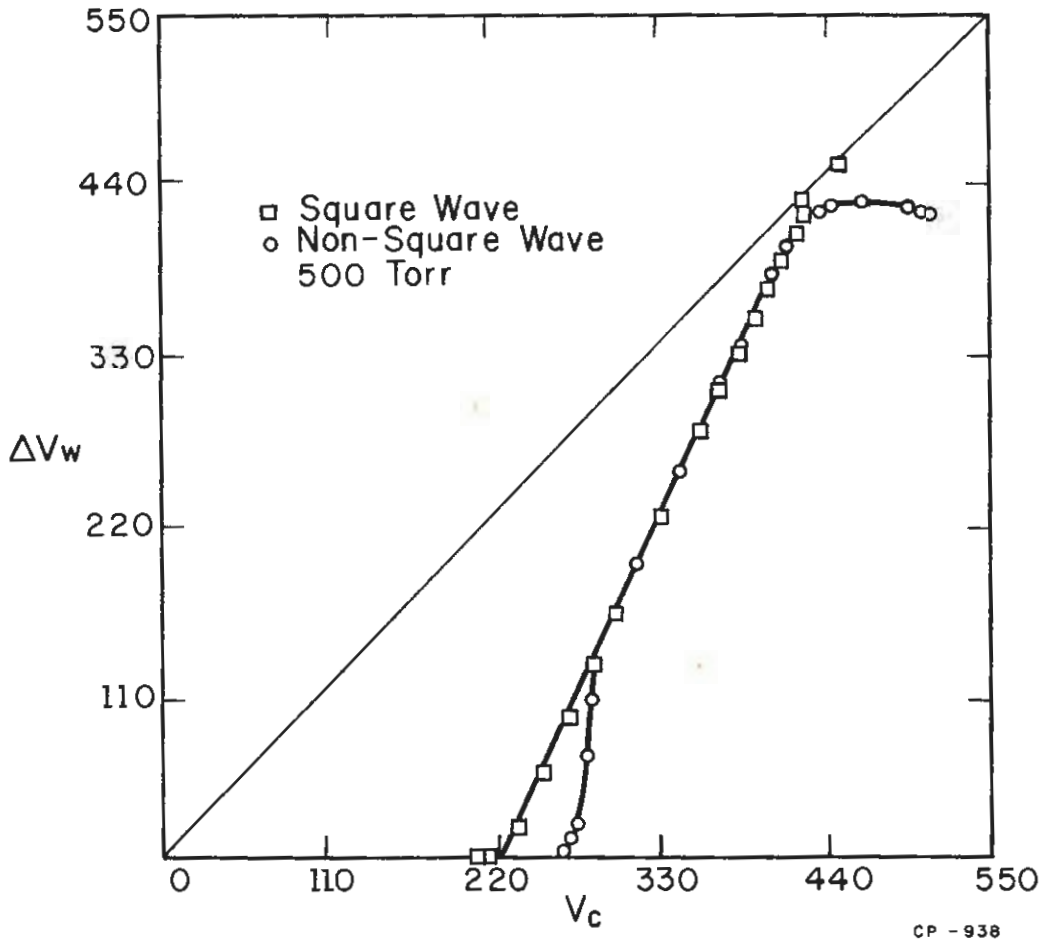

Figure 3.12. Comparison of the charge transfer curve of Figure 3.11 and the 500 torr curve of Figure 3.6.

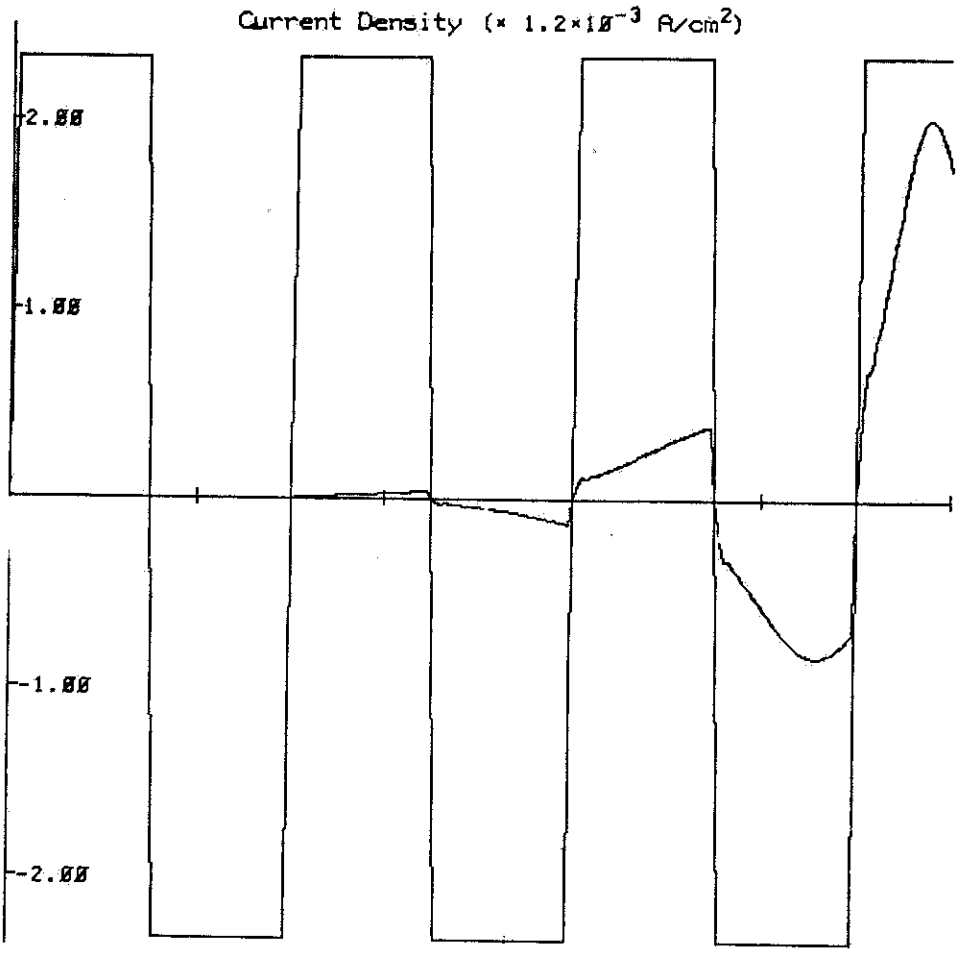

Figure 3.13. Sustain voltage and discharge current for a growing discharge sequence. The vertical scale factors are 100 volts and 1.2 x 10^{-3} A/cm^2. The gas pressure is 500 torr. The peak sustain voltage is 233 volts.

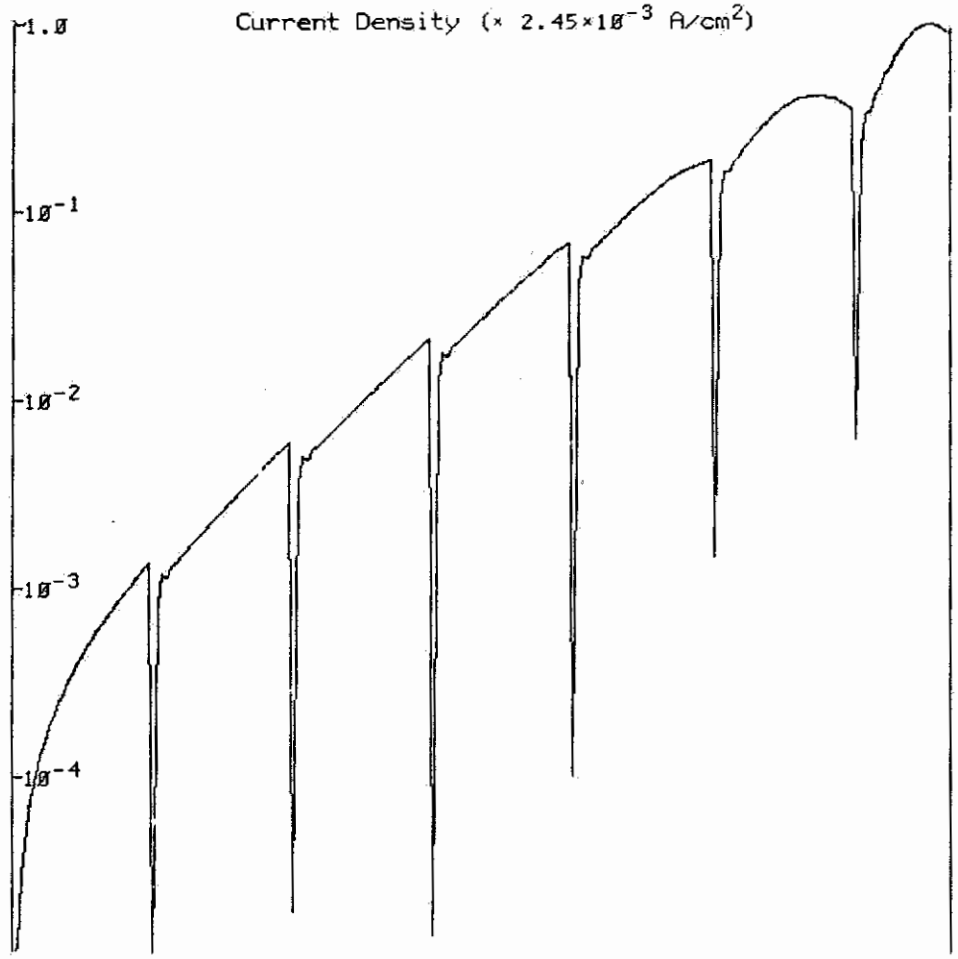

Figure 3.14. Log of the absolute value of the discharge current shown in Figure 3.13. The 1.0 scale point corresponds to 2.45×10^{-3} A/cm^2. The horizontal scale is the same as in Figure 3.13.

that the 2nd, 3rd, and 4th discharges have nearly the same exponential growth rate. The 5th and 6th discharges show the effects of wall charge. The exponential growth is as predicted by simple Townsend discharge theory [18]. What is most interesting is the fact that even though the exponential growth is interrupted when the sustainer reverses polarity, the magnitude of the reversed current is almost equal to the magnitude of the current before reversal. Thus, it seems as if the growth of the magnitude of the current in the early stages of the discharge series would be almost identical for both the AC case shown in Figure 3.13 and a discharge with a DC voltage of the same magnitude.

The reason for this becomes clear when one considers that for the case of a uniform, constant electric field, the total discharge current is proportional to the electron current at the cathode. For all the cases presented in this work, the electron cathode current is due to ejection of electrons by ion impact. Thus the total current is proportional to the ion density. Observation of the ion density for this discharge sequence shows this statement to be true. When the sustain voltage reverses quickly, most of the ions created by the previous discharge are not swept out of the volume but simply change direction. After a few ion transit times (200 ns), the ion distribution looks the same as before the sustainer reversal, but inverted in space. Thus, since ions have a low velocity, the sustain reversal does not strongly affect their population; thus, the magnitude of the discharge current can pick up almost where it left off.

Since the growth in the magnitude of the current in the AC discharge is almost identical to the current growth in the DC discharge, it is quite

reasonable that both cases have the same firing voltage. Thus, all of the charge transfer curves shown in Figure 3.6 should intersect the $\mu = 1$ voltage on the V_c axis. Figure 3.15 shows the magnitude of the current for 27 discharges in which the sustain voltage was three volts lower than the case of Figure 3.14. This sequence does not lead to a strong on discharge, and would normally be considered off to most observers. The sustain voltage of Figure 3.15 is below the $\mu = 1$ voltage, where as that of Figure 3.14 is above.

Figure 3.16 shows the discharge current for the type of sustain waveform that gave the transfer curve in Figure 3.11. The discharge current grows nearly exponentially when the sustainer is at 233 volts, but then falls abruptly when the sustainer goes to 116.5 volts. The important behavior is more clearly seen in the log of the current magnitude shown in Figure 3.17. While the sustainer is at 116.5 volts, the current falls to a constant value of 10^{-8} A/cm^2. This current is due to the very small cathode current j_o in equation (2.4) that is needed to start the discharge process going. By comparing Figures 3.14 and 3.17, one can clearly see that the sustain waveform of Figure 3.8 will not cause the discharge sequence to grow to an on state even though the peak sustain voltages for the cases of Figure 3.14 and 3.17 are both 233 volts. When the sustain voltage falls to 116.5 volts, all of the ions are swept out of the volume and are not regenerated, since $\mu \ll 1$. The only remaining current is due to j_o, as discussed above. Without an accumulation of ions from one discharge to the next, the sequence of Figure 3.17 cannot grow as does the one of Figure 3.14.

The peak sustain voltage was raised to 250 volts, as shown in Figure 3.18, and the ions were still swept completely out of the volume

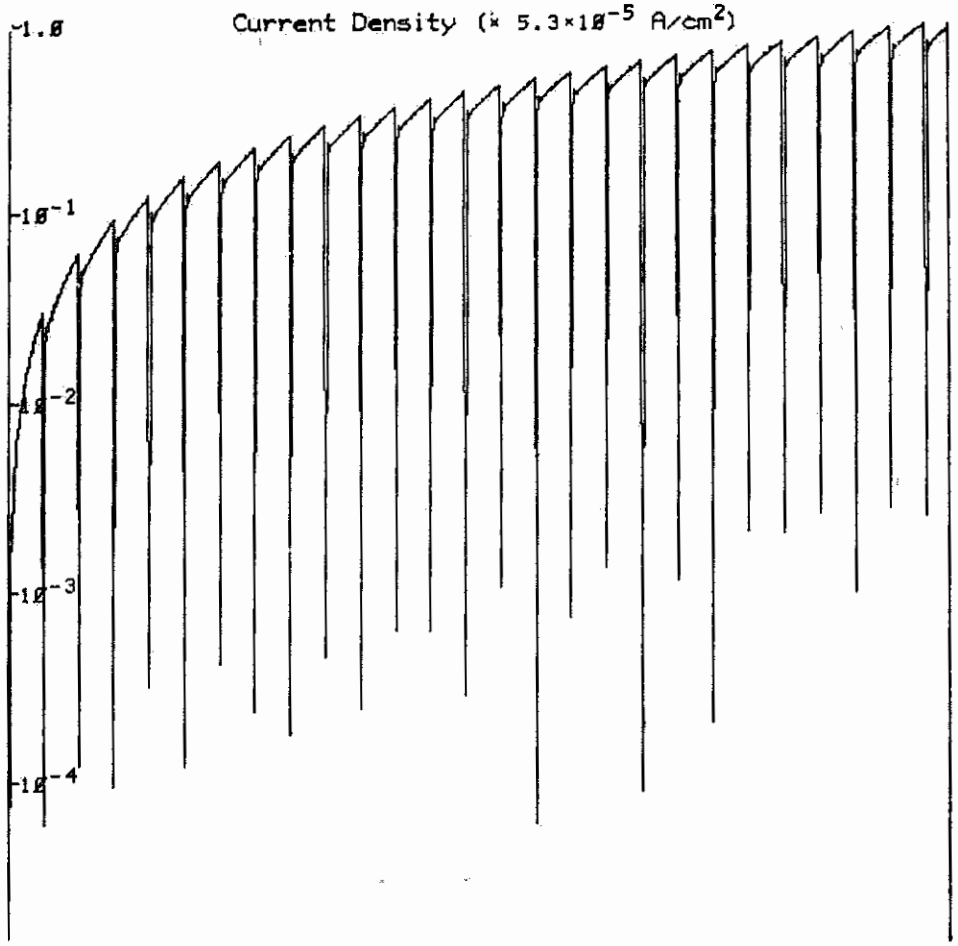

Figure 3.15. Log of the absolute value of the discharge current for a sequence of 27 discharges. The peak sustain voltage is 230 volts. Each discharge corresponds to a 3 μs half sustain period. The vertical scale mark at 1.0 corresponds to 5.3×10^{-5} A/cm^2.

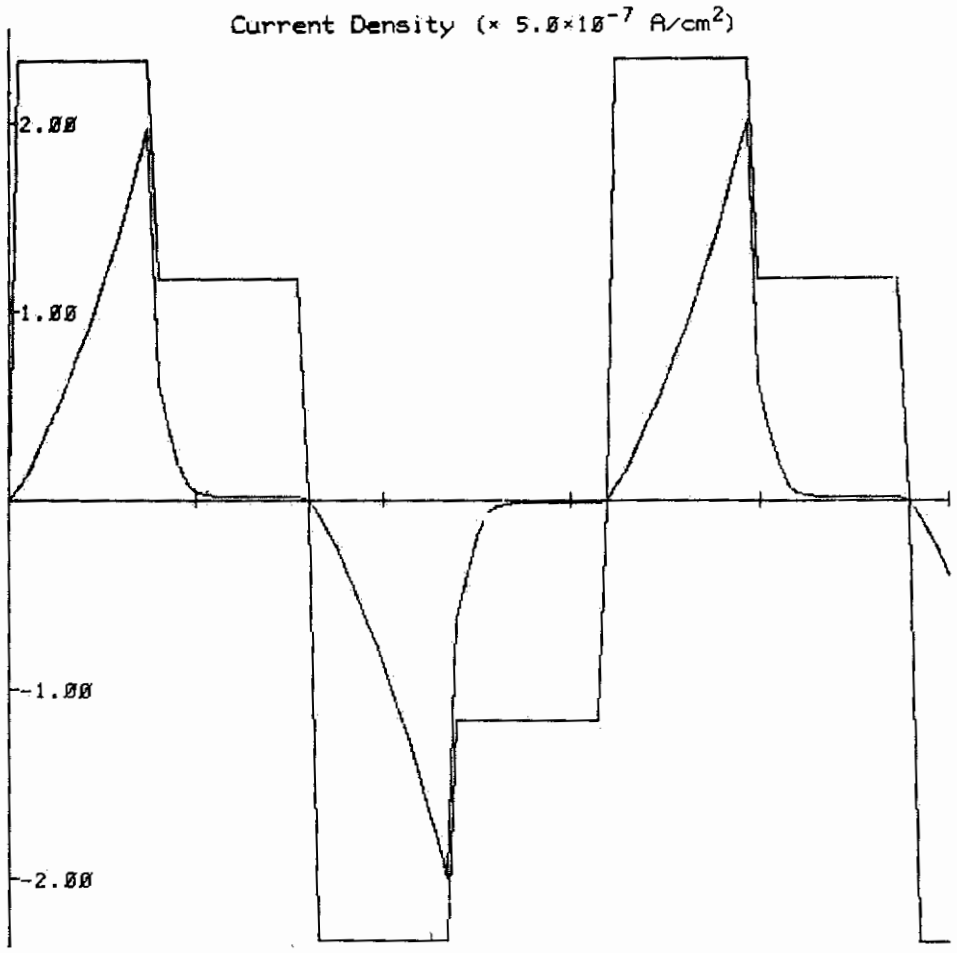

Figure 3.16. Sustain voltage and discharge current for 3 discharges having a non-square wave sustain waveform. Other conditions are the same as in Figure 3.13. The vertical scale factor is 5 x 10^{-7} A/cm^2. Each half cycle is 3 μs. The peak sustain voltage is 233 volts.

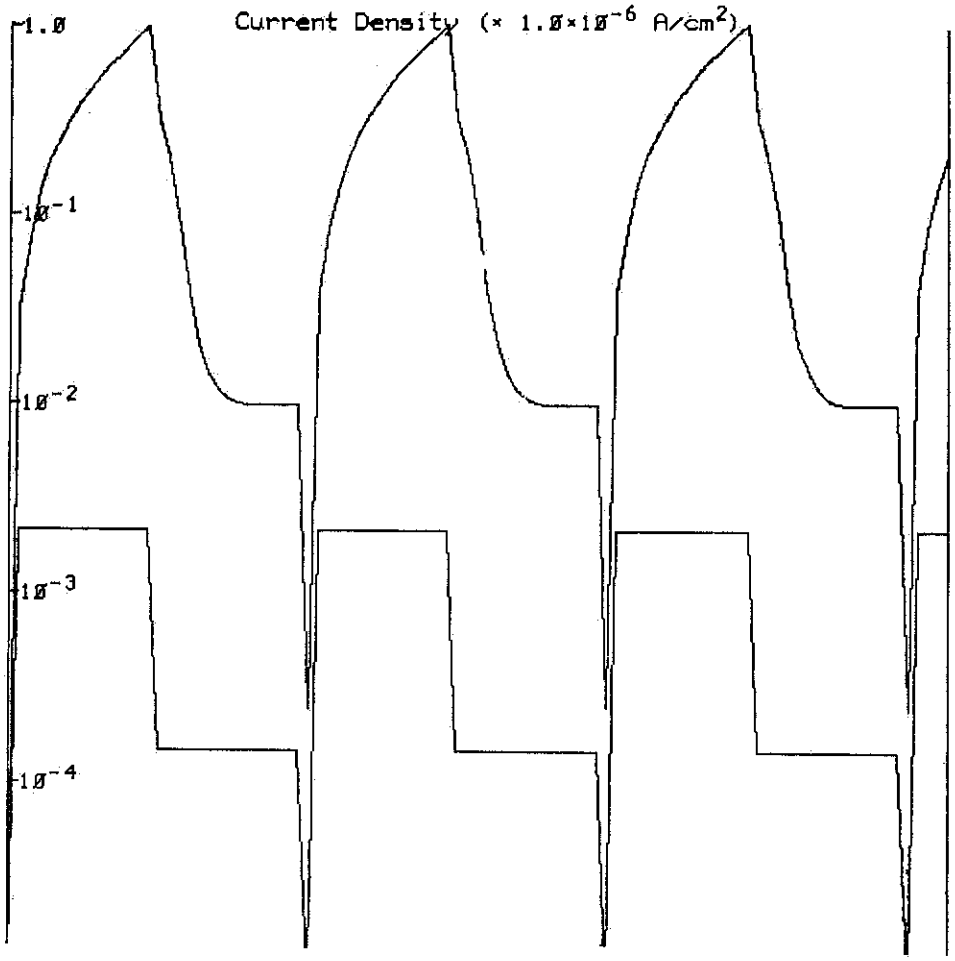

Figure 3.17. Log of absolute value of the discharge current shown in Figure 3.16. The vertical scale mark of 1.0 corresponds to 10^{-6} A/cm^2. The lower curve is the absolute value of the sustain voltage plotted on a linear scale.

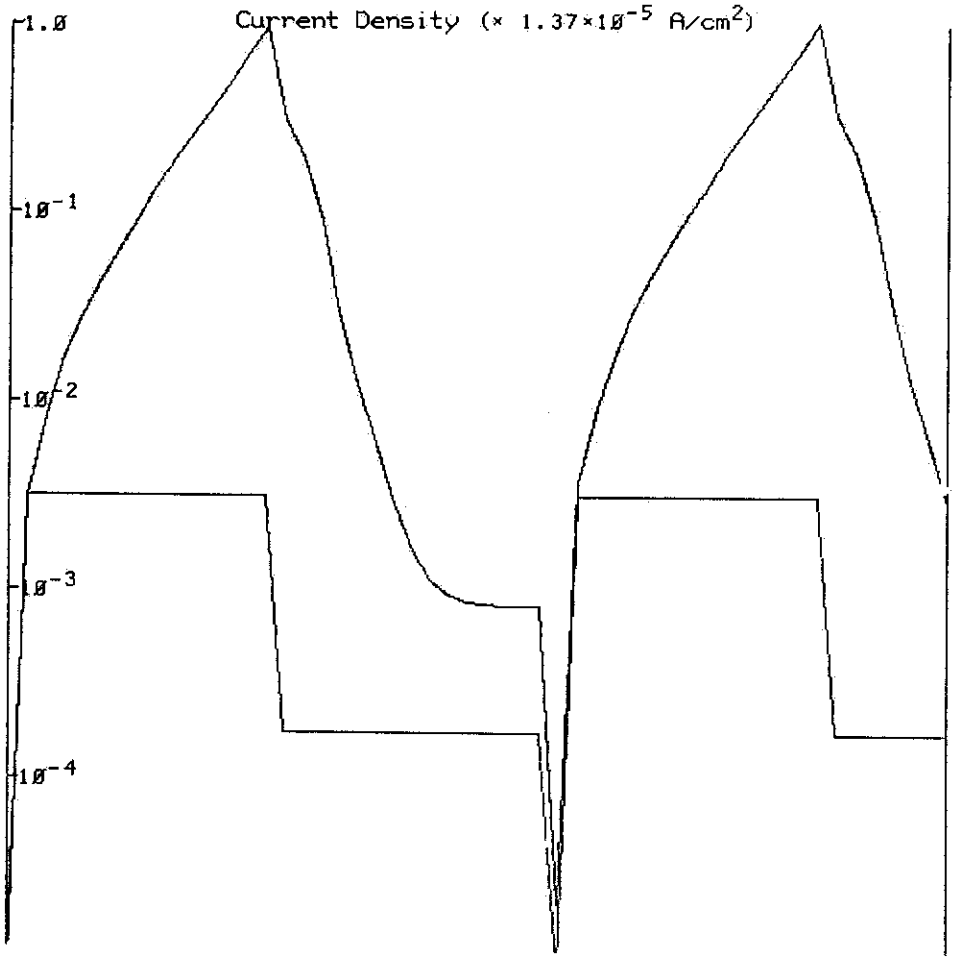

Figure 3.18. Log of absolute value of discharge current with the applied peak sustain voltage of 250 volts. The vertical scale mark of 1.0 corresponds to 1.37×10^{-5} A/cm^2. The lower curve is the absolute value of the sustain voltage plotted on a linear scale.

before the next discharge. Figure 3.19 shows similar data with the sustain voltage raised to 275 volts. At this voltage, $\mu = 2.6$, and the current grows more than 5 orders of magnitude. However, this discharge sequence has stabilized in the off state because most of the ions are swept out when the sustain voltage is at 137.5 volts. 275 volts is, however, just below the firing voltage with this type of sustain waveform.

The wall voltage change in this case is about 1% of the cell voltage, V_c. If ΔV_w gets very much larger, it will start to have a significant effect on V_c for the next discharge and will cause the discharge sequence to grow. This greater ΔV_w can be achieved by increasing V_s or by increasing j_o. The j_o dependence is due to the fact that the exponential growth of current initiates from a current value proportional to j_o. If j_o increases by some factor, then the current for the exponential growth period increases by that same factor [18]. For the data of Figure 3.19, $j_o = 4 \times 10^{-9}$ A/cm^2. This small current was doubled to 8×10^{-9} A/cm^2, which is still about 8 orders of magnitude smaller than the peak current observed for on plasma display cells. The resulting data is shown in Figure 3.20. Doubling j_o caused a doubling of ΔV_w for the first discharge. The larger wall voltage adds to the V_c for the next discharge. For this sequence, the additional wall charge is significant enough to cause a more intense discharge. The sequence continues to grow as additional wall charge builds up from discharge to discharge. The wall voltage for the sequence shown in Figure 3.20 is found in Figure 3.7. This is also the same data as used to obtain the charge transfer curve found in Figure 3.11.

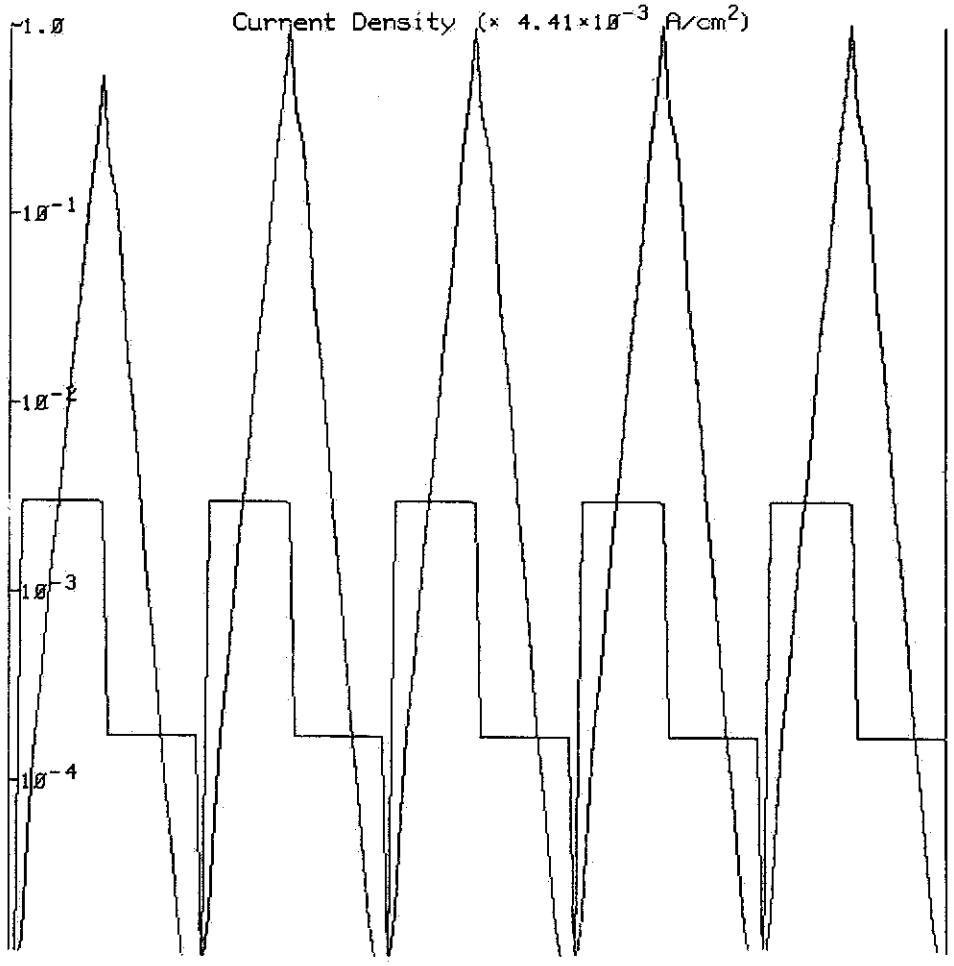

Figure 3.19. Log of the absolute value of discharge current when the peak sustain voltage is 275 volts. The vertical scale value of 1.0 corresponds to 4.41 x 10^{-3} A/cm^2.

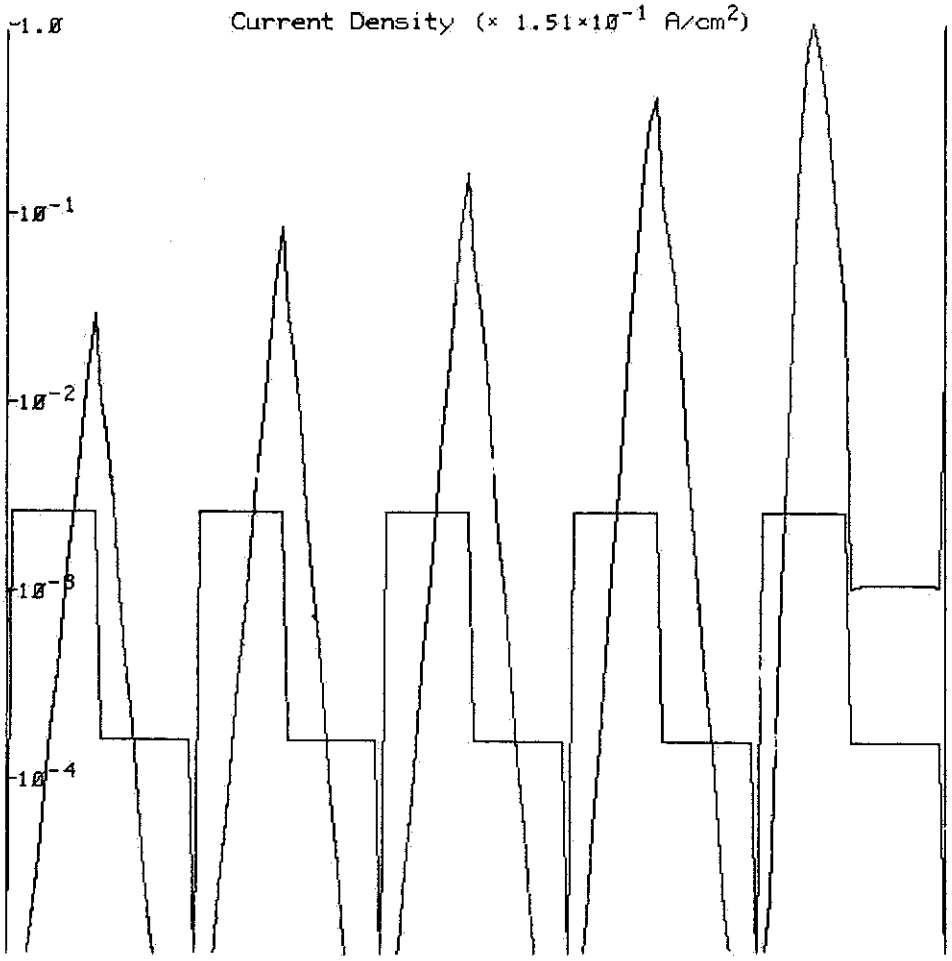

Figure 3.20. Log of the absolute value of the discharge current for the conditions of Figure 3.19, but with the value of j_o doubled. The 1.0 scale value corresponds to 1.51×10^{-1} A/cm^2.

To summarize, the above discussion and data has shown that the growth of a discharge series depends on both ion accumulation in the volume and charge accumulation on the wall. For pure square wave sustainers, both ions and wall charge are very important for the determination of the lower portion of the charge transfer curves like those in Figure 3.6. If the sustainer is changed to look like that in Figure 3.8, the ions will not be able to accumulate. With only the wall charge able to accumulate from discharge to discharge, the sustain voltage will have to become quite high before significant wall charge is collected from cycle to cycle. This is seen in Figure 3.12. Also, with this type waveform, the shape of the lower part of the charge transfer curve will be strongly dependent on j_o.

The upper portions of both transfer curves shown in Figure 3.12 are nearly equal. This is because only wall charge accumulation is important in this region. The value of μ is so great in this region, that even for very small values of j_o or ion density, the discharge can grow very rapidly and be complete before the fall of the sustain pulse. Thus, it makes little difference whether or not ions are present from previous discharges. Also, since the discharge completes itself very quickly, there is little difference between the 3 μs pulse of the square wave and the 1.5 μs pulse of the waveform in Figure 3.8. However, in the upper regions of the curve near the slope = 1 line, the short 1.5 μs pulse width does make a difference; and the wall voltage is reduced by a small discharge after the fall of the sustainer. This is seen in Figure 3.7 and in the early discharges of Figure 3.10. This causes the transfer curve to bend over as seen in Figure 3.12.

3.3.3 Case of Square Wave Sustainer with Field Distortion

All of the above discussions have had the effects of field distortion removed. This was done for convenience in order to separate the effects due to field distortion from those that are not. In actual plasma panels, the field distortion is rather severe, as shown in Figure 2.8. Since the charge transfer curve for a square wave is not complicated by the shortage of ions, as discussed above, square waves are chosen for the detailed field distortion study.

Figures 3.21, 3.22, 3.23 and 3.24 show the charge transfer curves for a series of discharges at 300, 400, 500 and 700 torr. For convenience, the curves found in Figure 3.6, having no field distortion, are superimposed on those with field distortion. From these figures it is clear that for the lower area of the curve, the two cases give the same results. This is reasonable since even when field distortion is included in the calculations, the weak discharges do not have sufficient ion and electron density to distort the field significantly.

The results in the mid and upper sections do not agree. For low pressures the field distorted curve goes to the right of the non-field distorted curve. For higher pressures, the field distorted curve goes to the left of the non-field distorted curve. This gives rise to an unstable region of the transfer curve; thus, a second memory mechanism is found.

3.3.3.1 Explanation of Second Memory Mechanism

This second memory mechanism appears to be very similar in nature to the memory effect found in DC discharges. The DC effect is dependent on

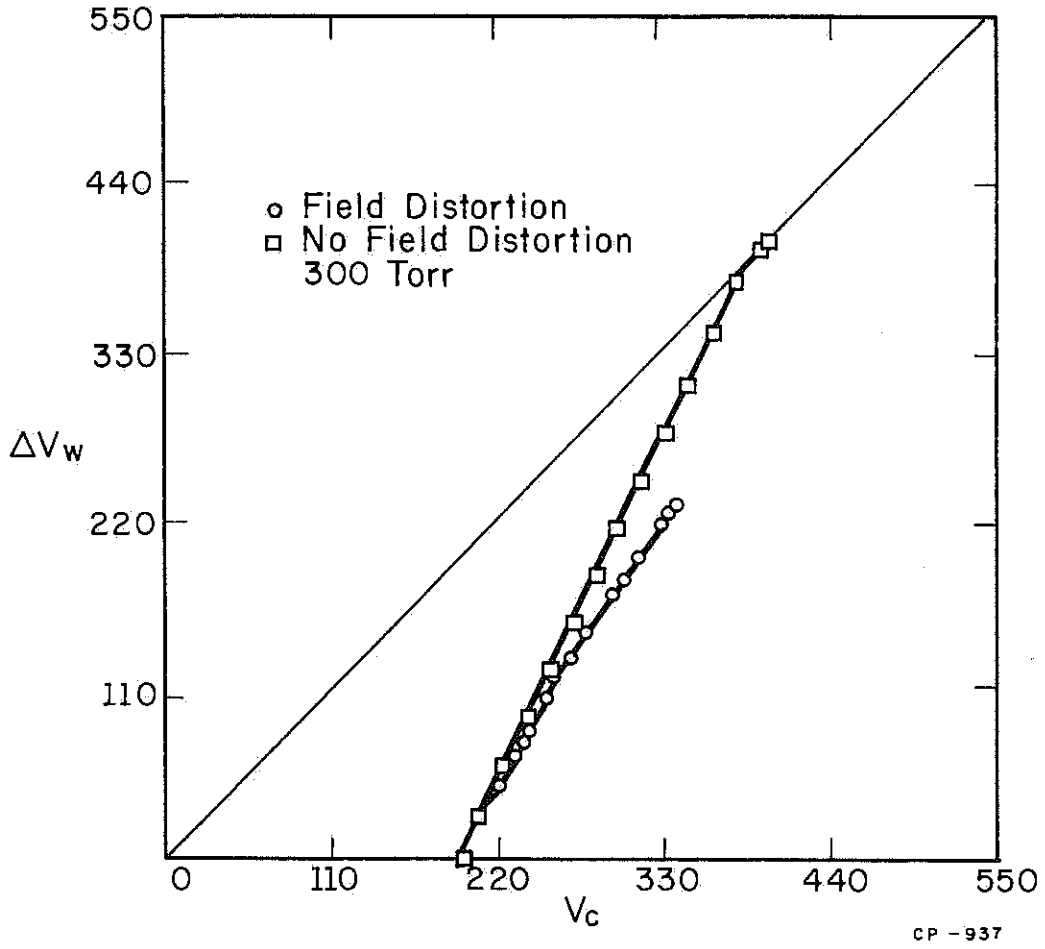

Figure 3.21. Charge transfer curve for 300 torr pressure, showing the effects of field distortion for a square wave sustainer.

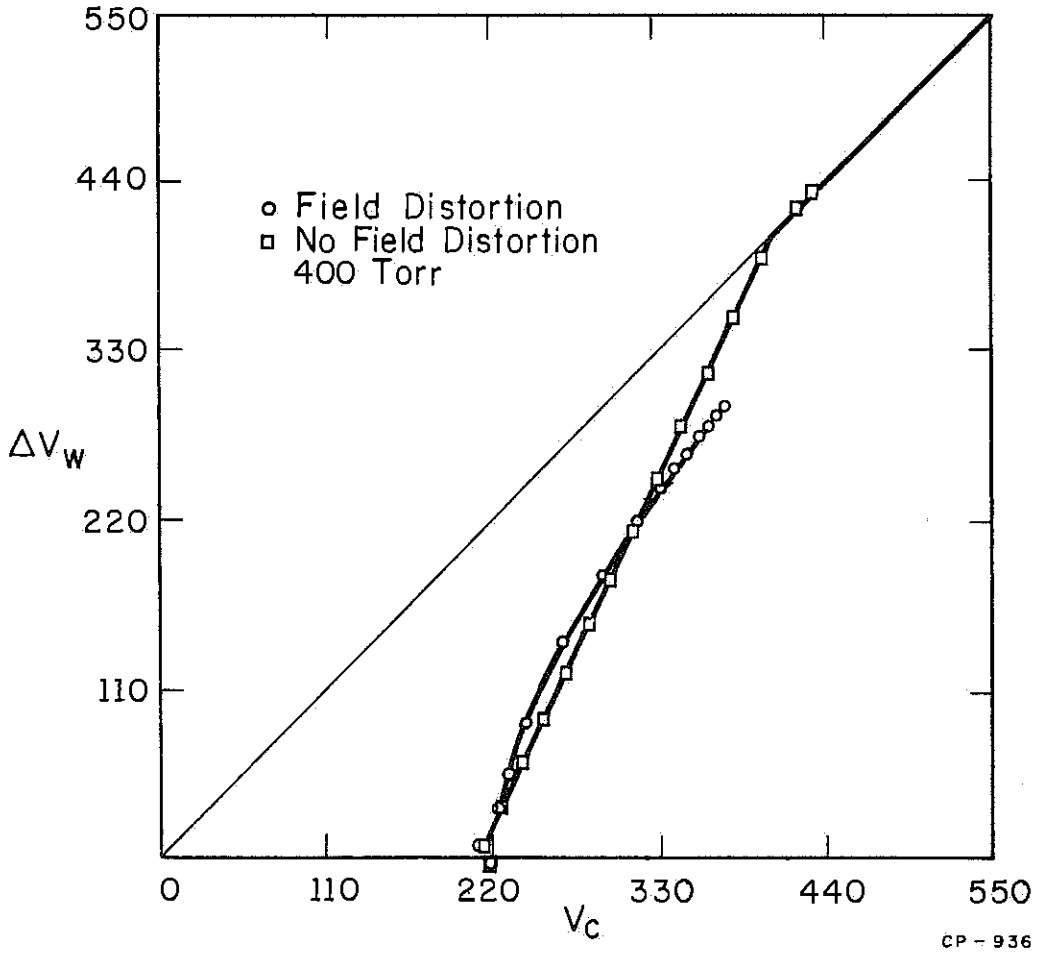

Figure 3.22. Charge transfer curve for 400 torr pressure, showing the effects of field distortion for a square wave sustainer.

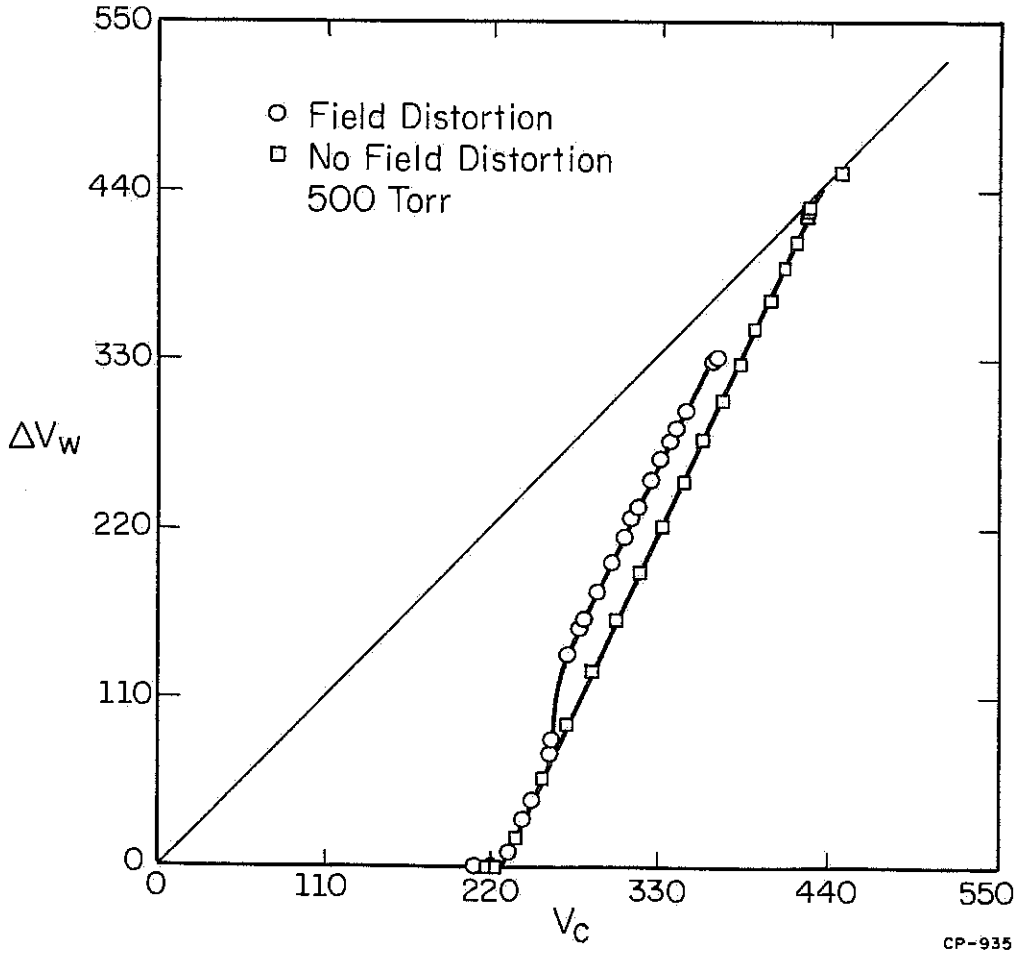

Figure 3.23. Charge transfer curve for 500 torr pressure, showing the effects of field distortion for a square wave sustainer.

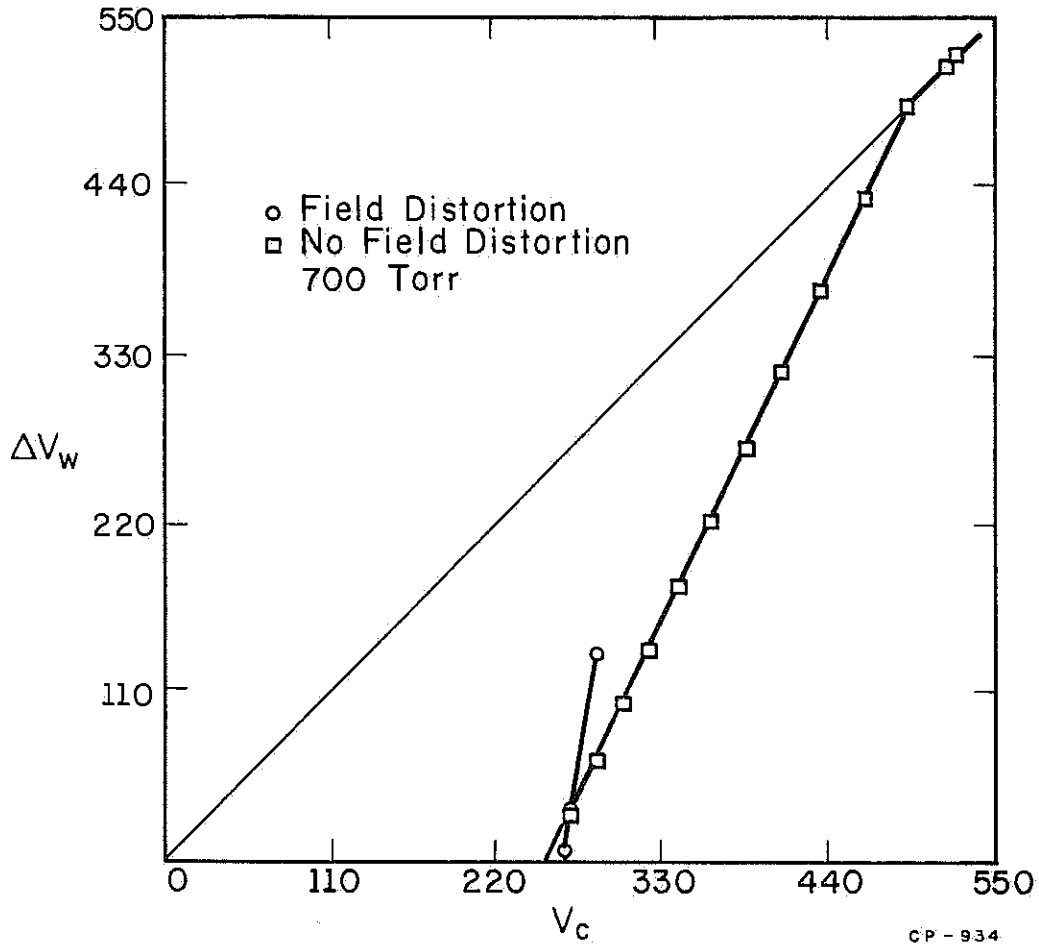

Figure 3.24. Charge transfer curve for 700 torr pressure showing the effects of field distortion for a square wave sustainer. The field distorted curve is incomplete because the following discharge was so intense that the calculation blew up.

field distortion caused by ions and electrons near the anode to increase the electric field near the cathode. If the proper conditions are met, the external voltage can be lowered below the initial firing voltage and still maintain a discharge. In a sense, the field distortion of the ions and electrons at the anode cause the effective anode to move closer to the cathode than the real anode. Thus, the discharge gap is effectively shortened. For the DC discharge to have memory, the firing voltage of the effectively shortened gap must be smaller than the firing voltage of the real gap. The firing voltage can be found from the Paschen curve for the discharge calculations presented in this work which is shown in Figure 3.25. Given the pressure of the gas, the firing or $\mu = 1$ voltage can easily be found with knowledge of the discharge gap, d. In the DC case, in order for the discharge to have memory, the value of d must be large enough so that $pd > pd_{min}$. If this requirement is met, then the shortening of the gap by the ions and electrons at the anode will cause the firing voltage to decrease, giving the desired memory characteristics. An initial pd value less than pd_{min} will not have memory since the firing voltage will increase as d gets smaller.

In the AC plasma display panel, a similar situation occurs. Ions and electrons collect near the anode, as shown in Figures 2.6 and 2.7. If the gas is at the proper pressure, the effectively shortened discharge gap will cause μ to increase. The higher μ will cause greater discharge activity, which will eventually result in greater wall charge transfer. This will cause the field distorted transfer curve to veer to the left, as shown in Figure 3.23.

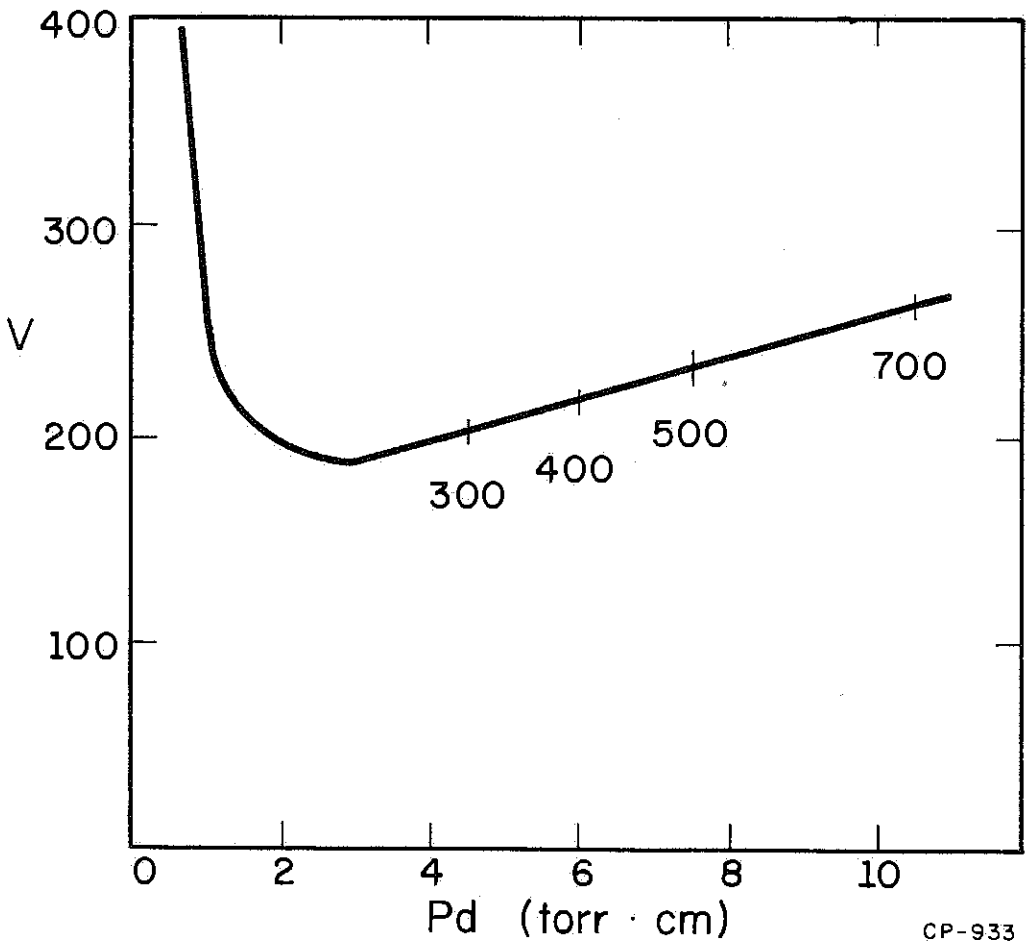

Figure 3.25. Paschen curve for the conditions presented in the computer simulation.

If pd is too small, then the field shortening of the gap will cause μ to decrease and eventually cause less wall charge to be transferred. This causes the transfer curve to veer to the right as shown in Figure 3.21.

The firing voltages for the four pressures used in Figures 3.21 through 3.24 are marked on Figure 3.25, assuming the gap spacing used in these calculations of d = 150 μm. Even though 300 torr is to the right of pd_{min}, the charge transfer curve still veers to the right as seen in Figure 3.21. The 400 torr curve seems to be just enough pressure to cause a small amount of memory. At 500 torr the memory effect is quite strong. Thus the apparent requirement for memory is that pd be appreciably greater than pd_{min}. How much greater is not clear and will have to be the subject of another study.

The data for 700 torr shown in Figure 3.24 is incomplete since the memory effect was very strong causing a very strong discharge to occur. This strong discharge caused the calculations to blow up. Thus, only the first few points of the transfer curve are available. But clearly, the trend of stronger memory effect as the pressure is increased, continues.

The value of $\mu(t)$ is calculated from equation (2.14) with typical results previously shown in Figures 2.14 and 2.15. The growth of $\mu(t)$ following the sustainer rise is due entirely to the effective shortening of the discharge gap. This causes the rate of current growth to increase as seen in Figure 2.13. If the initial $pd < pd_{min}$, then $\mu(t)$ does not rise following the end of the sustain rise.

3.3.4 Case of Non-Square Wave with Field Distortion

From the discussions above, it seems reasonable to expect the transfer curve for this case to act like the non-square wave without field distortion for the lower part of the transfer curve. Similarly one would expect the upper portion of the curve to act very much like the case of a square wave sustainer with field distortion. To test this, a discharge sequence was run at 500 torr for this case. The charge transfer curve is shown in Figure 3.26 along with the data from Figures 3.11 and 3.23 for comparison. It is clearly seen that the above hypothesis is correct for all but the very upper part of the transfer curve. In this region, 1.5 μs is not sufficient time to collect all wall charge and to allow the plasma to die out. Thus, the curve bends over to the right.

3.4 Comparison of These Results to Those of Others

Since the work of Lanza [14] is the only one that presented a calculated charge transfer curve, it should be interesting to compare the two results. To do this, the problem specified by Lanza was set up with Ward's calculational technique. This involved changing the gas mixture and cell geometry, from those used in all results presented up to this point. Lanza used a square wave sustainer and included field distortion. The calculated charge transfer curve is shown in Figure 3.27. In the lower portion of the curve, the slope is equal to 2 and the V_c intercept is at the $\mu = 1$ voltage. Since the upper region veers to the right, it seems as if the value of pd is less than the pd_{min} on the Paschen curve. Figure 3.28 shows the Paschen curve. The value of pd used by Lanza, is indeed much smaller

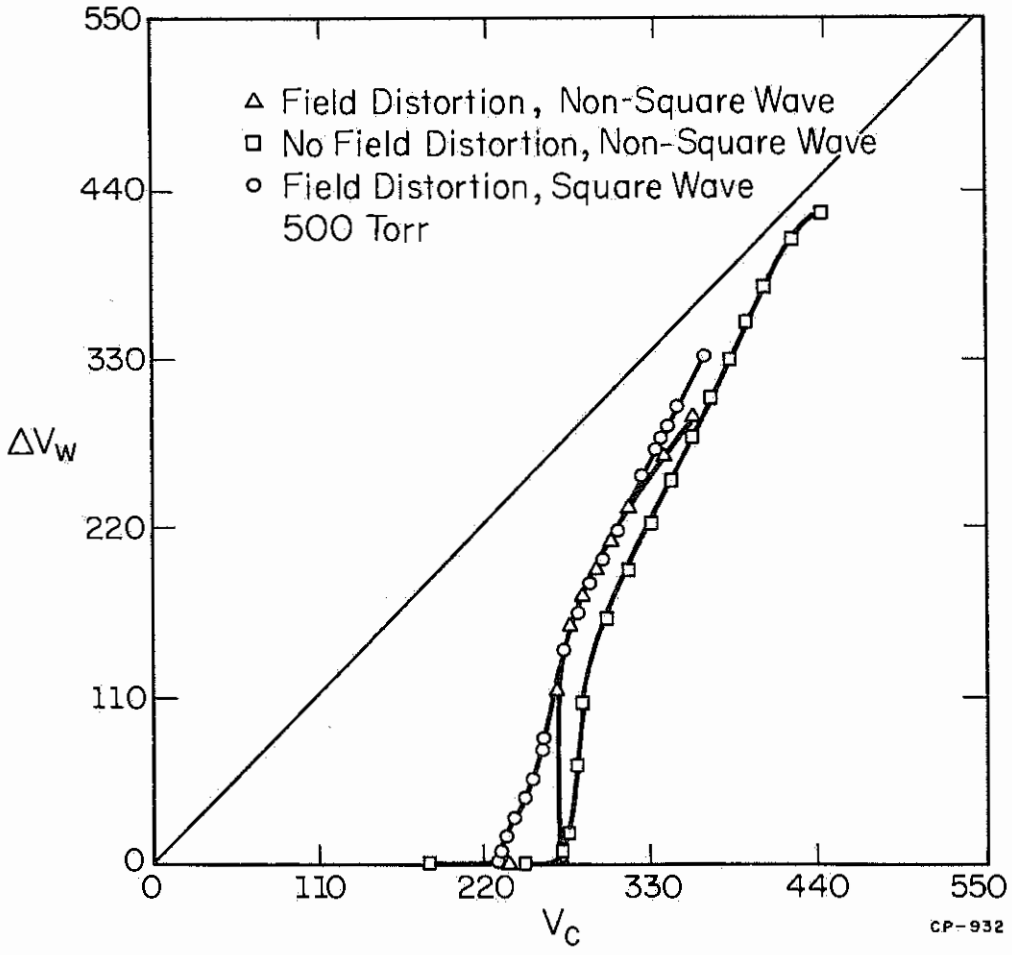

Figure 3.26. Charge transfer curves showing the effects of a non-square wave sustainer and field distortion. Curves for 2 other cases are shown for comparison.

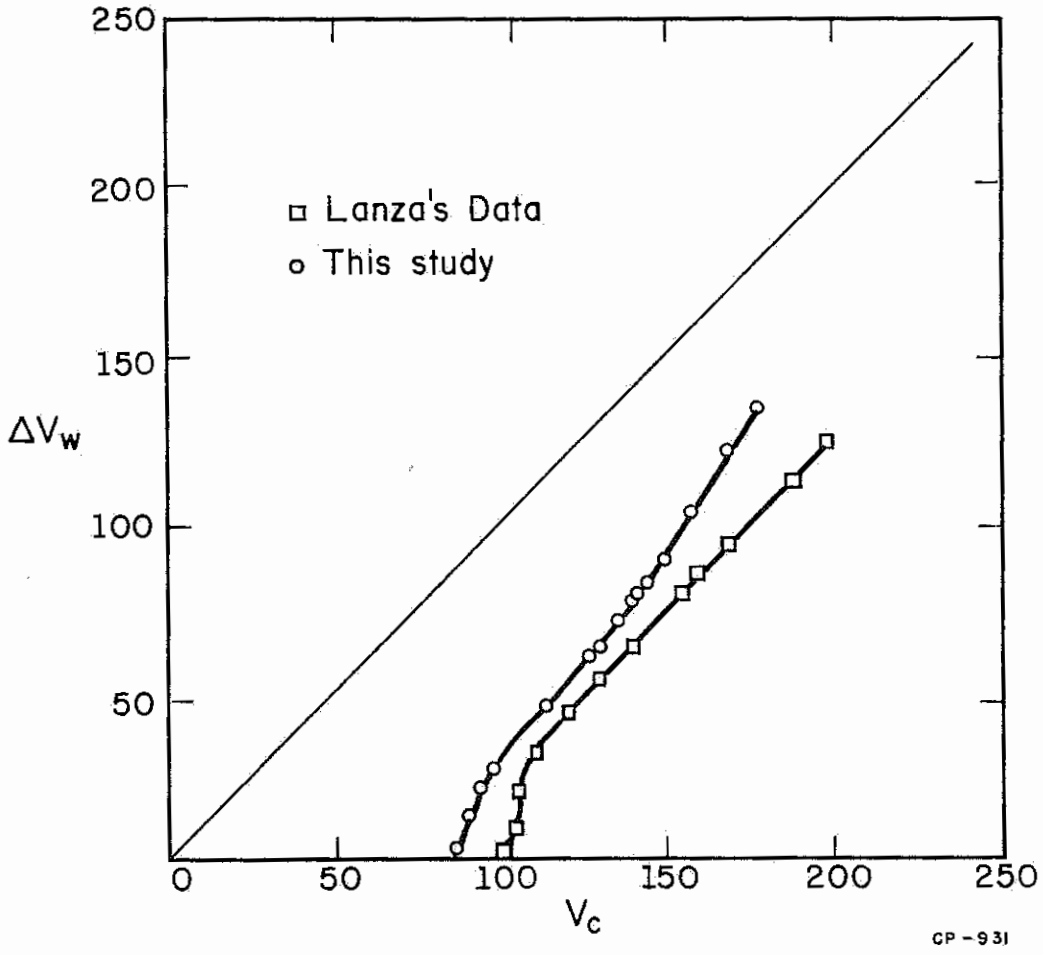

Figure 3.27. Charge transfer curve for the problem specified by Lanza [14]. Lanza's published results and those of this study are plotted for comparison.

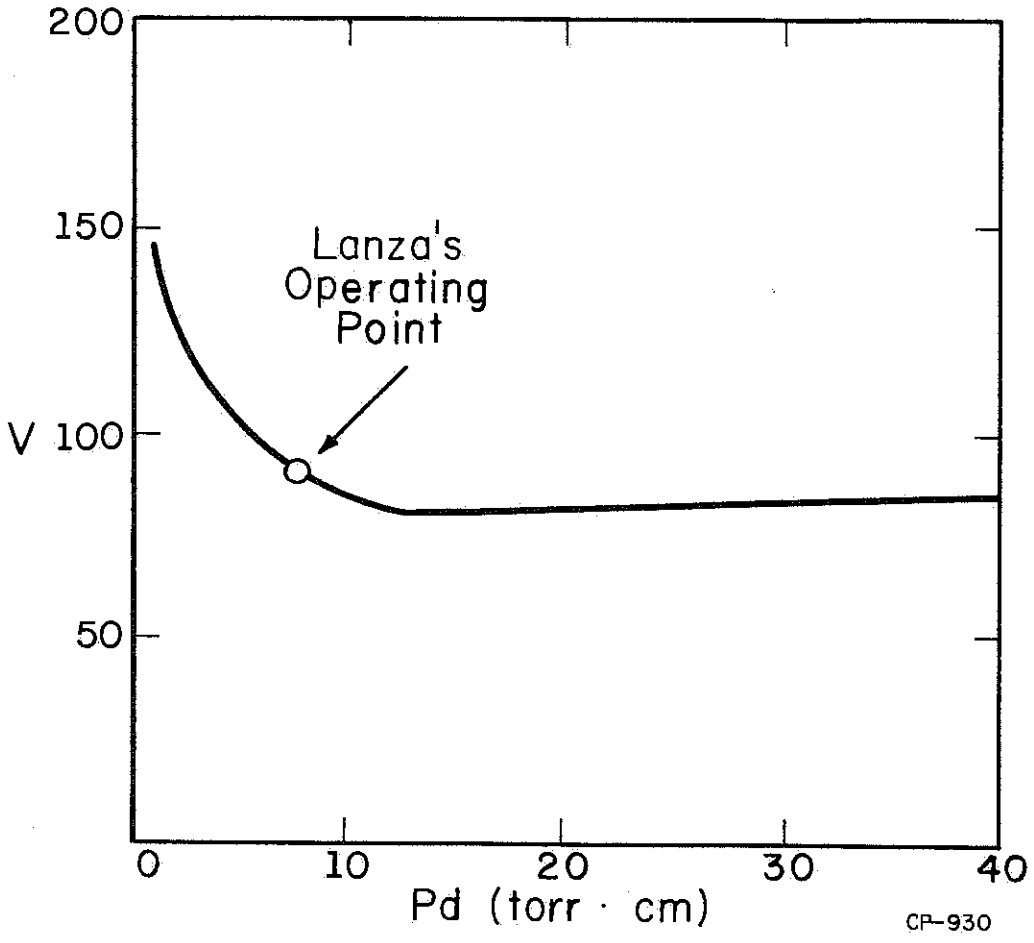

Figure 3.28. Paschen curve for conditions specified by Lanza.

than pd_{min}. Thus the case presented by Lanza does not have memory. More interesting is the fact that from what has been learned in this chapter, one could have determined that this case would not have memory before any computer calculations had been made.

Figure 3.27 also shows the charge transfer curve calculated by Lanza. An interesting question is, why does his curve have a region of slope greater than 2 for a case that does not have memory. The answer lies in the method in which he used to calculate his charge transfer curve. He did not use a long series of discharges to get points on the curve as was done for these calculations. But rather he got his points by applying a sustain pulse of varying amplitudes to find the value of ΔV_w for each new amplitude [23]. Since for each new pulse, the initial ion distribution was nearly zero, the ion density does not build up from discharge to discharge as it should in the case of a square wave sustain sequence. Thus, although Lanza presented his curve as for a square wave sustainer, it is more typical of the curve for a sustain waveform like that shown in Figure 3.8, where the ions are not allowed to build up from discharge to discharge. Thus Lanza's data looks like the curve of Figure 3.11 for the lower regions.

The only other calculational effort that deals with long series of discharges is that of Lay, et al. [13]. They use a non-square wave sustainer and do not include the effects of field distortion. They clearly show that their discharge sequences do have memory. From what has been learned from section 3.3.2, this should be expected. The charge transfer curve should look similar to that found in Figure 3.11. Although Lay, et al. do not present a charge transfer curve for their data, they do give data on

the wall voltages for a growing series of discharges in which the sustain voltage was above firing voltage. From this data, it is easy to construct the charge transfer curve that is shown in Figure 3.29. Clearly, this transfer curve will exhibit memory. It is somewhat similar in shape to the curve of Figure 3.11, however a direct comparison cannot be made. There are three basic differences between the calculation for these two curves. They are the different sustain waveforms used, the different values of γ_i used, and the different treatment of metastables.

The different sustain waveforms will affect the lower portion of the transfer curve. The waveshape for the curve of Figure 3.11 is shown in Figure 3.8. Lay, et al. used the wave shape shown in Figure 3.30. The important difference is that in one case the sustainer goes to zero for a long period, where as for the other case, the sustainer only goes to half the peak sustain voltage. When the sustain voltage is zero and there is zero wall charge, there will be no field across the gas and thus the ions will not be swept out of the gap. Thus for the waveform of Figure 3.30, the ions can accumulate from cycle to cycle until the discharge grows strong enough to sweep out most of the ions during the period when the sustain voltage is zero. The ions will still be swept out between major sustain pulses by the field produced by the wall charge that results from the weak discharge process. Thus, a reasonable size discharge must occur each cycle in order to maintain the cell in the off state. This small discharge shows up in the data of Lay, et al. when the sustain voltage is just below firing voltage. For this off condition, they indicate a ΔV_w of more than 30 volts. Results similar to these were seen when the calculations used in this study were used with

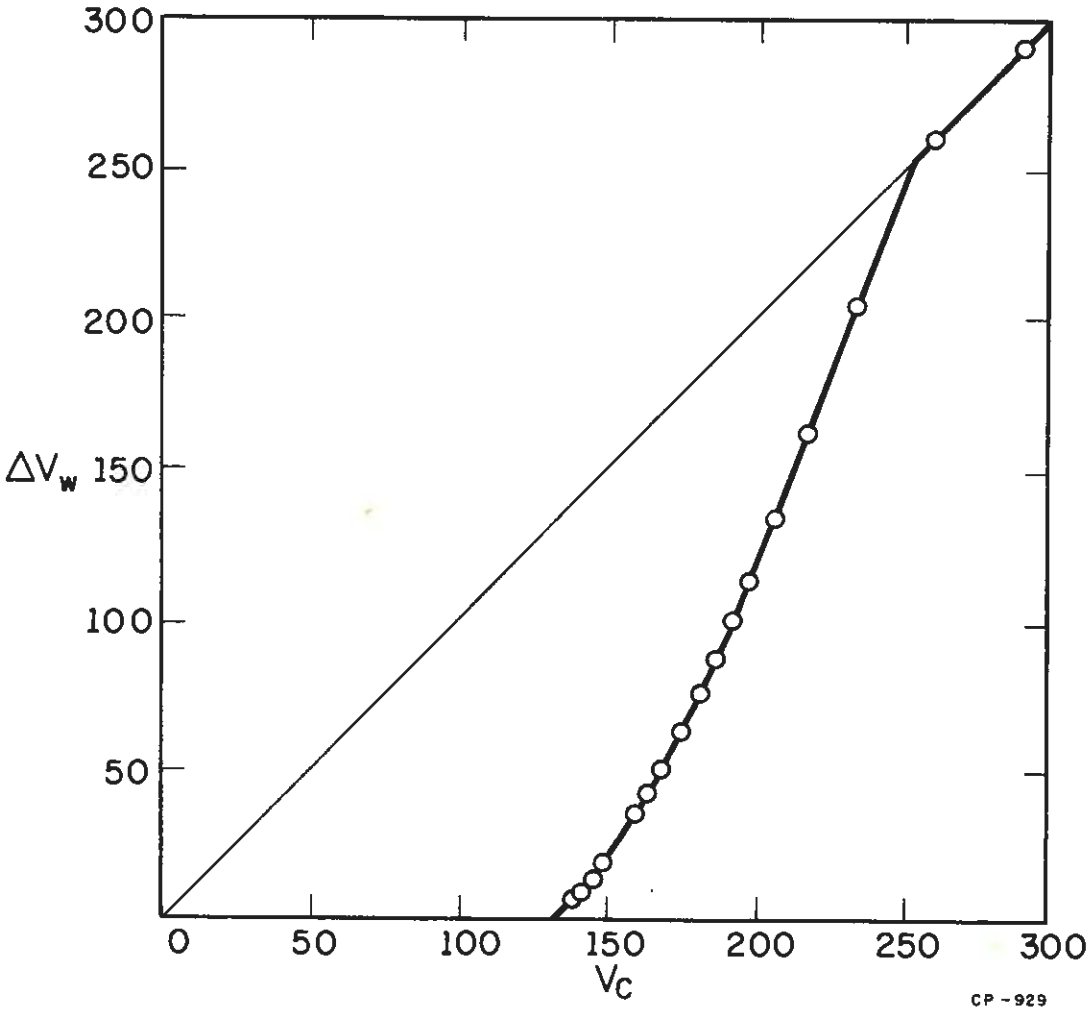

Figure 3.29. Charge transfer curve constructed from data presented by Lay et al. [13].

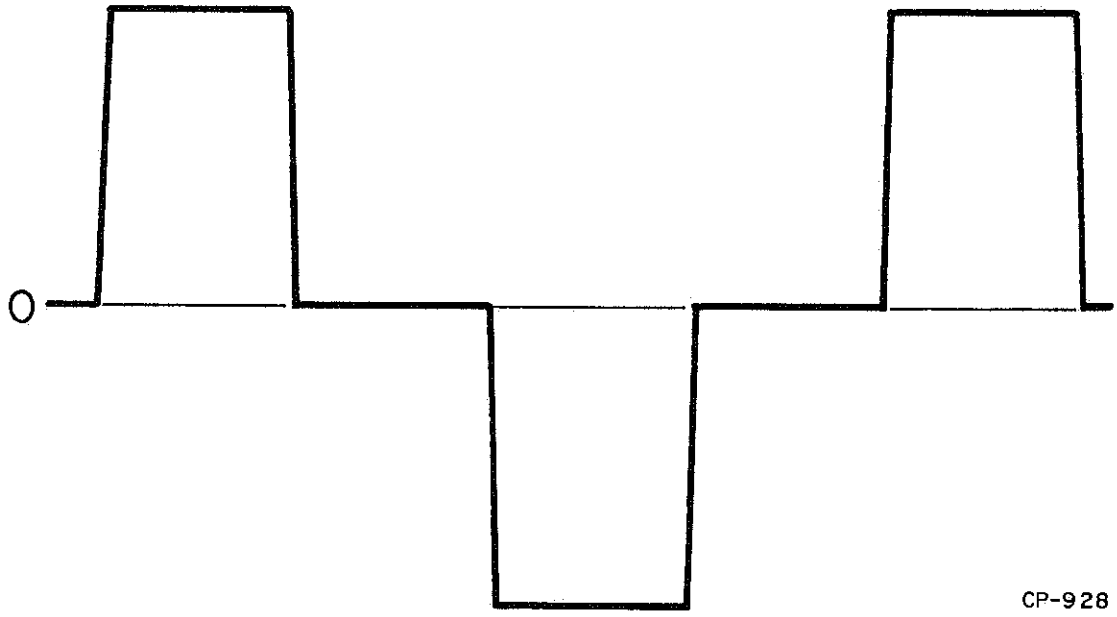

Figure 3.30. Sustain voltage waveshape used in the calculations of Lay et al. [13].

return to zero waveforms. This type of waveform causes the slope of the transfer curve in the lower regions to be less than two. This is clearly seen in Figure 3.29 but is absent in Figure 3.11. Thus, it is better to return the sustain pulse to some voltage between the peak voltage and zero. This will help the off cells remain in a nondischarging condition.

The second major difference between the calculation of Lay, et al. and those presented here is in the value of γ_i used. These calculations used a constant $\gamma_i = 0.06$. However, γ_i is usually not constant in gas discharges because of back diffusion of electrons at the cathode [24]. This usually makes γ_i a function of E/p at the cathode. Lay, et al. chose $\gamma_i = 0.01(E/p)^{0.533}$. This means that for the upper regions of the transfer curves of Figure 3.27 where $V_c \simeq 300$, $\gamma_i \simeq .12$. In the lower regions of the curve $\gamma_i = 0.09$. This variable, γ_i, should have an effect on the charge transfer curve. Although no calculations have been made, it is likely to cause transfer curves such as those shown in Figure 3.6 to have a slope greater than 2. This is due to the fact that a higher γ_i in the upper part of the curve should cause more ΔV_w than the lower γ_i for the lower regions of the curve. Thus, the effects of back diffusion at the cathode could be considered a third memory effect. The slope greater than 2 region of the curve in Figure 3.29 must be attributed to both the back diffusion effect and the effect of having a non-square wave sustainer. The question of how important back diffusion is in actual plasma panels is a matter for further study. All values of γ_i, whether variables or constant, have been determined from guess work in all calculations performed on the AC plasma panel. The problem is that there have not been sufficient experimental determination of γ_i for glass surfaces and dielectrics.

The third difference between the two sets of calculations is in the effects of metastable Ne atoms. Lay et al. have included the effects of metastables, whereas the calculations presented here have not. How the effects of metastables change the charge transfer curve is not clear. Lay and Chu [25] have shown that metastable effects have a certain delay time associated with the build up of the metastable population. The Ne metastables can cause additional ion electron pairs to be created due to the well-known Penning effect. This serves to increase α and thus lowers the firing voltage. However, because of the time delay associated with this effect, the effective α may be different depending on the speed of the discharge process. The discharges for the lower part of the transfer curve are very slow to develop; thus, the time dealy of the Penning effect would be less important. For this region, then, the value of α would be large. By similar reasoning, the effective α for the upper transfer curve should be smaller since the discharge would be nearly complete before the Penning effect would set in.

How this might affect the charge transfer curve can be explained by taking Figure 3.11 as an example of a transfer curve without the Penning effect. Addition of the Penning effect will not change the upper region of the curve. It will, however, cause the lower portion of the curve to move to the left. This will cause a reduction of the memory effect initiated by having the non-square wave sustainer. Thus, in general, one might expect the Penning effect to reduce the memory margin.

To summarize, the results of memory obtained by Lay et al. will require further analysis to determine the exact nature of the transfer curve. Having a non-square wave sustainer adds to the memory effect, but having the

sustainer return to zero probably causes the effect to not be as strong as it could be. The effects of back diffusion will probably increase memory, whereas the Penning effect will probably reduce memory margins.

3.5 Experimental Results

No experiments were performed in this study to confirm the accuracy of the charge transfer curve theories presented in this chapter. However, there are a number of results achieved by other workers that are explained by these theories.

A value that nearly all researchers pay attention to is the firing voltage. This value is determined by what is happening in the lower regions of the transfer curve where little or no field distortion exists. Coleman [26], and Schermerhorn [27] have noticed that the firing voltage with a pure square wave sustainer is 10 to 20 volts lower than that observed with a non-square wave sustainer like that in Figure 3.8. This same trend is predicted by the transfer curve presented in Figure 3.12. Schermerhorn's results indicate that minimum sustain voltage is almost the same for both waveforms, and therefore, the non-square wave gives superior memory margin. These results, then, are in complete harmony with the theory.

While experimenting with the properties of shifting operations in plasma panels, Jones [28,29] took data using a return to zero sustainer similar to Figure 3.30. He found that the firing voltage increased as the sustain pulse width was shortened. For short pulse widths, the minimum sustain voltage was also increased. He also found that the shifting operation, or the ability of one cell to cause an adjacent cell to fire, was enhanced with high sustain voltages and short pulse widths.

This behavior can be clearly understood in terms of the present theory. It seems reasonable to expect that shorter sustain pulses should increase the firing voltage. As discussed above, the firing voltage for this type of sustainer is determined by the condition that a significant amount of wall charge be transferred to significantly change the cell voltage on the next discharge. The shorter the growth period, or sustain pulse width, the greater the growth rate must be to attain that same wall charge value. The higher growth rate implies a higher voltage pulse. As shown in Figure 3.19, the current can grow many orders of magnitude during a single short sustain pulse, with the cell remaining in the off state because insufficient wall charge has been transferred.

The shift technique relies on the fact that particles from one discharging cell can move to a neighboring cell and lower its firing voltage enough to turn it on. If the discharge calculations model the neighboring cell, the particle from the pilot cell can be modeled as an increase in the quantity j_o. It is clear that for the square wave case, the quantity j_o is going to have little or no difference on the firing voltage. As discussed above, the firing voltage is the $\mu = 1$ voltage, which is not affected by j_o. As the sustain pulse width is shortened and the firing voltage increases the current growth per pulse increases. The exponential growth all starts from the value of j_o. Thus, a doubling of j_o will also double the wall charge transfer for that sustain pulse. When the current growth is very large, the value of j_o can be very small and still be able to cause sufficient wall charge transfer to turn on the cell. In Figure 3.19, the value of j_o was 4×10^{-9} A/cm^2, which is more than 8 orders of magnitude smaller than the

peak discharge current of an on discharge. Although the current growth is large for this case, it is still insufficient to turn the cell on. However, when j_o was doubled, sufficient wall charge was transferred and the following discharge sequence turned the cell on, as seen in Figure 3.20. Thus, a shifting cell should become more sensitive to the stray particle of other cells as the sustain voltage pulses become large and narrow.

In terms of charge transfer curves, the shortening of the sustain pulse width has the effect of causing the lower portion to move further to the right as in Figure 3.11. The shorter the width, the further to the right and thus the higher the firing voltage. The increase in j_o causes the bottom portion to move back to the left.

One lesson that should be apparent from the above discussion is that the firing voltage of a cell depends on the waveform and on the states of other cells in the panel. Usually, when an experimenter quotes a firing voltage, the above determining conditions are not specified. To reduce this ambiguity it is suggested that all measurements of firing voltage be made with a pure square wave sustain generator. In this way, the effects of neighboring cells on the firing voltage will be eliminated. The resulting firing voltage will also be the $\mu = 1$ voltage, which is of fundamental significance to the device being studied.

One last experimental confirmation is found in some previously unpresented measurements by Weikart [30]. He noticed that in a very dark room, the eye could observe a very small amount of light coming from off cells with a sustainer applied. A large number of on cells were in the near vicinity, so at first he considered the light from the off cells to be

scattered light from the on cells. However, upon examining these off cells with a microscope, the major portion of light was seen to be from a very weak discharge in the off cells. When the sustainer was removed from the off cells only, this light went away. Figure 3.31 shows the sustain waveform and output from a large number of off cells. The initial short light pulse is due to scattered light from the neighboring on cells. However, the exponentially increasing light, that lasts the width of the sustain pulse, is from the off cells. This looks very similar to the situation seen in Figure 3.18, where the peak sustain voltage pulse was about 17 volts greater than the $\mu = 1$ voltage. For convenience, the linear plot of the data shown in Figure 3.18 is shown in Figure 3.32. The data shown in Figure 3.31 was taken with the sustain pulses 26 volts above the firing voltage obtained with a pure square wave.

A very interesting fact of the off cell discharges was that the discharges got weaker as the off cells got further away from the on cells. This would correspond to a decrease in j_o, which should be expected as a cell gets further from the source.

Thus, this is an excellent confirmation of the theoretical results that predict that the lower region of the charge transfer curve should move to the right, as seen in Figure 3.12, with application of a non-square wave sustain waveform.

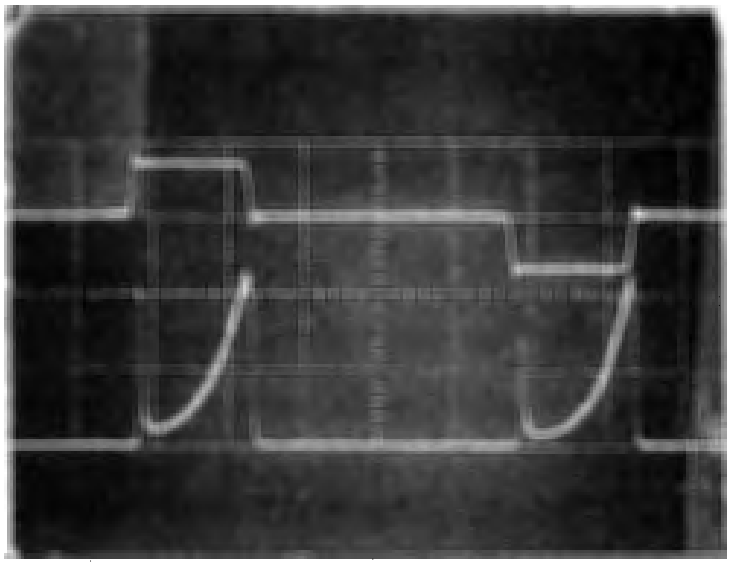

Figure 3.31. Sustain voltage and light output for plasma cells in the off state. The vertical scale is 200 V per division and the horizontal is 2 μs per division. The light output is the lower trace.

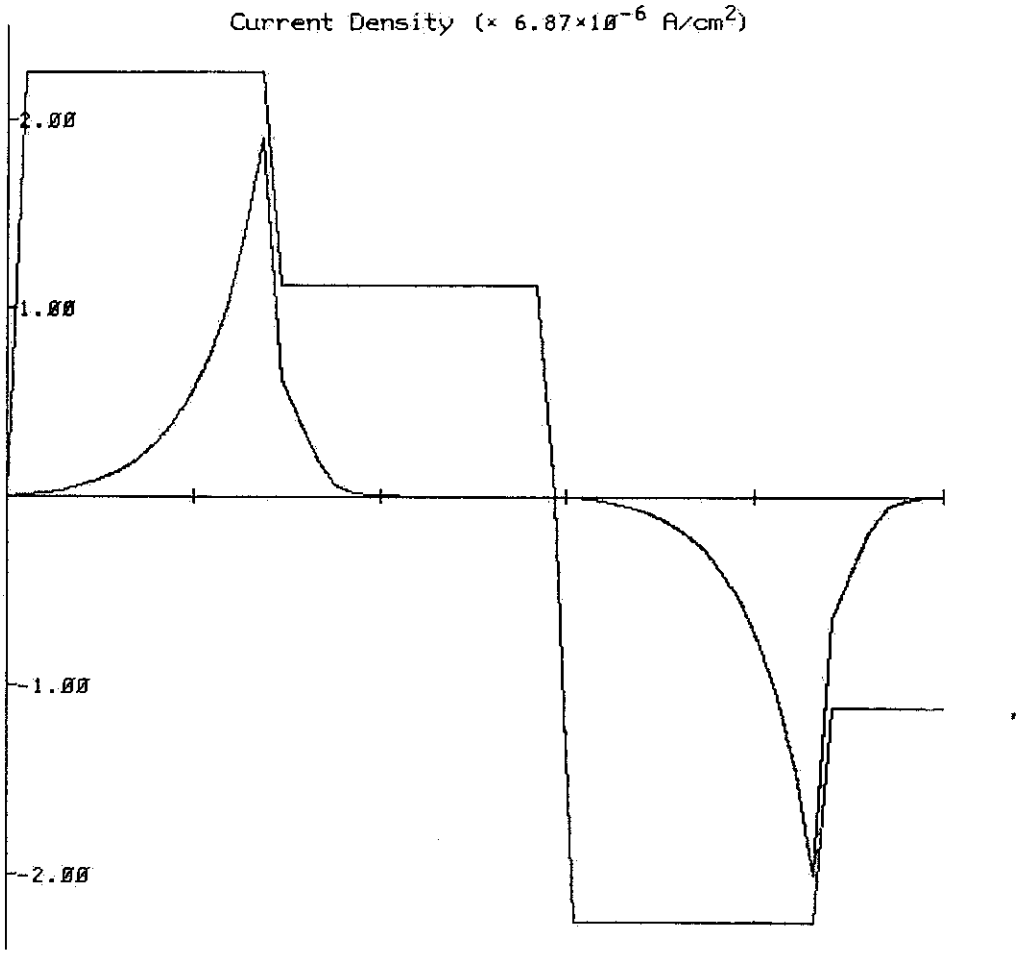

Figure 3.32. Calculated discharge current for a cell in off state. This is for the same data as shown in Figure 3.18. The applied sustain voltage is also plotted. The vertical scale factor is 6.87 x 10^{-6} A/cm^2. The peak sustain voltage is 250 volts.

CHAPTER 4

PLASMA DENSITY MEASUREMENTS USING RF AND MICROWAVE TECHNIQUES

4.1 Introduction

Chapters 2 and 3 of this thesis have been devoted to some theoretical aspects of the discharge dynamics. The remainder will be devoted to experimental measurements.

Most previous experimenters have been able to measure only 2 physical parameters of the plasma display panel: discharge current and light output. Although much information about the operation of the device can be derived from these parameters, a great amount of information is lost due to the fact that light and current are dependent on a number of other variables that are a function of both space and time.

Physical quantities that one would like to measure are shown in Table 4.1. Of these variables, probably the most important to the operation of the discharge dynamics of this device is the electron density. For this reason, a considerable amount of effort was placed into measuring this quantity both as a function of space and time. This and the next two chapters are devoted to that end.

4.2 RF Capacitance Measurements

The data shown in Figure 2.6 shows that in the plasma region away from the cathode, the plasma density is typically 10^{-6} C/cm^3, or about 10^{13} cm^{-3}. A plasma of this density has a plasma frequency of about 28 GHz. This means that for frequencies considerably below 28 GHz, the plasma will look like a near infinite dielectric constant material. Since the computer

TABLE 4.1

Measurable Physical Variables

Electron Density
Ion Density
Neutral Atom Density
Metastable Atom Density
Electron Temperature
Ion Temperature
Neutral Atom Temperature
Electric Fields
Glass Surface Effects

calculations predicted that the major part of the cell discharge gap would be filled with plasma and that the plasma would remain in the gap for a long time, it seemed reasonable to expect that the capacitance of the cell would change by large factors. Once this fact was realized, it took less than an hour of lab work to set up an experiment that presented the first experimental confirmation of the existence of plasma in the plasma display panel.

Figure 4.1 shows how the growth and decay of the plasma should affect the cell capacitance. Before the cell fires, no plasma exists and the cell has its neutral value C_o. At the time of the discharge, t_d, the cell fills with plasma and the capacitance increases abruptly. The peak value, C_p, is determined by how much of the gap is filled with plasma. As the plasma decays, in the manner shown in Figure 2.9, the capacitance slowly decreases until all the plasma in the gap has dissipated at time t_e.

It is important to note that these capacitance measurements give almost no information about the density of the plasma. Since for experimental reasons the capacitance measurements described here are done at frequencies at or below 200 MHz, the plasma would have to have a density below 10^9 cm^{-3} before it would act like anything other than a very large dielectric constant. At these densities, even a cold plasma's Debeye length becomes comparable to the gap spacing, making it impossible for a true plasma of density 10^9 cm^{-3} to exist in a plasma panel. Thus, the only information that can be obtained from capacitance measurements is the spatial extent of the plasma; and this information is limited to simply knowing how much of the gap is filled with plasma. Capacitance will not tell where in the gap the plasma is. The positioning of the plasma near the anode in Figure 4.1 was done based on the

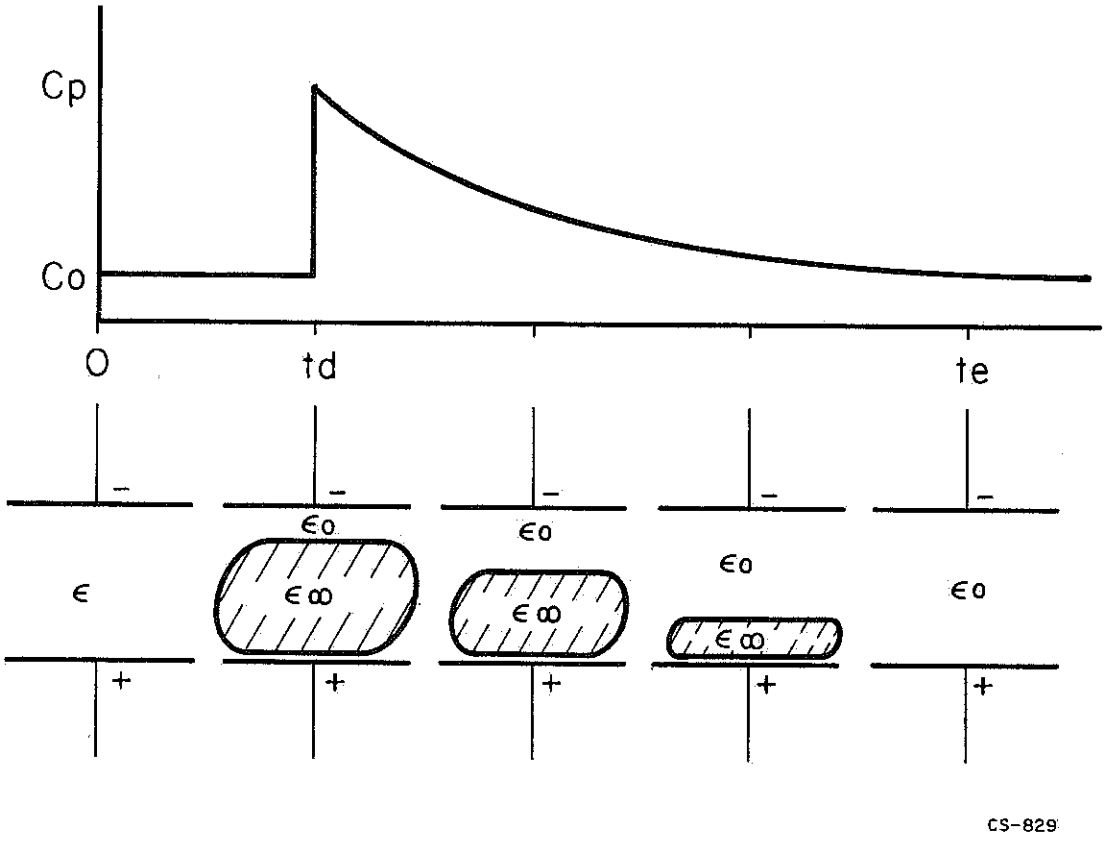

Figure 4.1. Variation of plasma cell capacitance due to the growth and decay of the plasma.

computer calculations. The most important information derived from the capacitance is about the existence of the plasma.

4.2.1 Resonance Technique

Although the computer calculations predict an increase in capacitance by at least a factor of 5, such large changes will not be measurable at a typical plasma panel's electrodes. The electrode in a panel has many stray capacitances that are much larger than the cell capacitance. Thus, even with all of the cells in a large panel discharging, the total capacitance may only change a few percent. A very simple way to measure this small capacitance change is shown in Figure 4.2. With this technique, the panel capacitance is made to resonate with a suitable inductor. Small changes in panel capacitance will cause changes in the resonant frequency of this LC combination. These changes will vary the coupling between the rf oscillator coil and the oscilloscope coil, which are loosely coupled to the resonating inductor. The sustain voltage is introduced, as shown, across a capacitance, C_b, which is very large compared to the panel capacitance. Thus, the sustainer does not strongly affect the operation of the resonant circuit. The value of the inductor is made small so that the rising of the sustain pulse does not cause too much ringing. The RF oscillator is adjusted to the resonance of the circuit which is usually between 10 and 100 MHz. The higher the resonant frequency, the less sustainer induced ringing becomes a problem. Of course, at too high of a resonant frequency, other resonant effects set in due to the inductance of the panel lines.

Figure 4.3 shows the output of the oscilloscope when the capacitance of a number of cells in an Owens-Illinois, 128 line, 33 line per inch plasma

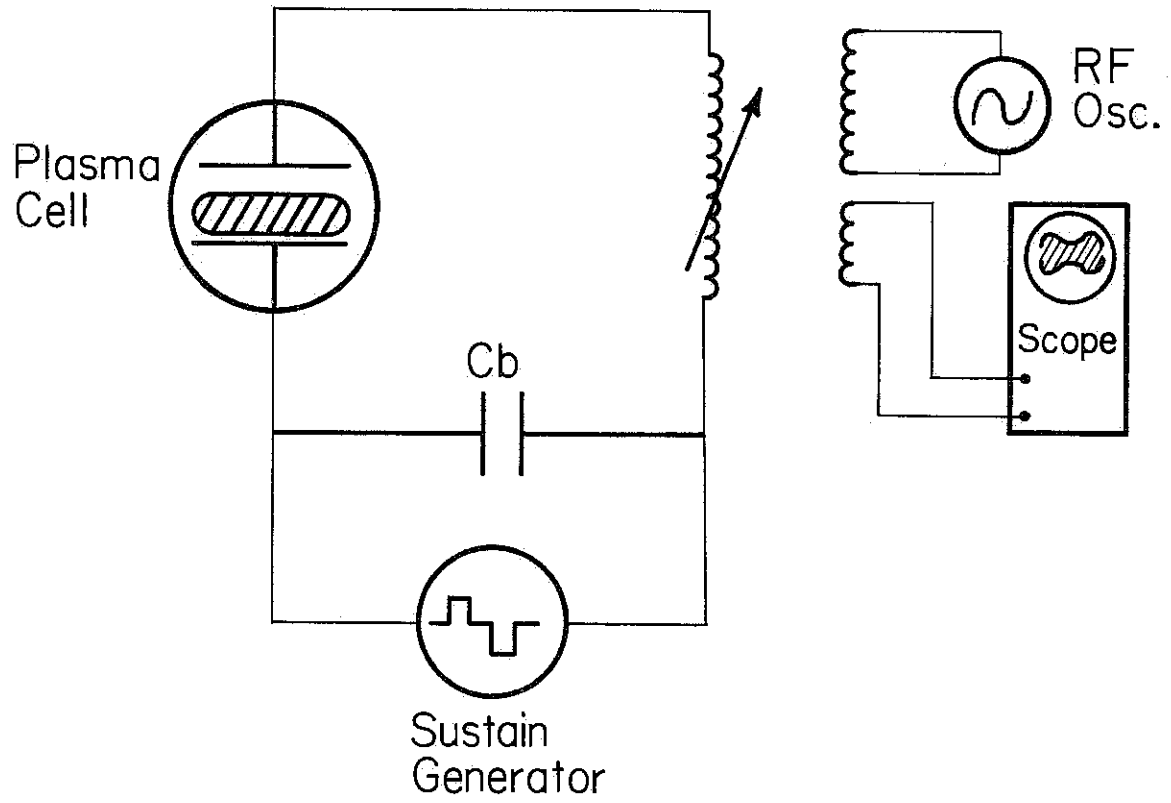

Figure 4.2. Resonance technique for measuring the variation in plasma cell capacitance.

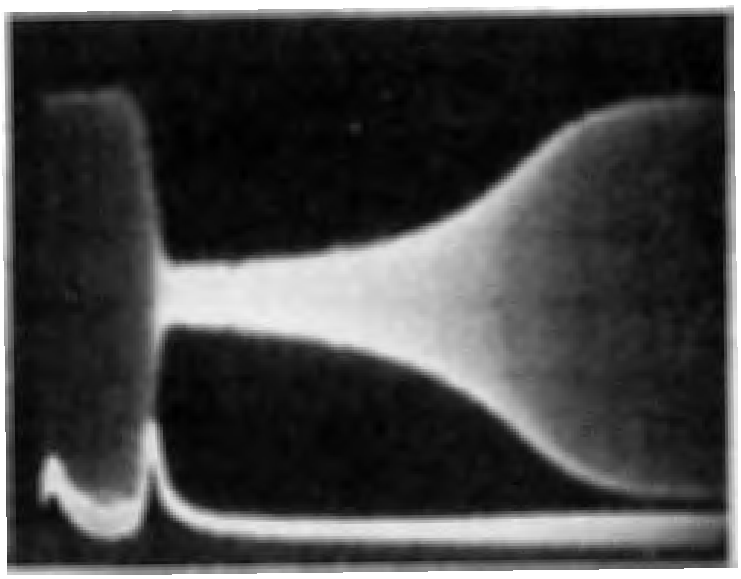

Figure 4.3. RF capacitance envelope and discharge current for a number of cells in a standard plasma panel. The RF frequency was 19 MHz. The discharge current scale is 40 ma/division. The horizontal scale is 2 μs per division.

panel was measured. Also shown is the discharge current pulse. In this figure, the oscillator was tuned to around 19 MHz. The output waveform is strongly dependent on the frequency of the oscillator. Figure 4.3 shows the oscillator tuned to give maximum coupling with the neutral capacitance, C_o. The capacitance increase, due to the discharge, caused a great reduction in coupling. As the plasma dissipates, the capacitance decreases and the coupling increases. Figure 4.4 shows the same measurement with a slightly different oscillator frequency. In this case the neutral capacitance, C_o, causes only intermediate coupling. As the capacitance increases due to the discharge, the coupling is further reduced. As the capacitance slowly decreases, it passes through a value where the coupling is maximized. This peak in coupling will move one way or another as the oscillator frequency is changed. Thus, the panel has all of the characteristics of a time-varying capacitance.

The data from the above two figures shows that the capacitance is changing for 15 μs after the discharge. This was taken in a standard plasma panel having a neon-argon gas mixture. Since most panels operate at a sustain frequency of 50 KHz, the discharges occur every 10 μs. Thus, it is very possible that the plasma from the previous discharge is an important initial condition for every discharge.

This technique can be modified to operate at higher frequencies if the inductance of the panel electrodes is used in place of the resonating inductor of Figure 4.2. The electrodes of most panels have a number of resonances in the 100-200 MHz range. A grid dip meter can be used to couple energy into the electrodes. A simple transformer made of a few turns of wire

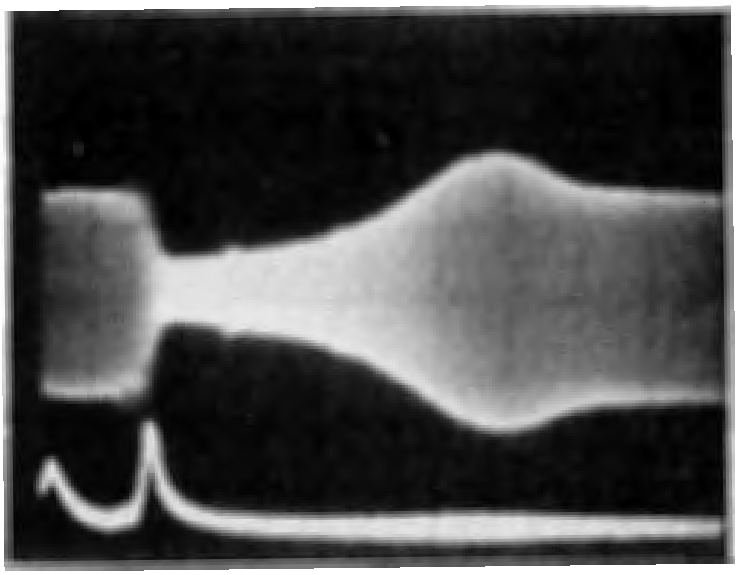

Figure 4.4. RF capacitance envelope for the conditions of Figure 4.3, except with a slightly different RF oscillator frequency.

can be used to couple energy to the oscilloscope. The primary is usually placed in series with the panel. A quick tune through the frequency range will usually find a resonance that will give a strong signal similar to those seen in Figures 4.3 and 4.4. This is a particularly useful technique because it is so easy to set up. It is no harder than measuring the discharge current or light output.

The above techniques are very useful for measuring the small capacitance changes in panels. However, they offer certain disadvantages when one tries to make a quantitative measurement of a plasma cell capacitance. The output of the resonant technique is determined by the oscillator frequency, and the circuit Q and resonant frequency. Techniques exist for measuring these quantities; thus, one could determine the quantitative capacitance variation in a plasma cell. However, this technique is messy and subject to error. A second disadvantage is that the ringing due to the rise of the sustainer is always somewhat of a problem in any resonant technique. With care, it can be reduced, but it is never eliminated, and usually always obscures the capacitance variation near the discharge peak.

4.2.2 Stub Technique

An alternate technique was used that did not involve a resonant circuit. It is basically a voltage divider technique that places the cell capacitance in series with the capacitance of the oscilloscope probe. The circuit is shown in Figure 4.5. Since the cell capacitance and the scope probe capacitance are on the order of 10 pf, it is very important to make all other impedances connecting to the cell very high. On the other hand,

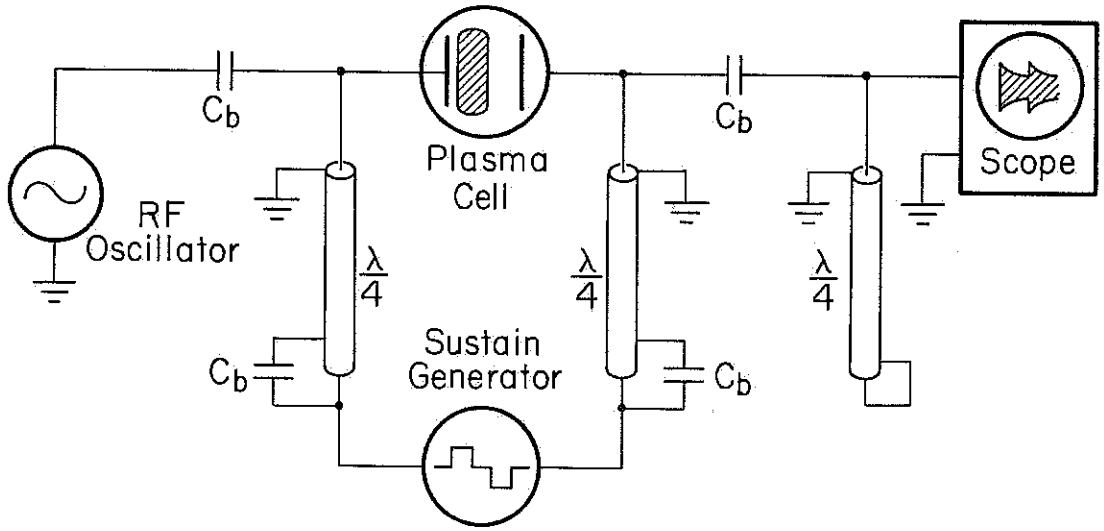

Figure 4.5. Circuit diagram of quarter wave stub technique for measuring the cell capacitance variation.

for the cell to operate properly, the sustainer must connect to the cell through a low impedance path. This problem is solved by using quarter wave stubs cut at the RF measuring frequency. A third problem is the fact that without an appropriate filter, the scope probe would see the very large sustain voltage on top of the small RF signal. A high impedance at the RF frequency and a low impedance at the sustain frequency was obtained with the third, quarter wave stub across the oscilloscope probe. The capacitors C_b are 200 pf and act as a low impedance at the RF frequency. The stubs connecting to the sustain generator were cut slightly longer than quarter wave since the capacitors C_b do not act as a perfect short. The extra length compensates for this and makes the stub impedance at the cell much higher than the cell capacitance.

Typical results are found in Figure 4.6, showing both the sustain waveform and the RF envelope. The height of the envelope is related to the cell capacitance by the voltage divider relationship with the oscilloscope probe capacitance, which is 12 pf for this data. To eliminate the stray capacitance problem a very large area plasma cell was constructed. The two electrodes were the shape of a disc, 1 cm in diameter. Aside from the very large electrode area, the remaining dimensions of the cell were typical. The glass dielectric thickness, ℓ, was about 25 μm, and the gap spacing, d, was about 200 μm. General construction techniques for experimental plasma cells are presented in section 6.3. The neutral capacitance, C_o, of this cell was 7 pf. With such a large cell capacitance, the effect of additional stray capacitances was minimized.

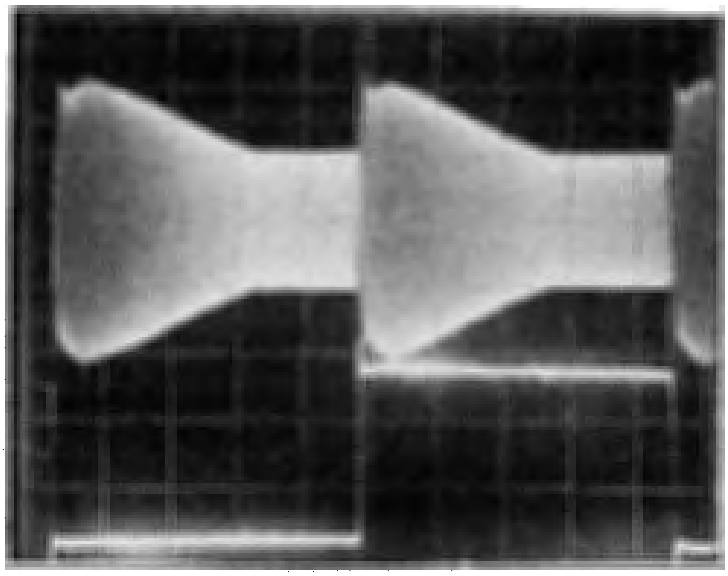

Figure 4.6. Capacitance envelope and sustain voltage waveform for large area plasma cell measured using the stub technique. The RF frequency was 56 MHz. The horizontal scale is 20 μs per division. The cell was filled with 250 torr Ne and 0.25 torr Xe.

The data shown in Figure 4.6 uses this large area cell with a gas mixture of 250 torr Ne plus 0.25 torr Xe. From this data it is seen that the plasma remains in the cell for at least 60 μs after the discharge. This is typical of all data taken with Ne + 0.1% Xe. The longest time observed for plasma decay in such mixtures was 100 μs. Different gas mixtures have considerably different plasma decay times. This will be discussed later in this chapter.

From data such as seen in Figure 4.6, one can easily figure out the actual capacitance of plasma cell by means of the voltage divider relationship. Referring to Figure 4.1, the value of C_o was 7 pf, and the value of C_p is measured at about 50 pf. Thus, the change in capacitance is very large. From these values one can estimate that the plasma fills about 6/7 of the discharge gap shortly after the peak of the discharge activity. This is consistent with the computer calculations as seen in Figure 2.6.

4.3 Induced Plasma Decay Phenomena

A number of interesting facts were observed in regard to the decay of the plasma. First, if the RF oscillator voltage is too high, it will cause the plasma to decay faster. Although the RMS RF voltage across the cell was always below one volt for all measurements, on some occasions even 0.1 volts RMS would cause the capacitance envelope to decay a little more rapidly. The physical mechanism for this RF dependent decay is not clear at this point.

A second, more interesting plasma decay phenomena occurs when the sustain voltage changes across the cell. Figure 4.7 shows the RF envelope and sustain waveform, showing typical behavior of the capacitance when the

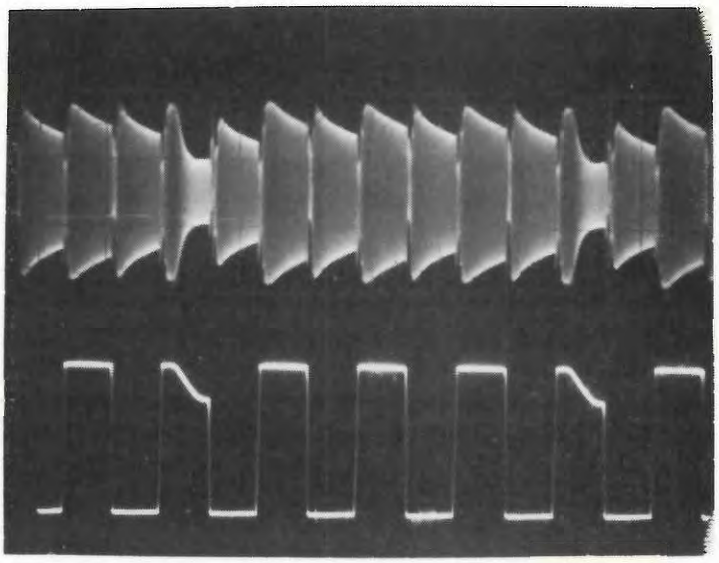

Figure 4.7. Capacitance envelope and sustain voltage waveform showing the decrease in capacitance due to a slow droop of the sustain voltage. The voltage scale is 200 V per division. The horizontal scale is 20 μs per division.

voltage across the cell is changed. In this case, after the sustainer had remained high for 5 μs, it was allowed to slowly droop to an intermediate value. This causes the plasma to be completely swept out of the volume, and the cell returns to capacitance C_o. In this case, the sweep-out process is slow and takes about 5 μs. However, the speed of this process depends strongly on the rate of voltage change across the cell. Figure 4.8 shows the same type of data taken with a non-square wave sustainer which is typical of that used in many plasma display systems. It is clearly seen that the plasma is swept out as soon as the sustainer falls. Thus the plasma exists, on the average, for only half of the complete sustain cycle.

Although the data presented above is for a falling sustain voltage, similar results occur when short pulses are added to the sustain waveform. Most pulses longer than 1 μs will completely sweep out the plasma. In general, a pulse of at least 50 volts is required. Shorter or smaller amplitude pulses will usually only partially reduce the capacitance. There does not seem to be a great deal of difference between positive going pulses or negative going pulses. Both can sweep out the plasma. Of course there is a limit to how high a positive pulse can go before it causes a discharge that creates additional plasma. None of the items mentioned in this paragraph should be interpreted as strict rules, but more as what is observed in many cases. Obviously, a much more careful study of the cell capacitance behavior as a function of the sustain waveform is needed.

The fact that the plasma can be swept out by an electric field presents an interesting theoretical problem. An important property of plasmas is that they shield out the effects of all electric fields applied below the

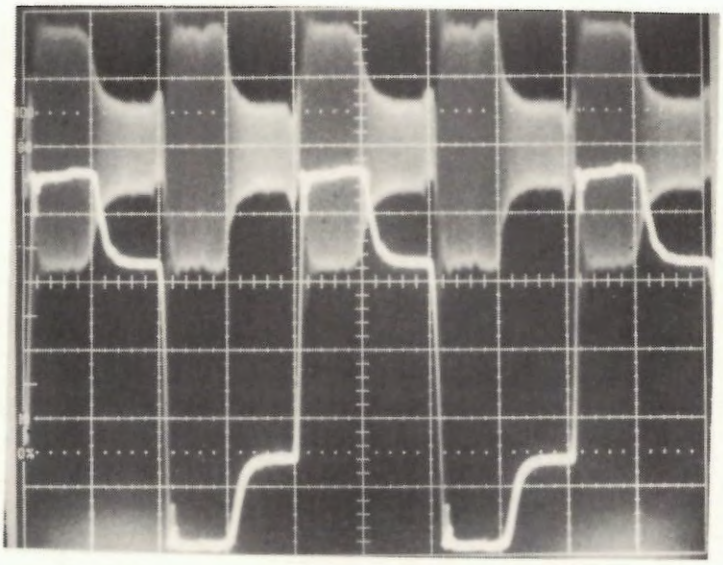

Figure 4.8. Capacitance envelope and sustain waveform showing that a non-square wave sustain waveform will sweep out the plasma during the voltage fall. The RF frequency is 56 MHz. The voltage scale is 50 volts per division, the horizontal scale is 5 μs per division.

plasma frequency. The fields used in the above experiments to sweep out the plasma have frequencies many orders of magnitude lower than the plasma frequency for this case. How then can a plasma be destroyed by such a low frequency?

The answer to this question obviously involves some very complex plasma dynamics. There is, however, a very simple explanation. If one considers the plasma as a material with an infinite dielectric constant, when the field across the plasma changes, the charges in the plasma will all move so as to cancel out the field. There is, however, only a finite amount of charge in the plasma. If, in order to cancel out the new applied field, the plasma would have to move more charge than it has, then the plasma could no longer exist.

A simple example will show that the above mentioned destruction mechanism is quite important. Assuming that the gap spacing is d = 100 μm and that the plasma fills 4/5 of the gap, the cell can be modeled as two series capacitors. The capacitor associated with the plasma has an infinite dielectric constant and thus infinite capacitance. Assuming an infinite parallel plane structure, the second capacitor, associated with the non-plasma region, will have a capacitance per unit area of $\frac{\epsilon_o}{g}$, where g, in this case, is 20 μm. If a 50 volt pulse is applied across the two series capacitors, the charge per unit area that will flow through both capacitors will be $\frac{Q}{A} = \frac{\epsilon_o V}{g} = 2.21 \times 10^{-9} C/cm^2$. Figure 2.6 shows that the peak plasma density is about 10^{-6} C/cm^3. For the data shown in Figure 4.8, the plasma has already decayed for 5 μs before the sustain voltage falls. Assuming that after 5 μs the plasma density is uniform at 10^{-7} C/cm^3 over the distance of 100 μm gives

a charge per unit area of 10^{-9} C/cm^2. Since this value is smaller than the charge that must flow through the capacitors, it is clear that the electrons will be swept away from the ions in trying to satisfy the displacement charge requirement of the 50 volt pulse. Once the electrons are swept away, the slower ions will soon drift to the wall.

The above very simple explanation neglects many important effects that would be included in a detailed analysis. This is really the problem of a plasma sheath. When a voltage is placed across a sheath, the sheath quickly adjusts to maintain the charge neutrality in the plasma. In this case, however, the sheath would have to grow to dimensions larger than the plasma itself in order to protect the plasma. Thus, the plasma decays. A more detailed analysis will have to wait for another study.

4.4 Microwave Measurements

The capacitance measurements have shown the existence of the plasma, but they give little information about its density. To do that one must go to higher frequencies so that the probing radiation is in the region of the plasma frequency. A very standard technique used by many is to measure the microwave transmission, reflection and absorption of the plasma [31]. This usually involves placing the plasma in a waveguide or perhaps placing the plasma between two horn antennas: one for the transmitter and one for the receiver. These techniques work well for very large plasmas which are used by most researchers in the area, but they are not practical with a discharge gap spacing of only 100 μm, as is found in the plasma panel.

4.4.1 Experimental Technique

After a considerable amount of thought and experimentation, it was found that one possible way to transmit the microwaves through a plasma cell was to make the plasma cell look like a strip transmission line. Figure 4.9 shows the geometry of such a plasma cell. One electrode of the plasma cell was made the ground plane and the other was made the strip conductor. The width of the strip was chosen to make the line impedance equal to 50 ohms. The spacing between the two electrodes was chosen to be close to the actual spacing used in plasma display panels. In this way, similar pressures could be used; thus the plasma densities should be the same. The glass dielectric thickness was also made similar to that of the plasma panel. The length of the plasma region of the strip line was 3 cm. The actual strip line continued for about 1 cm on each side of the plasma region. The plasma region was limited to 3 cm by the gas sealing material. The two ends of the strip line were connected to coax through special type N connectors that were constructed to minimize reflections in the transition from the connector to the strip line. The sustain generator was connected to the strip electrode by a very narrow serpentine electrode that was screen printed at the same time as the strip electrode. Because it was much narrower than the strip electrode, it had a much higher impedance than 50 Ω. Also, the serpentine pattern acted as an inductor at the microwave frequency. Thus, there seemed to be minimal effects on the microwave transmission due to the sustain generator connection.

The microwave energy was generated at about 10 GHz by a reflex klystron. The klystron was coupled through a wave guide, isolator, and

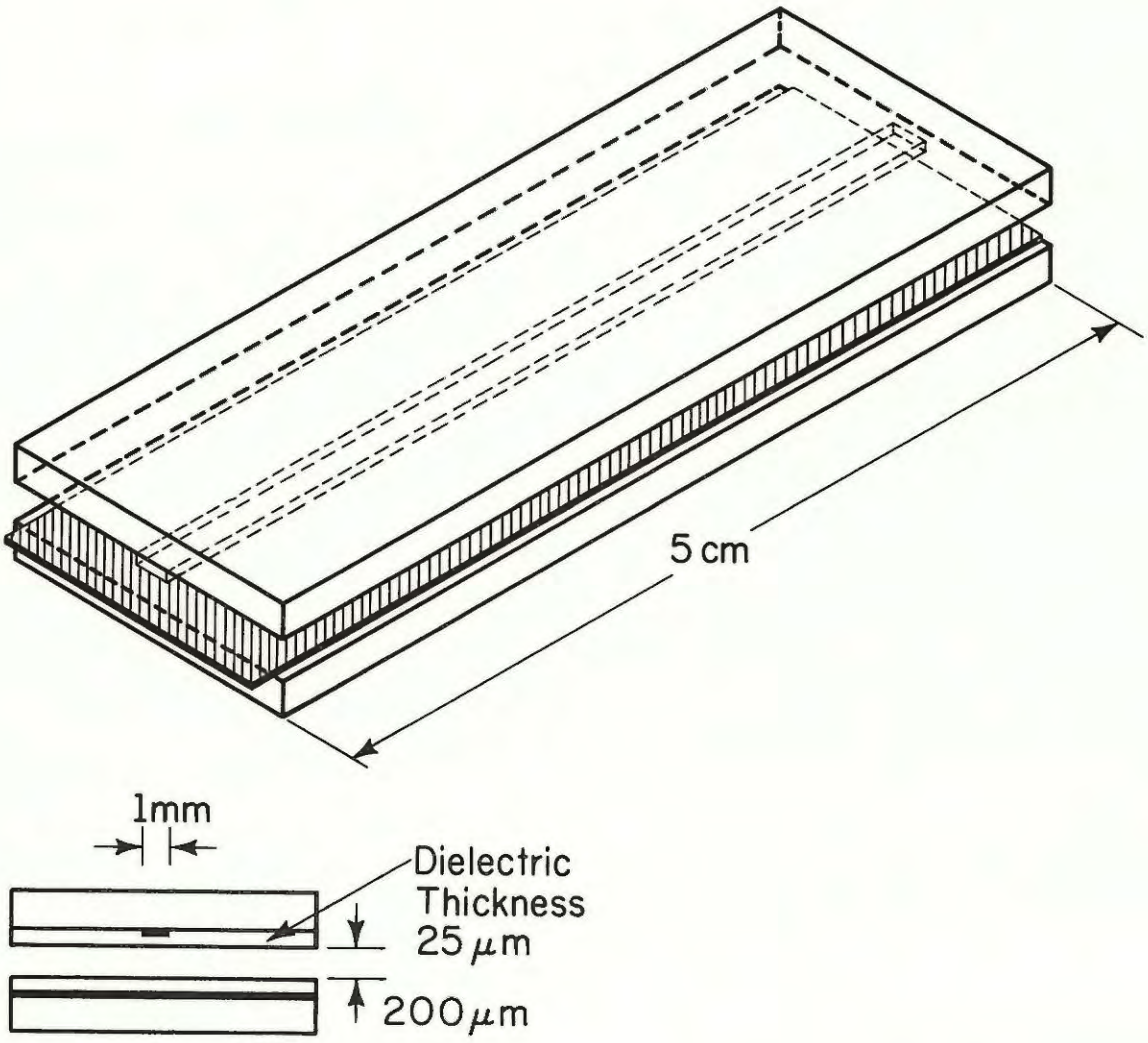

Figure 4.9. Geometry of strip line plasma cell used to measure microwave transmission.

attenuator to a length of RG-8 coax that connected to the strip line. It was important to use an E field coupler between the waveguide and coax, since the loop of the H field coupler would complete a DC connection between the two electrodes of the strip line thus shorting out the plasma cell and the sustain generator. The output end of the strip line was again connected with coax to a waveguide detection system. This was simply a waveguide isolator and a waveguide crystal detector. The current from the detector went to the scope to give an indication of the microwave transmission through the strip line.

The experimental setup was further refined so that capacitance measurements could be made simultaneously with the microwave measurements. The circuit seen in Figure 4.5 could not be used in this case since the ground plane end of the plasma cell was connected to a good ground through the coax, the waveguide, and eventually through to the klystron power supply. In the revised capacitance measuring scheme shown in Figure 4.10 the capacitors C_b are large, typically 200 pf; and the capacitor C_s is of comparable size to the plasma cell, which is typically 15 pf. At the RF frequency, the scope probe is in parallel with the plasma cell. All of the RF energy is coupled in through capacitor C_s. As the cell capacitance increases, then, the RF signal at the scope will decrease. The sustain generator is again isolated with a slightly longer than a quarter wave stub. The shorted stub across the probe is used to filter out the sustain voltage from the scope input. Since both the sustain generator and the plasma cell must be grounded by this technique, it was most convenient to make the sustain generator put out only positive going pulses. Thus these pulses were twice the amplitude of the

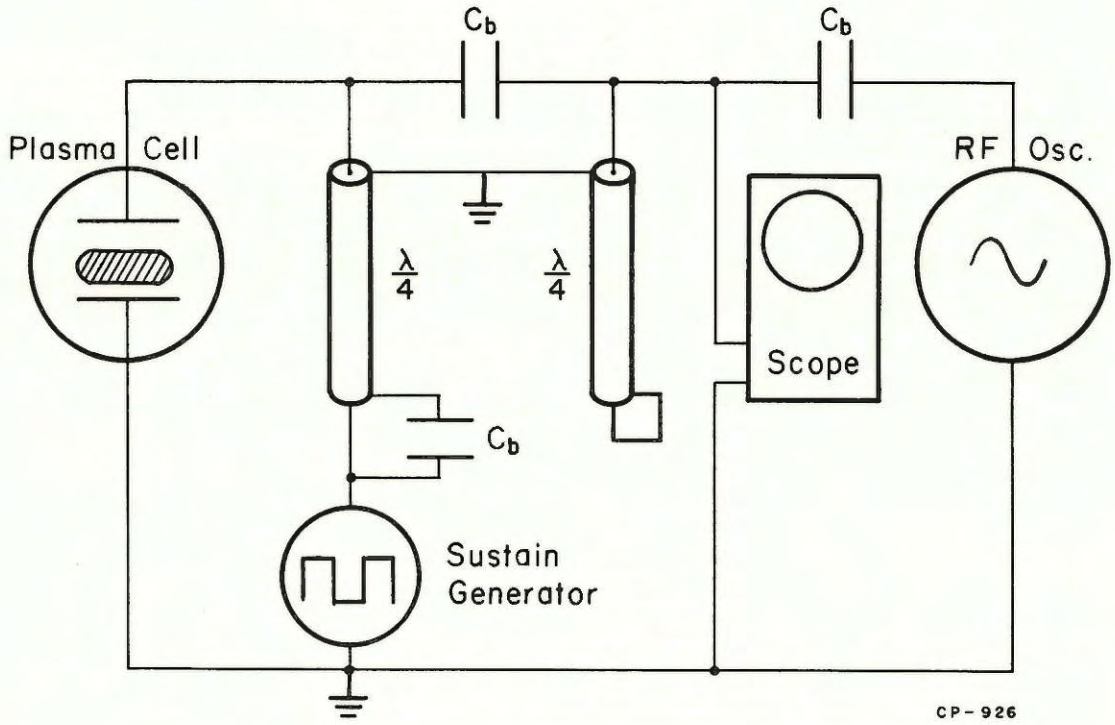

Figure 4.10. Capacitance measuring circuit used with the microwave transmission experiment.

normal pulses which go positive and negative. Since this is just a matter of ground reference, it did not affect the outcome of the measurements.

In the initial measurements, considerable difficulty was experienced in observing the capacitance variation due to the loading produced by the coaxial lines leading to the waveguide. This problem was easily solved by making each piece of coax a half wavelength long at the RF frequency. Since the waveguide ends of these lines are essentially open to the RF, the strip line end also acted as an open. Thus, the connection or disconnection of the microwave coax lines showed little effect on the capacitance measurements.

4.4.2 Experimental Results

Figure 4.11 shows typical data for the strip line cell filled with 250 torr Ne + 0.4 torr Ar. A pure square wave was used as a sustainer. It is clear that the microwave transmission goes to zero at the time of the discharge. After the plasma dissipates, it rises agin to 100%. The capacitance shows similar behavior, increasing at the discharge, then slowly decreasing to the neutral value. Figure 4.12 shows data for the same setup but with 250 torr Ne + 0.4 torr Xe. The plasma lasts much longer as seen in both the capacitance and the microwave measurements. A general feature of all data taken was that Ne + Xe plasmas lasted considerably longer than Ne + Ar plasmas of the same pressure and percentage of minority gas. This is as expected since the predominant ion in the late periods of the plasma decay is most likely to be the minority gas ion. Since the diffusion constant of Xe^+ is much smaller than Ar^+, one would expect the Xe^+ plasma to decay slower.

Another general observation was that the plasma would die off more quickly if the microwave power was at too high a level. Although no power

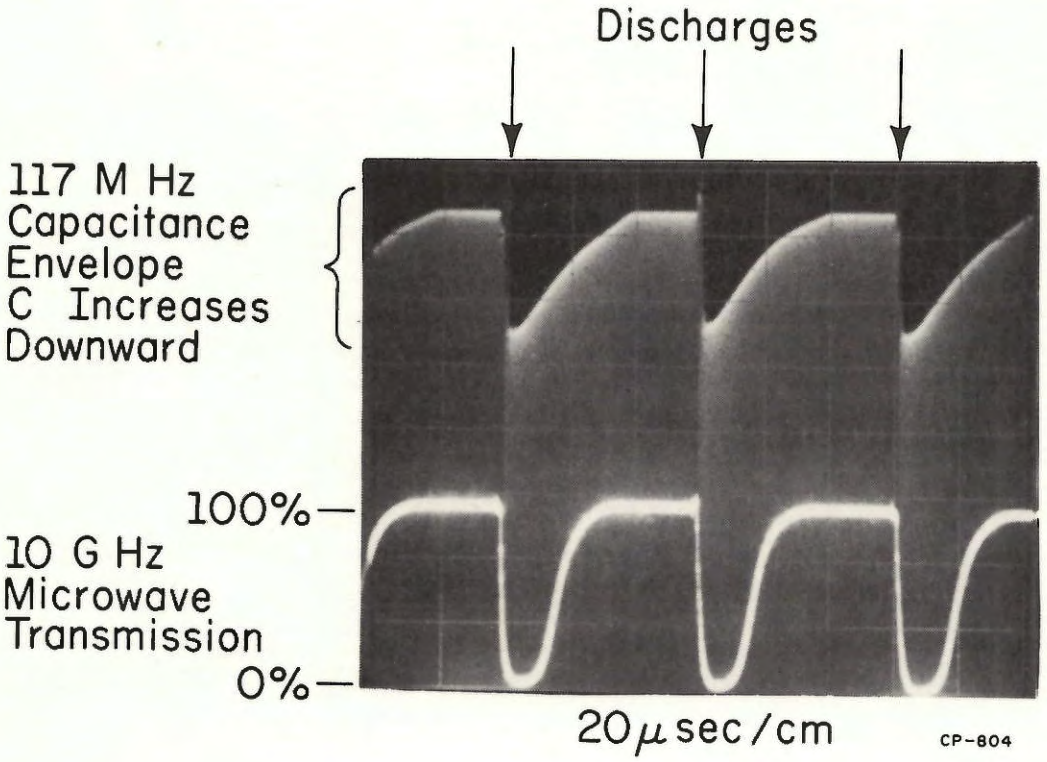

Figure 4.11. Microwave transmission data and capacitance variation for the strip line cell filled with 250 torr Ne and 0.4 torr Ar.

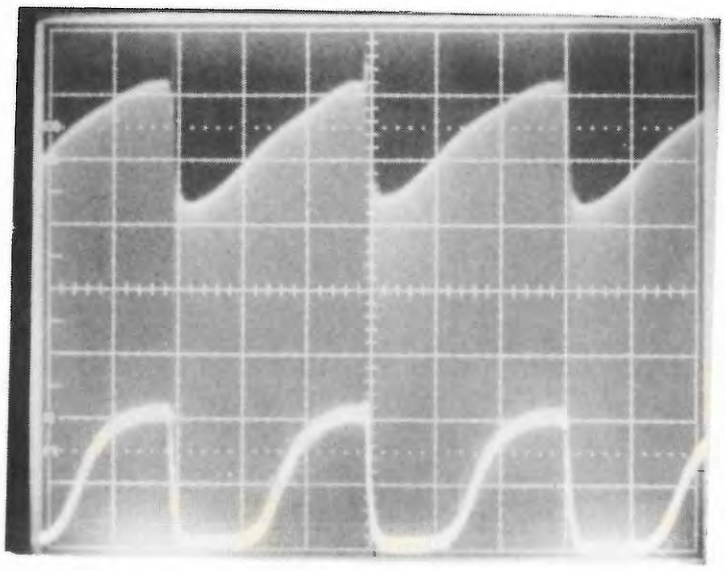

Figure 4.12. Microwave transmission data and capacitance variation for the strip line cell filled with 250 torr Ne and 0.4 torr Xe. The horizontal and vertical scale factors are the same as in Figure 4.11.

measurement was made, the maximum rated power output of the klystron was $\frac{1}{2}$ watt. The measurements shown in Figures 4.11 and 4.12 were made with the power attenuated to a level where the microwaves did not cause any increased plasma decay. As in the case of the RF enhanced plasma decay, the mechanisms involved are too complex for speculation here as to the causes.

The data in Figures 4.11 and 4.12 could be interpreted as meaning the following. When the microwave transmission is cut off, the plasma has a plasma frequency greater than 10 GHz. As the plasma decays, the plasma frequency also decreases so that when it is lower than 10 GHz, the transmission begins to increase. Even when the plasma frequency is considerably below 10 GHz, the transmission may still not be 100% since the plasma still acts as a material with a finite dielectric constant that will change the impedance of the strip line and cause reflections. A plasma frequency of 10 GHz corresponds to a plasma density of 1.24×10^{12} cm^{-3}. Thus, it seems reasonable to expect that the actual plasma density is above 10^{12} cm^{-3} for the early part of the discharge cycle.

The above analysis is really a bit too simple. A very important complicating factor arises upon consideration of electron collisions with neutral atoms and ions. The collision frequency is very high for the plasma panel because of the high gas pressures. Chen [32] shows that in neon the momentum transfer collision frequency between electrons and neutral atoms is about 10 GHz for a pressure of 250 torr and an electron temperature of $305^{o}K$. The electron-ion collision frequency depends on the ion density. Chen also shows that for $300^{o}K$ electrons in pure Ne at

250 torr, in a plasma of density 10^{13} cm^{-3}, the electron-ion collision frequency will be about 20 GHz. Similarly, a plasma density of 10^{12} cm^{-3} corresponds to a 2 GHz collision frequency.

The important frequency of interest here is the total of both the atomic collision frequency and the ionic collision frequency. From the numbers above, a minimum value is 10 GHz. In general this number will increase with electron temperature. The electrons in the plasma studied here certainly have a temperature much greater than $300^{o}K$ for a major part of the sustain cycle. Thus, it is very clear that the total collision frequency is much greater than the microwave measuring frequency.

The above fact complicates the interpretation of the data found in Figures 4.11 and 4.12. Much of the decrease in microwave transmission could be attributed to absorption in collision processes. Since neither the plasma frequency or the collision frequency are very well-known in this experiment, it is obvious that additional measurements and analysis are needed. It would be useful to conduct both transmission and absorption measurements at a number of different microwave frequencies in order to separate the effects of these two frequencies.

A further complicating factor is that the plasma does not fill the entire discharge gap. The capacitance measurements show that the spatial extent of the plasma is diminishing after the discharge. This must be properly accounted for in interpreting the microwave transmission. Again much further analysis is needed.

Although from the above discussion, one cannot confidently say anything about the plasma density from the microwave measurements, as in the capacitance measurements, one can get information about the dependence of the plasma on sustain voltage pulses. Figure 4.13 shows the sustain voltage and typical microwave transmission for a higher frequency sustain signal than used in Figures 4.11 and 4.12. In this case the sustainer falls before the plasma has decayed. Near the end of the sustain pulse, the transmission is increasing; but as the pulse falls, the transmission decreases and then increases to 100%. This is better seen in the expanded time scale of Figure 4.14. The transmission remains at 100% until the start of the next discharge about a half microsecond after the completion of the sustain pulse fall.

The reason for the small decrease in transmission is not clear and deserves further study since it should give clues as to the mechanisms involved in the plasma sweep out process. It is very clear that the fall of the sustain pulse did cause the sweep out of the plasma, and that the process was complete midway along the sustain transition. Thus, the microwave measurements are consistent with the results of the RF capacitance measurements. Figure 4.15 shows the transmission data for a return to zero sustain waveform. This data is similar to that shown in Figure 4.8 in that both show that the fall of the sustain pulse sweeps out the plasma.

4.5 Significance of the Existence of Plasma

Both the RF capacitance and the midrowave transmission measurements have clearly demonstrated the existence of the plasma predicted by the

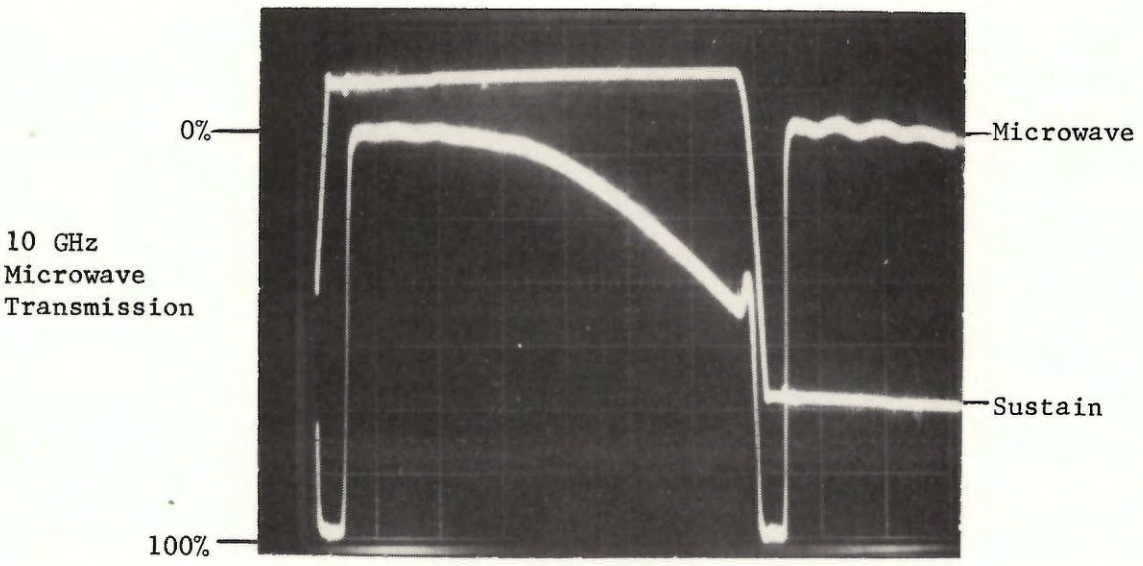

Figure 4.13. Microwave transmission data and sustain voltage waveform showing the effects of a falling sustain voltage. The horizontal scale is 2 μs/division.

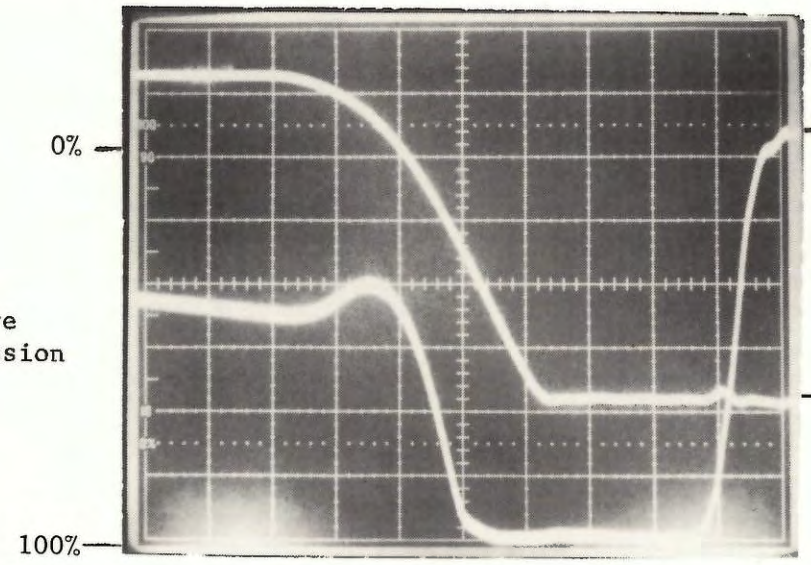

Figure 4.14. Microwave transmission data for the same conditions as in Figure 4.13. The horizontal scale is 200 ns/division.

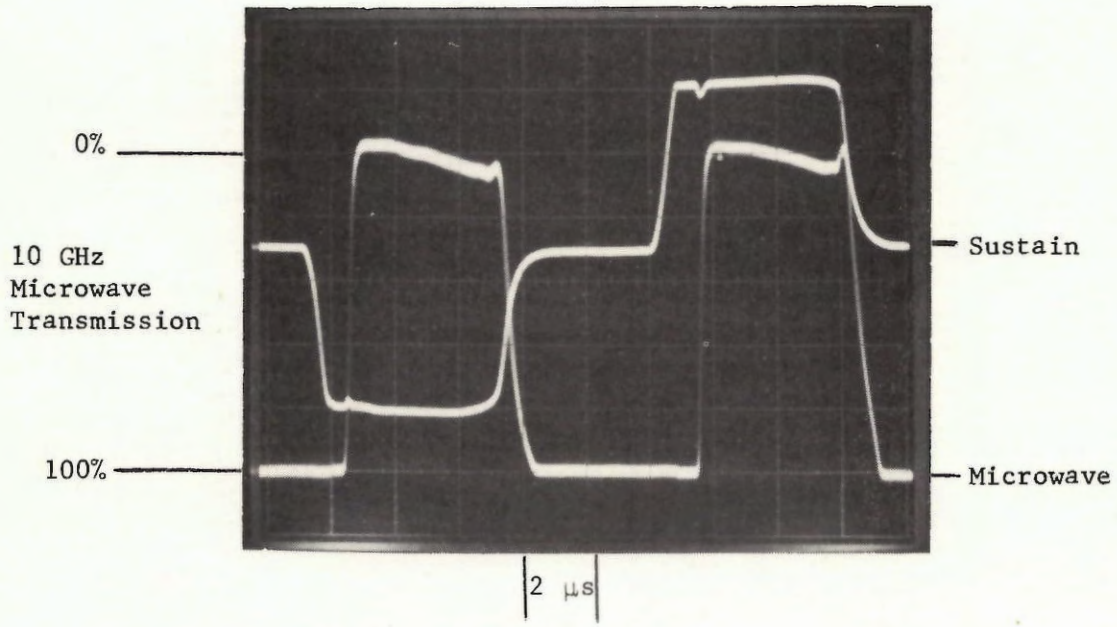

Figure 4.15. Microwave transmission data showing the plasma sweep out for the fall of the return to zero sustain waveform.

computer calculations. They have not verified the magnitude of the plasma density predicted; however, further work on the microwave measurements at various frequencies may be able to provide accurate densities. The plasma is clearly swept out of the volume by a significant change in the sustain voltage. The lifetime of the plasma can be as long as 100 μs and depends strongly on gas mixture. However, for most sustain frequencies and waveforms used in typical panels, the plasma is swept out by a changing sustain voltage. This section will discuss what these results imply to the characteristics of the plasma display panel.

The plasma densities predicted by the calculations show peak densities on the order of 10^{-6} C/cm^3. This represents a considerable amount of charge in the volume. Since it is desirable to maximize the amount of wall charge transfer for a given discharge intensity, the question arises as to how the volume charge can be deposited on the wall so as to increase the wall charge transfer. With the sustain waveforms presently used, the volume charge is swept out by the falling sustain pulse. For cells in the on state, the fall of the sustain pulse usually means a reversal in the field across the gas, since the field due to the wall charge does not change until a discharge occurs. This field reversal will cause the plasma that is being swept out of the volume to go to the walls in a manner that decreases the wall voltage. This effect is seen in the calculations of Figure 4.16. Thus, with the present way of operating the plasma panel, the volume charge actually decreases the total wall charge transfer. This effect is probably a major reason why sustain voltage pulses typically must be at least 5 μs

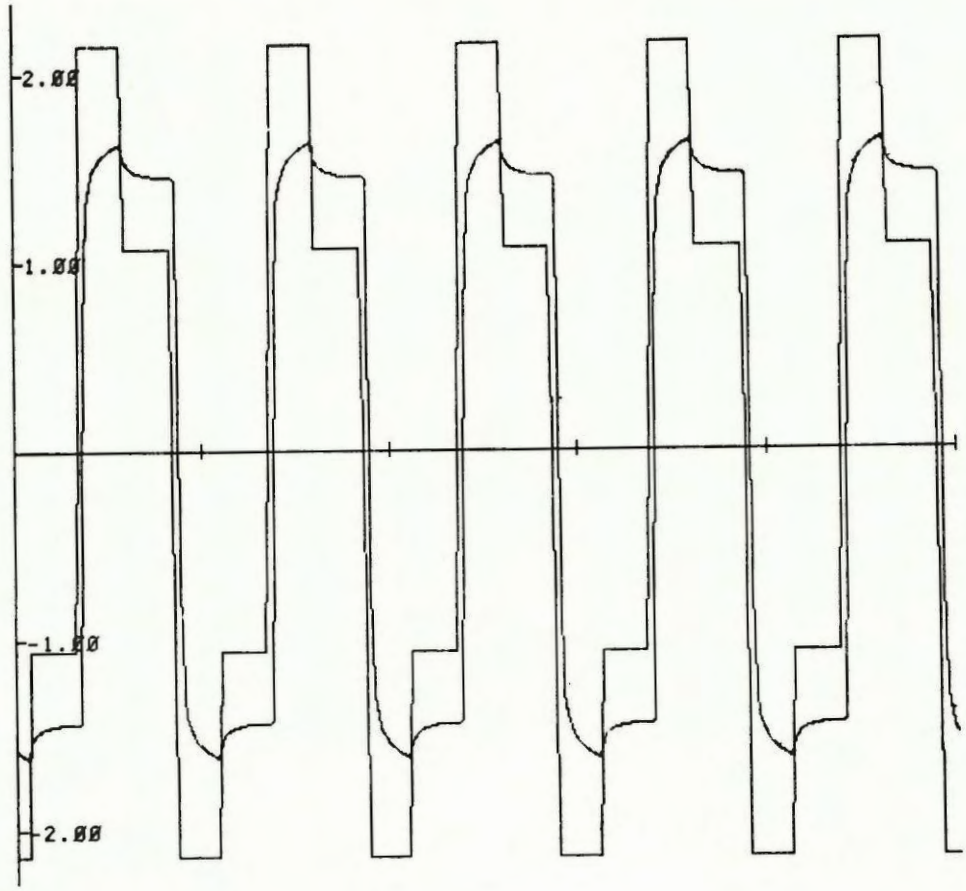

Figure 4.16. Sustain voltage and wall voltage for a stable discharge sequence showing the small change in wall voltage due to the fall in the sustain voltage.

long in order to achieve memory. For shorter pulses, the plasma is of such density that a very significant amount of charge is transferred during the fall of the sustainer. Thus, 5 μs must be spent for the plasma to be reduced in intensity.

Considerable improvement might therefore be obtained if the volume charge could be added to the wall charge. How this can be accomplished is not clear at this point. However, the experiments showed that the plasma is swept out for both positive and negative going sustain pulses. By the application of an appropriate positive going sustain pulse on top of the normal sustain pulse, one might be able to sweep out the plasma in a beneficial direction. Once the plasma is no longer in the volume, the sustainer can fall in the usual manner without penalty. The problem with this technique is that the positive pulse cannot be too high or it will act as a write pulse to the cells in the off state. Thus, some more experimental work is needed to find the appropriate waveform that will sweep out the plasma without causing the off cells to turn on. This work can now be done with the aid of the RF capacitance measurement techniques developed in this chapter.

The second area where the existence of the plasma is of concern is the computer interrogation of the information stored in the panel. Two techniques have been shown to be feasible. Circuits that sense the discharge current of an individual cell can be used for direct electrical readout [33]. Also, a photomultiplier can be used to sense the light output of an individually-addressed cell [34]. Both of these techniques suffer from noise that is associated with the existence of the plasma.

In the discharge current sensing scheme a sense amplifier on an X line detects the current from one cell that is discharged by a sustain pulse on a single Y line. If all the cells in that X line are in an on state, they will have discharged a short while before the sense operation. Existence of the plasma will cause a small amount of current to flow in all of these on cells as seen in Figure 2.12. Although this current is small, it can be very significant when all of the small currents from all cells in the X line are compared to the peak discharge current of the one cell to be sensed. Thus for unambiguous sensing, one must wait 15 μs after a sustain discharge before the cell to be sensed can be discharged. This is a disadvantage because it reduces the rate at which cells can be read. It should be possible to greatly reduce the long current tail of the on cells by simply placing an appropriate sweepout pulse that will remove the plasma before the read operation takes place. Thus, the 15 μs period could be considerably reduced and the read rate increased.

A very similar problem exists with the optical readout technique. If a large number of cells in the panel are in the on state, then their total afterglow can amount to significantly more light than will come from the one cell that is to be read. Assuming that this afterglow is produced by recombination mechanisms in the plasma, the appropriate sweep out pulse might reduce the afterglow light to a tolerable level.

CHAPTER 5

A VERY SENSITIVE LASER INTERFEROMETRY SYSTEM

5.1 Introduction

From the measurements of Chapter 4, it is clear that a long-lived plasma exists in the plasma display panel. However, little information was obtained about the density or the distribution of this plasma throughout the cell. It is clear that shorter wavelength radiation is needed to probe the area across the discharge gap. Thus, considerable effort was placed in measuring the properties of the plasma with optical wavelengths. Since the optical frequency is very much greater than the anticipated plasma frequency, the plasma will simply change the phase of the probing light beam. To measure this phase change, the plasma cell must be placed in a very sensitive interferometer.

The anticipated phase change imposed severe resolution requirements on the interferometry system so that a great deal of effort was placed just in developing suitable interferometry techniques. The end result was a very simple system capable of measuring optical phase changes smaller than 10^{-5} Å. Since this value is smaller than any other known to appear in the literature, this entire chapter is devoted to a discussion of this interferometry system. Chapter 6 presents the application of this system to the measurement of the plasma properties.

5.2 Resolution Requirements

The first question that needs answering is "does the electron density in a plasma panel have sufficient amplitude to be measurable by

interferometry techniques?" From Maxwell's equations one can easily show [35] that the phase change is

$$\Delta\varphi_e = - B\Delta n_e L\lambda \quad , \tag{5.1}$$

where $\Delta\varphi_e$ is the phase change in radians due to the change in electron density, Δn_e, L is the length of the plasma traversed, λ is the laser wavelength and $B = 2.817 \times 10^{-15}$ meters.

Figure 2.6 shows that the peak electron density should be in the range of

$$10^{12} < n_e < 10^{13} \text{ cm}^{-3} .$$

If we assume a very long plasma display cell of L = 1 cm and a typical laser wavelength of $\lambda = 6328$ Å, then from (5.1) and an electron density of 10^{12} cm^{-3} we get a phase shift of 1.78×10^{-5} radians or 0.018 angstroms. This is a very small phase change that looks very discouraging since it is generally considered that good interferometry technique can measure fringe shifts of only $\frac{\lambda}{100}$, [35]. The basic problem that limits the sensitivity of most interferometers is mechanical stability. The mechanical elements usually move many ansgtroms due to thermal expansion and sonic vibrations.

A number of factors created optimism in being able to measure the required small fringe shifts. The first was the discovery of a particular type of interferometer in which most mechanical motion was balanced out. Also, since the plasma display panel operates at high frequencies (50 kHz) relative to the acoustic vibrations, much of the remaining low frequency

acoustic noise can be filtered out. Also, averaging techniques are convenient to use at this frequency, thus greatly increasing the signal-to-noise ratio.

5.3 Details of Interferometry System

The basic interferometer arrangement used in this work is shown in Figure 5.1. It is a Jamin interferometer in which two optical flats are aluminized on their back sides to form mirrors. This interferometer is very stable since there are only two elements that can move to cause an unwanted phase change - the two flats. Translational motion of the flats in the y and z directions causes no change in optical path length for perfect optical flats. Translational motion in the x direction will change the length of both beams equally, allowing their relative phase to remain unchanged. The only motion that can cause a noise signal is a rotational motion about the z axis. Thus, this is an extremely stable interferometer. Most other interferometers, such as the Michelson, require a very stable mechanical mount to get the output fringes to remain stationary enough for the eye to recognize them. The Jamin interferometer meets this criteria when the flats are held with the human hand.

With the mechanical noise problem essentially solved, other noise sources become important. The light source becomes the main problem. Lasers are generally recognized as the only reasonable choice of light source for this problem. However, they are also fairly noisy devices. A 1% noise level seems good to a laser manufacturer, but for this problem it represents a signal equivalent to a $\lambda/200$ phase shift and is thus quite unacceptable. Fortunately, this noise can be canceled out by using a second detector and a

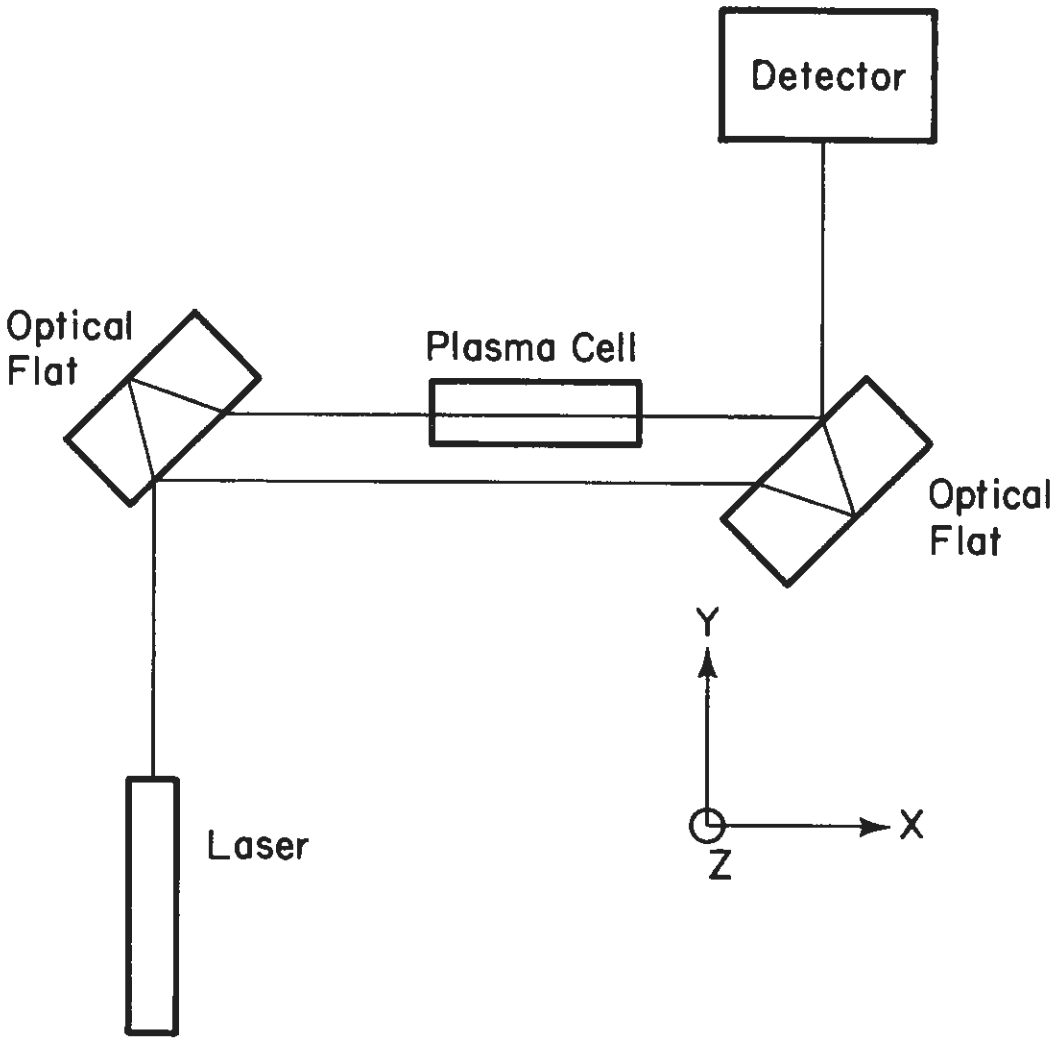

Figure 5.1. Jamin interferometer.

differential amplifier. The second detector can be placed at a number of places along the beam. For instance, in Figure 5.1 a beam splitter can be placed between the laser and the interferometer. The deflected beam from this beamsplitter goes to the second detector. The outputs of both detectors are fed to a differential amplifier. If the two detectors are sufficiently linear and properly frequency compensated, all of the excess laser noise can be canceled out to the level of the shot noise plus the detector noise.

The shot noise is not the shot noise traditionally associated with the leakage current of the detector, but rather the shot noise due to the current from the laser light. This noise current is given by the familiar formula

$$I_{sn} = \sqrt{2\Delta f I e} \tag{5.2}$$

where Δf is the bandwidth, I is the signal current and e is the electron charge. Since the signal we wish to measure clearly increases proportional to the laser light intensity, the signal-to-shot noise ratio increases as the square root of the laser intensity. Thus, it pays to use the highest power laser available. A high power laser also eases the electrical noise problem since the electrical noise, such as that caused by the high voltage sustain waveform, is not dependent on laser power. Thus, the signal to electrical noise ratio is proportional to the laser poser. With the power from even a 1 milliwatt laser, the noise generated in the detector (such as resistive noise) is so small compared to the signal shot noise that all other noise sources can be neglected.

Three different laser systems have been used with this interferometer. Initial experiments were made with an RCA 4 mw He Ne laser at 6328 Å. This worked very well and allowed a significant amount of data to be taken. The second system was a homemade He Ne laser simultaneously operating at 6328 Å and 1.15 μ. The power on both of these lines was probably under 1 mw. The measurements at the two wavelengths could be performed simultaneously which was desirable because of factors discussed in Chapter 6. Late in the course of these studies a Spectra Physics 166 Argon Ion laser, capable of oscillating at 9 different wavelengths with a total power of 4 watts, was obtained. Since it was the most powerful of the three, the argon ion laser was used to evaluate the performance of the interferometry technique. However, much initial experience was gained in using the 4 mw He Ne laser, and a few of the tricks learned are related below.

The first lesson learned was that silicon photodiodes are better suited for detectors than photomultipliers in this application. The obvious reason is that the photomultiplier is easily saturated by the bright laser light. But even if one takes precautions against saturation, the photodiode is still superior because of its greater quantum efficiency. This is true based on the assumption that the system is shot noise limited. The detector with the higher quantum efficiency will have a larger current flowing through its cathode and will thus have a larger signal-to-noise ratio. The advantage of the photomultiplier of being able to resolve individual photons is not important here because the large amplitude of the laser beam is capable of quickly charging the capacitance of any photodiode.

The high intensity of the signal from the Ar^+ laser caused great saturation difficulties for many of the photo detectors used. For many high performance PIN diodes, the nondepleted silicon acts as a series resistor in the kil-ohm range. This resistance will drop nearly all of the reverse bias voltage for currents in the tens of milliamps. To solve this problem, very large area photovoltaic detectors had to be used. The photovoltaic detectors are made of a lower resistivity silicon, making the series resistance much lower. These detectors were usually reversed biased to about 12 volts in order to reduce junction capacitance. Individual diodes had to be selected to insure that 12 volts did not exceed the reverse breakdown voltage. Most of the data shown here was taken with E. G. & G. PV 444A or PV 215 diodes.

A lesson learned empirically is that it is important for the laser to operate in a single longitudinal mode. All three lasers could be made to oscillate in a single transverse TEM_{oo} mode, but only the 4 mw He Ne and the argon ion lasers could give single longitudinal modes. The RCA 4 mw He Ne laser has internal mirrors and, thus, random polarization. When the laser tube is first turned on, the polarization rotates with a period of about 1 Hz; but after a 1 day warmup the polarization remains nearly constant over a 1/2 hour period. The longitudinal mode spacing for this laser was 430 Mz so that only 2 or 3 modes can oscillate within the He Ne gain profile. In some internal mirror laser tubes, these modes are orthogonally polarized; thus, by means of a polarizer, one can select one of these modes and reject the others [36,37]. When the polarizer and the laser tube were properly rotated, the output of the differential amplifier arrangement was very near the noise level attributable to the laser shot noise.

With the argon ion laser, an air spaced Fabry-Perot etalon could be placed in the laser cavity to make it oscillate on one longitudinal mode. In every case the noise level for the single mode oscillation was much lower than that for the multimode oscillation.

The reason for the multimode noise is unclear. This effect has been noticed by other observers [38]. It appears to be a heterodyning noise between the modes. The mode spacing of all 3 lasers was greater than 100 MHz, which is well above the range of the detectors so that the beating between two modes is not the problem. However, the frequencies of the individual modes can be pulled slightly so that the mode spacings are not all equal. It is the beating of the mode spacing frequencies that causes a noise in the kilohertz range that is objectionable. In the 4 mw He Ne laser probably only 3 modes were oscillating so the beating of the two 430 MHz mode spacing frequencies gives a single frequency beat that was observable at 20 kHz. With the addition of the polarizer and the proper rotation of the laser tube, only one mode got into the interferometry system and thus the low frequency beating went away. The argon ion laser probably oscillates in 20 or 30 longitudinal modes that are constantly changing phase and amplitude, so that the low frequency beating is not a simple sine wave, but a complex, almost random low frequency noise. Addition of the etalon drastically reduces this noise.

The puzzling effect that goes without understanding is why this noise cannot be canceled out with the second detector. If the multimode laser beam is not sent through the interferometer, but is simply split by a beam splitter and each of the two beams measured by two detectors, the difference of the signals from the detectors will go to the shot noise limit!

There are two basic changes to the system of Figure 5.1 that improve the signal to noise ratio and the stability. To increase stability, a glass plate controlled by a servo system is placed in one leg of the interferometer, as seen in Figure 5.2. A change in the angle of the glass plate relative to the laser beam will cause the beam to travel a different path length through the glass. This is a very old trick that allows one to change the relative phase of one beam over the other and thus position the output fringes at the proper spot.

The relationship between the phase change and light, or detector output is the familiar $\cos^2$ relationship shown in Figure 5.3. The phase changes discussed in this work are so small compared to $\lambda/2$ that a linear relationship can be assumed between phase change and detector voltage. The proportionality constant is determined by where along the $\cos^2$ curve one operates. The angular position of the glass plate determines this operating point. For maximum signal to noise ratio, this operating point should be where the $\cos^2$ curve has maximum slope. These points are labeled in Figure 5.3. This is also the operating point where the linearity approximation holds the best. It should be noted that the sign of the proportionality constant can be either positive or negative, depending on which preferred operating point is chosen. This fact serves as a helpful check for determining if the measured signal is a real phase change or some sort of electrical noise. The phase change signal can be easily inverted by slightly moving the glass plate. Since any electrical noise is most probably independent of the position of the plate, the noise and the signal can easily be separated.

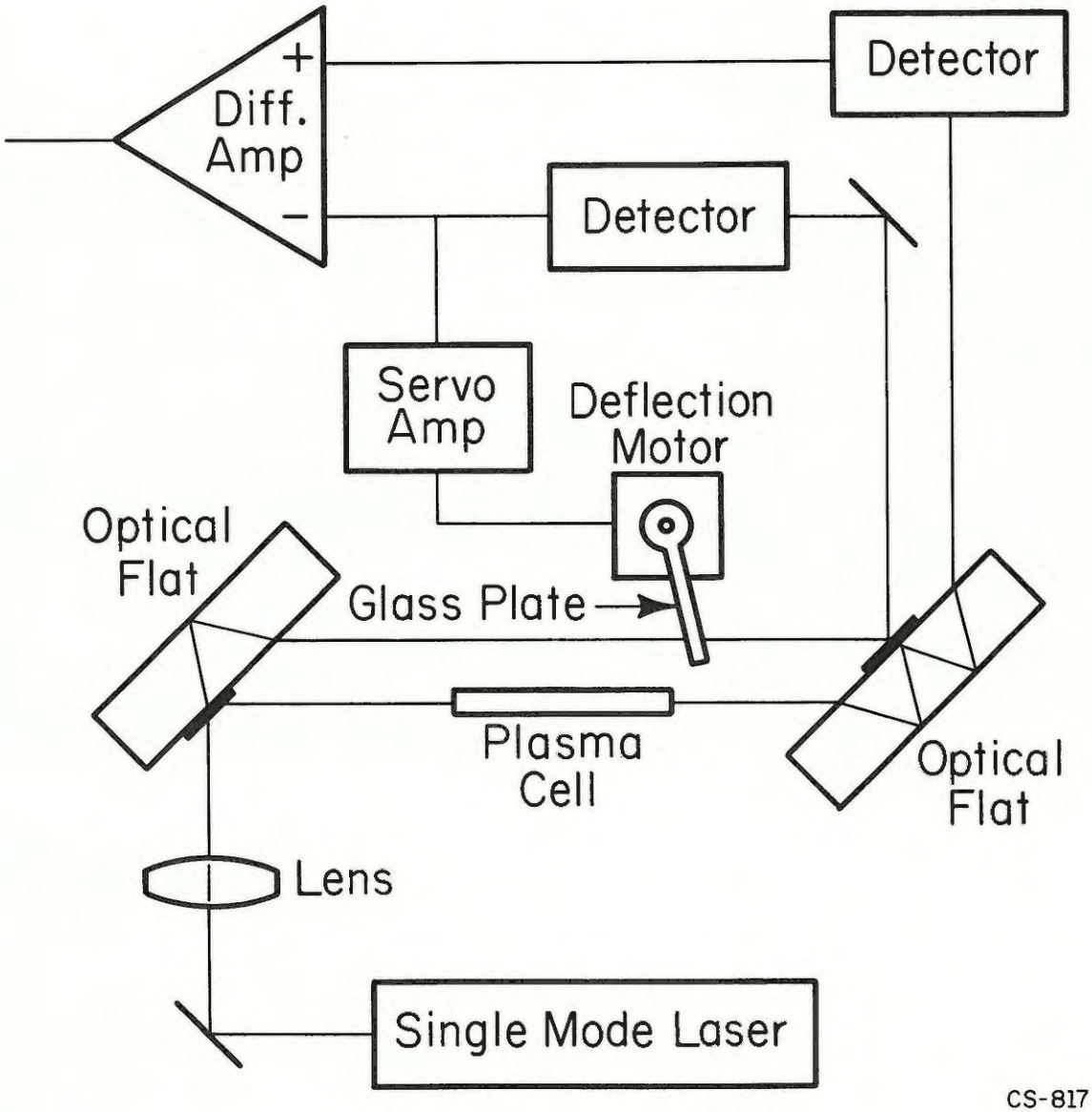

Figure 5.2. Improved interferometry system.

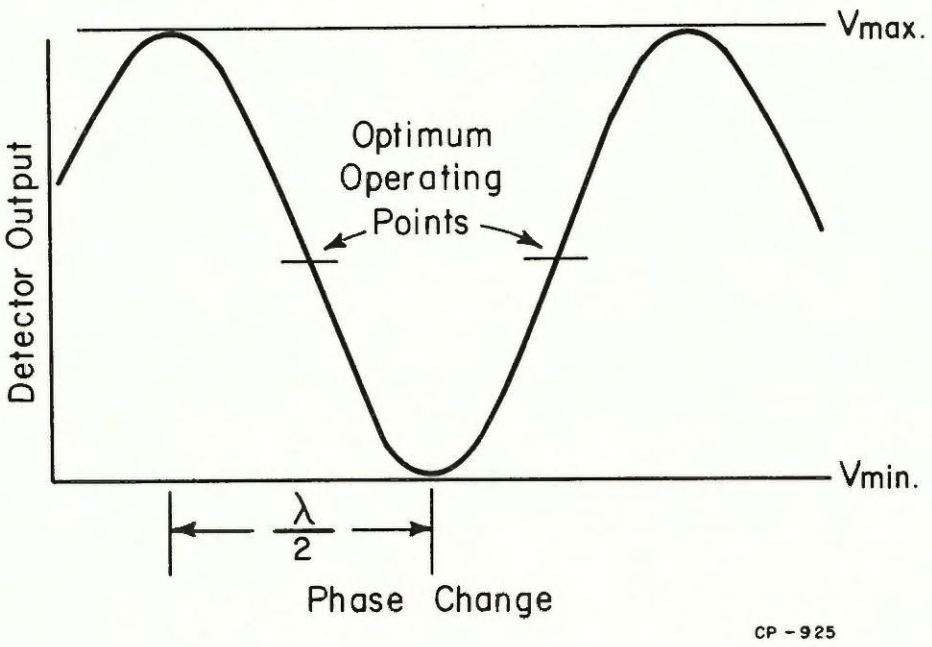

Figure 5.3. Detector output versus optical phase change showing the familiar $\cos^2$ relationship.

This system can be calibrated by recording V_{min} and V_{max} seen in Figure 5.3 while rotating the glass plate. If during operation one assumes that the glass plate is adjusted at an optimum operating point along the $\cos^2$ curve, then the sensitivity in $\mathring{A}$ per volt is

$$\frac{\Delta\mathring{A}}{\Delta V} = \frac{\lambda}{\pi(V_{max}-V_{min})} \quad . \tag{5.3}$$

As discussed above, the Jamin interferometer is very stable; however, over a period of minutes, small temperature changes can cause it to drift. Also, room air currents passing through the interferometer can cause one leg to have a different optical length than the other. Most of these effects have frequency components that are much lower than those of interest for this work. However, these disturbances change the operating point along the $\cos^2$ curve of Figure 5.3 and thus modulate the signals at the higher frequencies. For instance, if signal integration techniques are used to improve the signal-to-noise ratio, a number of minutes might be needed for the integration. Any drift of the operating point due to thermal change would cause a false signal to appear after the integration. Thus, a servo system is needed to hold the interferometer to a fixed operating point. As shown in Figure 5.2, the glass plate is connected to a deflection motor. The motor was driven by a servo amplifier with one differential input connected to the detector output and the other to a variable voltage source. When operating properly, the glass plate rotates until the voltage output from the detector is equal to the variable voltage source. Thus, by adjusting this voltage source, one can define the operating point of the interferometer.

A second improvement over Figure 5.1 is the addition of beam-splitters on the front surface of the flats as indicated with heavy lines in Figure 5.2. This serves to increase the signal-to-noise ratio. From the above discussions, it is clear that when the system is shot noise limited, the signal to noise ratio will be improved with a greater signal at the detector. Also, the signal at the detector should be fully modulated by the interferometer. In Figure 5.1 the laser beam is initially split by the reflectivity of the glass surface. For the proper polarization and the optical flat at 45^{o} to the beam, the reflectivity of the glass surface is approximately 10%. Thus, the two beams are not of equal intensity. When the two beams are recombined, the stronger beam, which goes through the plasma cell, only experiences a 10% reflection. Thus, most of the laser energy does not reach the detector. What does reach the detector is 100% modulated, but its maximum intensity can only be about 20% of the laser beam intensity. The addition of 50% reflecting beamsplitters at the points of surface reflection neatly solves this problem. This makes both beams of nearly equal intensity. The output to the detector is 100% modulated and the maximum signal to the detector can be nearly 100% of the laser signal. However, as shown in Figure 5.3, the interferometer is properly biased when the output is at half maximum so that only half of the laser energy goes to detector 1. It is convenient to place a second detector where the remainder of the energy goes. This is designated detector 2. If the outputs of both of these detectors are fed into a differential amplifier, the laser noise canceling function can also be performed. This eliminates the need for a beamsplitter and detector arrangement between the laser and the interferometer

to do the noise canceling. Such a beamsplitter would have to deflect energy out of the interferometer, thereby reducing the signal to noise ratio. The arrangement of Figure 5.2 allows the total laser power to enter the interferometer, along with the added advantage that the laser noise canceling detector also has a signal. With proper care, the signals entering the two detectors will be 180° out of phase, whereas the laser noise will be in phase. Thus, the output of the differential amplifier will show only the signal plus the shot noise. The balancing of the signals to the detectors is achieved by adjusting the glass plate position.

For ideal beamsplitters with 50% reflection and transmission, the two output beams will have equal power at the correct bias point. This fact can be used to obtain the correction signal for the deflection motor, by feeding the outputs of the two detectors to the inputs of a DC differential amplifier. This technique eliminates the need for an adjustable external voltage reference. The glass plate will always be adjusted to balance the two output signals which will always be at the proper bias point.

Both metallic and dielectric beamsplitters were experimented with on the flats. Metallic thin films of evaporated aluminum and gold were used. Also, quarter-wave dielectric films of ceric oxide were evaporated. The metallic films have the advantage of a more uniform reflectivity as a function of wavelength, making them more desirable for the multi-wavelength work, such as for 6328 $\mathring{A}$ and 1.15 μ. A major drawback of the metal is its absorption, which may be as high as 20% of the incident radiation. This is not too significant in terms of signal reduction, but with a focused 1 watt beam, the metal heats up and quickly evaporates away, destroying that area

of the beamsplitter. The dielectric beamsplitter usually absorbs less than 1% and usually evaporates at a much higher temperature and is thus much more rugged. A second disadvantage of the metal film is that the light experiences an undesirable phase shift in traversing the film. When metallic films are used, the signals measured in detectors 1 and 2 are not 180^{o} out of phase. This causes a loss of signal and also disturbs the bias point that occurs when the signals in the two detectors are balanced. The use of the quarter wave ceric oxide beamsplitter gave a perfect 180^{o} shift. Ceric oxide was chosen because it has an index of refraction greater than 2, and it is possible to evaporate it with a tungsten filament which was readily available. The quarter wavelength referred to above is an optical not a physical length. The reflectivity of these dielectric beamsplitters is about 40% when the electric field vector of the laser radiation is in the z direction of Figure 5.1 and the angle between the beam and the flat surface is 45^{o}. The flats could be rotated so that this angle was less than 45^{o} to make the reflectance reach the desired 50% value. Thus, it was possible to achieve 100% modulation of both of the beams entering the detectors with the desired 180^{o} phase difference.

The lens shown in Figure 5.2 is used to focus the laser beam in the area of the plasma cell to achieve optimum spatial resolution.

5.4 Sensitivity Tests

In order to test the sensitivity of the interferometry system shown in Figure 5.2, a CS_2 Kerr cell was substituted for the plasma cell to give a known phase shift. The geometry of the electrodes was very similar to

the geometry of the plasma cell electrodes discussed in Chapter 6. The electrode gap spacing was 200 μm. They were 1 mm wide and 1 cm long. Reagent grade CS_2 was used in the cell. The phase shift change, Γ in radians, that a light beam experiences after passing through a Kerr cell is

$$\Gamma = 2\pi BLE^2 \tag{5.4}$$

where L is the length of the cell that equals 1 cm in this case, E is the electric field proportional to the applied voltage, and B is slightly less than the Kerr constant which is 3.6×10^{-14} mks units for CS_2 [39]. The fact that Γ changes as the square of the applied voltage is very helpful for this measurement. Since very small phase changes are to be measured, it is necessary to show that some other physical effect such as electrical noise is not really causing the observed signal. Electrical noise, however, would probably show a linear relationship between the measured signal and the voltage applied to the Kerr cell. Thus, adherence to the square law relationship of (5.4) is excellent proof of the validity of the measurement.

To measure the sensitivity of the system, a 50 kHz square wave was applied to the Kerr cell placed in the system of Figure 5.2. Figure 5.4 shows the applied voltage and the signal output of the differential amplifier. This data was taken at 5145 Å using the Ar^+ laser oscillating in a single mode with nearly 1 watt power. The output signal shows a phase shift of about 0.1 Å. This is clearly above the noise level of the system, showing that phase shifts as small as 0.02 Å should be observable. This data was a single shot trace in real time with no averaging.

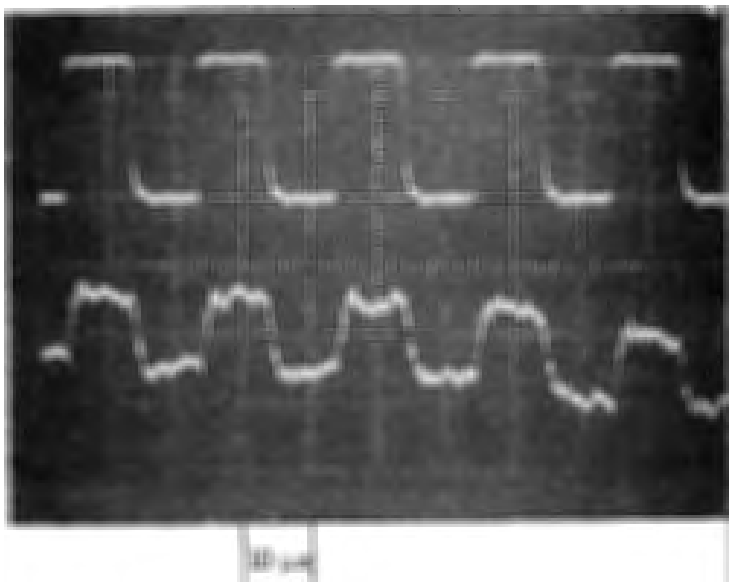

Figure 5.4. Kerr cell voltage in the upper trace and the observed phase change in the lower trace. The voltage scale is 20 V/division and the phase scale is 0.1 Å per division.

When averaging is used these results can be improved considerably. To test the ultimate resolution of this system, a Princeton Applied Research HR-8 lock-in amplifier was used to average the signal shown in Figure 5.4. With a 150 kHz square wave applied to the Kerr cell, the data shown in Figure 5.5 was taken. The time constant was set at 10 seconds with 12 db rolloff per octave. The total magnitude of the phase change was set at 10^{-5} Å. Clearly from Figure 5.5, this magnitude is well above the noise level, implying that a phase change as small as 2×10^{-6} Å could be detectable with this setup. This sensitivity limit could be further decreased with a longer averaging time constant. Clearly this is an extremely sensitive, yet simple system.

Because of the unusually large sensitivities, checks were made to insure that 10^{-5} Å was really being measured. As discussed above, the Kerr cell phase change should be proportional to the square of the applied voltage. Figure 5.6 shows the results of the measured signal for different applied voltages across the Kerr cell. Clearly, the desired square law relationship exists over many orders of magnitude of phase change. Thus, the various possible noise sources can be discounted.

5.5 Excess Noise

Although the result shown in Figure 5.4 is very impressive, it shows a noise signal that is considerably above the shot noise limit of the Ar^+ laser. This fact presented the challenge of improving the performance of the system if the spurious noise could be found. With the lock-in amplifier, the excess noise was found to increase as the frequency was

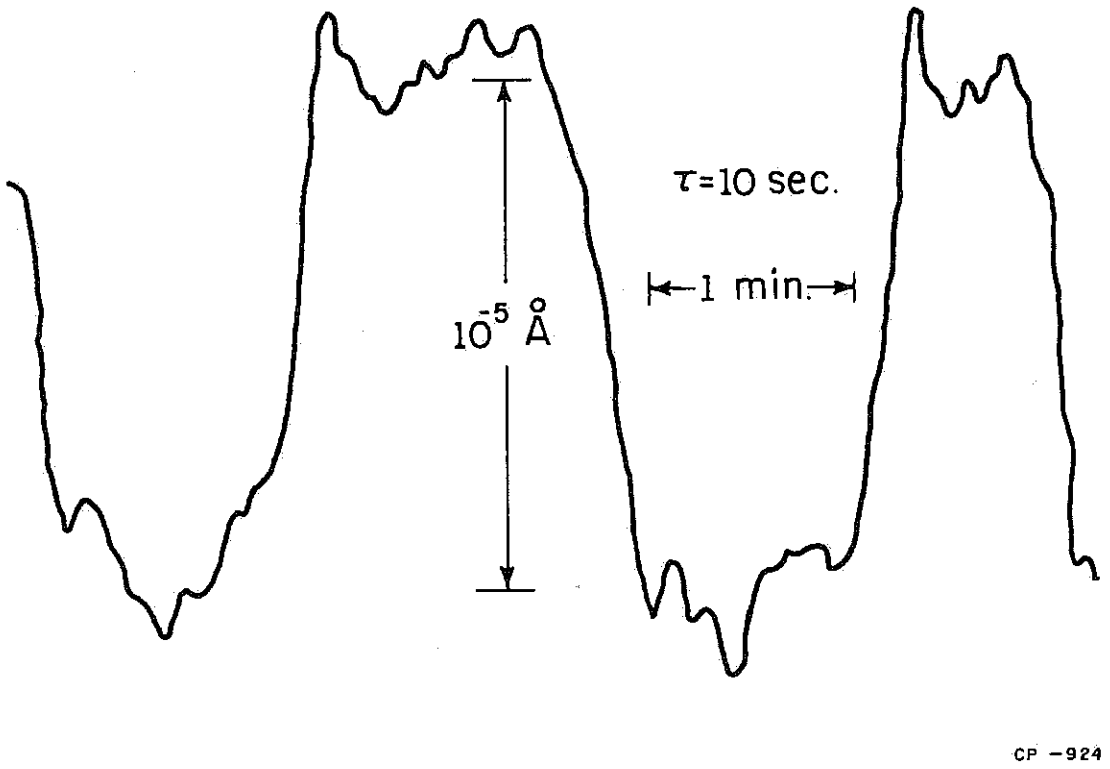

Figure 5.5. Phase change signal due to the change in Kerr cell voltage. This is an average of a 150 KHz square wave.

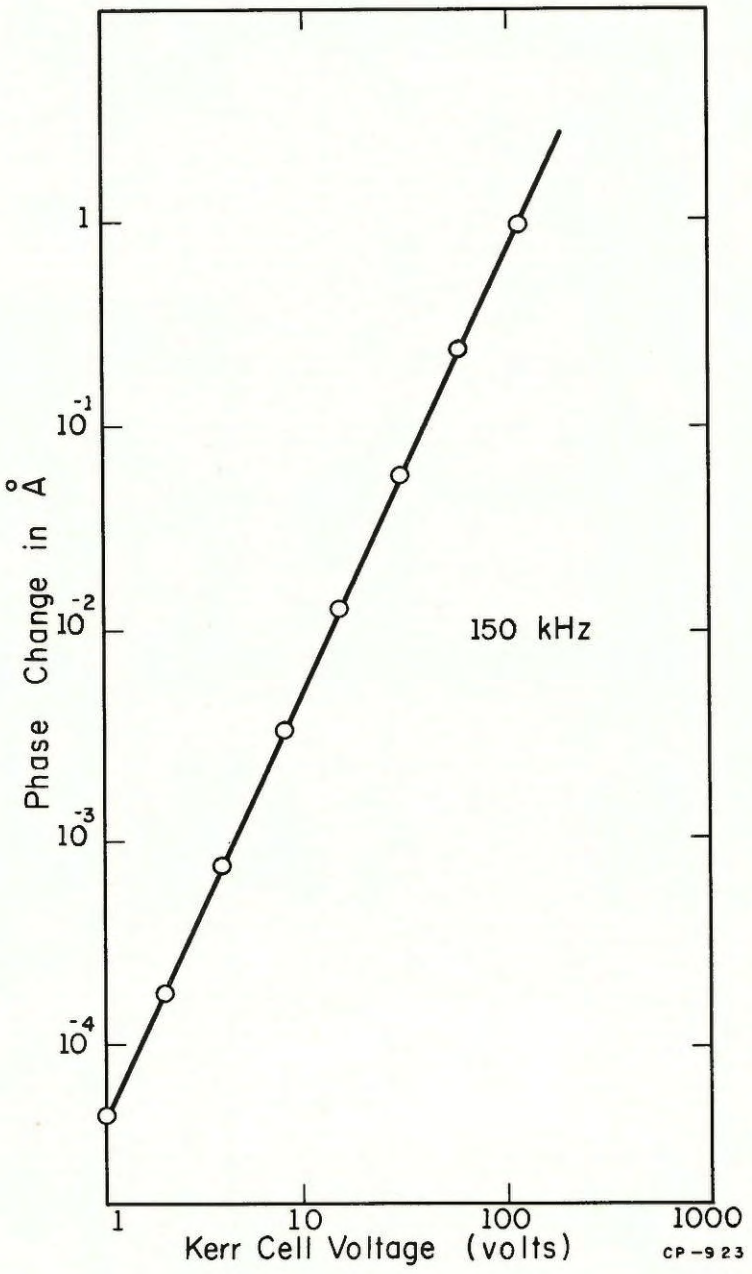

Figure 5.6. Log plot of measured phase change versus Kerr cell voltage. This data confirms the relationship of equation (5.4).

decreased below 150 kHz. This might typify mechanical vibrations of the flats. This was checked extensively by varying the mounting materials and geometry of the optical flat supports and mechanical isolation systems. The noise showed no observable dependence on these variables.

Next a piezoelectric ceramic with appropriate electrodes was used with a square wave generator to introduce mechanical vibrations into the system through the air and by mechanical connections. The amplitude of the ceramic vibration was at least 50 Å, and probably much greater at a mechanical resonance. By adjusting the frequency of the square wave generator, the resonances of the flat supports could be found. The support system was remarkably insensitive to these mechanical vibrations at all frequencies. It was difficult to see any signal even when the ceramic transducer was touched directly to the table supporting the flats. However, a much stronger signal was seen due to sound waves being transmitted through the air and passing through the interferometer. These signals had peak intensity when the sound was at the proper frequency so that a half wavelength was equal to the spacing between the two beams in the interferometer. A plane sound wave at this wavelength with a direction along the y axis of Figure 5.1, will cause a gas density increase in one beam while causing a decrease in the other beam and giving a large differential signal. Other wavelengths will not give such a large signal because the densities seen by the two beams will be more in phase with each other.

Other experiments with the ceramic transducer further indicated that this interferometer was more sensitive to sound waves in air than to mechanical vibrations of the solid supports. One very convincing property

was found when the spacing between the two flats was changed. The strength of the sound wave signal was roughly proportional to the distance between the flats. This is what would be expected for the sound waves in air since the phase change in a laser beam is a measure of the density change integrated over the length of the beam between the two flats. An infinite plane sound wave traveling in the y direction will change the density equally along the path of the beam, making the integral of the density change proportional to the spacing between the flats.

The undesirable noise exhibited by the interferometer system did not have frequency response peaks coincident with the mechanical resonances of the support system. Nor did it have a response peak near the sound in air half wavelength frequency described above. The noise seemed uncorrelated to the distance between the flats. Thus, the noise did not appear to have the properties of mechanical vibrations in the interferometer or of sound waves traveling through the air.

By tuning the lock-in amplifier to various frequencies, it was noticed that the noise had a peak in a couple kilohertz band around 21 kHz. This noise peak had the peculiar property of being fm modulated at 60 Hz. This was eventually traced to plasma oscillations in the Ar^+ laser tube. These oscillations caused an almost unobservable modulation of the laser amplitude; however, they were much stronger at the output of the interferometer. They could not be canceled out by the normal balancing technique described above. If one leg of the interferometer was blocked so that no interference occurred, then the signals in the two detectors could be balanced to the shot noise limit. Thus, this noise seemed inherent in the operation of the interferometer.

A large amount of attention was paid to the possibility that these plasma oscillations were creating a frequency modulation of the laser that was causing the noise. As mentioned before, these experiments were performed with a laser oscillating in a single longitudinal mode, and thus at a single frequency. Instantaneously, the laser may be emitting a very narrow bandwidth of perhaps a few Hz. But over the long term, a number of phenomena can randomly frequency modulate the laser. The prime cause of fm modulation is change in the laser cavity length due to sonic vibrations or thermal drifts. Also, any change in the index of refraction of the Argon plasma tube will change the optical length of the cavity and also fm modulate the laser. The plasma oscillations mentioned above could introduce such an index of refraction change.

If the interferometer is somehow dependent on frequency, then such fm modulation could cause the observed noise. To test this, the laser was purposely fm modulated by placing a piezoelectric ceramic on one of the laser mirror mounts so as to change the length of the cavity with an applied voltage. Modulating the laser in this way caused a signal at the interferometer output that could not be canceled out by balancing the detectors. This signal seemed to have all of the properties of the noise signal except its randomness. Thus, the noise could clearly be attributed to the laser and possibly was due to an fm modulation.

The question then arose as to why the interferometer might be frequency sensitive. Attention was first paid to the possibility that the two paths of the interferometer were not equal. If this is the case, then the relative phase of the two beams being combined at the output beamsplitter

will change as the frequency changes and thus give the observed noise. In this case, the positioning of the optical flats should have a strong effect on the observed noise. However, experimentally no correlation could be found. Also with a little practice, the flats could be oriented so that the path difference between the two legs was less than a wavelength of light. When this was achieved a black fringe could be observed with the eye when the light source was a white tungsten incandescent bulb. This shows almost the ultimate in frequency insensitivity, when photons throughout the visible spectrum all place a fringe at the same spot. If the path lengths were changed by as much as a single wavelength, the black fringe became colored. The fact that both legs of the interferometer had equal length had no observable effect on the noise or on the signal introduced by the piezoceramic modulating the laser cavity. Thus, the frequency dependence of the interferometer did not seem to be large enough to cause the observed noise.

The source of the noise was finally located when it was realized that cavity vibrations and plasma oscillations could also slightly angularly deflect the beam coming from the laser. Such deflections would cause a slight path difference in the two legs of the interferometer due to slight imperfections of the flats thus causing the observed noise. The use of the piezoceramic to change the length of the cavity in the fm modulation test also had the effect of slightly tilting one laser mirror which would angularly deflect the beam. To test this idea, the beam was slightly deflected independent of the laser with a mirror attached to a piezoceramic. The signal applied to this deflector did show up at the interferometer output and had the same properties as the noise except in randomness. This

deflection was very slight, causing the beam to be displaced only about 1 μm at the interferometer, yet it was easily detectable at the interferometer.

The random angular deflections of the laser were measured by splitting the beam down the center with a mirror that reflects the left half of the beam to one detector and lets the right half fall on a second detector. The outputs of the two detectors are fed to a differential amplifier so that when the beam is properly centered, the amplitude fluctuations of the laser beam balance out. Any small movement of the beam causes the signal in one detector to increase, with the other signal decreasing, thus causing a signal at the differential amplifier output. The movements were seen to have the same frequency characteristics as the noise in the interferometer. Expecially apparent was the noise due to the plasma oscillations at 21 kHz. The deflection signal was considerably bigger than the amplitude variation measured when one detector received the whole beam. Thus, the strong correlation between the motion of the beam and the observed noise seems to indicate it as a prime cause.

The noise spectrum around 1 kHz was also very large due to the resonant acoustic vibrations of the laser cavity that caused small deflections of the beam. These vibrations were fed by the turbulence of the laser cooling water. When the water pressure was decreased to the point just above the flow rate cutoff of the laser, the turbulence decreased considerably and a great deal of the lower frequency noise decreased significantly. For the plasma panel studies, this low frequency noise was of little concern and could be filtered out with standard electrical filters.

It is interesting to consider what a 1 μm displacement of the beam would mean to this interferometer. This small displacement causes the noise because of surface irregularities and inhomogeneous volume properties of the otpical flats. The flats used here were made of schlieren free grade fused quartz with surfaces flat to $\lambda/20$, with a laser grade surface polish and with the two surfaces parallel to one arc second. Even with these excellent properties, simple analysis shows them inadequate for these purposes. Take, for example, the fact that the two surfaces are parallel to only one arc second. If the laser beam moves only 1 μm across the flat, a 1 arc second angle between the two surfaces will cause an increase in thickness of $\frac{1\ \mu m}{60 \times 60 \times \frac{360}{2\pi}} = 0.048$ Å. This is clearly a strong enough variation in thickness to cause the noise shown in Figure 5.4. Also, slight surface irregularities in the surface could easily cause the small phase shifts observed when the beam is slightly deflected. The irregularity of a single plane of atoms would be more than sufficient to cause the observed noise. The reason that the noise is not much bigger is due to the averaging effect that the beam performs when it passes through a large area of atoms. The optical length of the flats is also determined by the index of refraction of the quartz, which is not homogeneous. The best grades of optical quartz typically have a maximum index variation Δn of 10^{-6} over the aperture of the flat. This represents only a 2 part per million change in index and at first appears quite good. However, for the flats used here, with a thickness of 6.3 mm, an index change of 10^{-6} represents a phase change of 63 Å, which is quite large for these experiments. Fortunately, the index does not vary rapidly as a function of the distance across the aperture so that the 1 μm variations

in the beam position do not cause the beam to experience an index change anywhere near the 10^{-6} factor discussed above.

5.6 Potential Improvements

No attempts were made to reduce the noise problem discussed above since the existing resolution of the system was quite adequate for the measurements discussed in Chapter 6. However, some improvements could certainly be made. Better grade optical flats could be used. Those used in this experiment were of a very high quality, making improvements here difficult. A better approach would be to eliminate the vibrations in the beam. This could be done with a control system. The motions of the beam would be detected by the two detector position sensing system described in section 5.5. Its output would be fed through a feedback amplifier to an electro optic deflector that would correct the direction of the beam. The response of the deflector would have to be at least as fast as the fastest laser deflection to be corrected, which is about 150 kHz for the laser used here. It would be desirable to have the deflector respond much more rapidly so that the gain of the servo system can be increased without oscillations occurring due to deflector-induced phase shifts. Mechanical deflectors are much too slow. Acousto-optic deflectors may be fast enough, but their response is delayed a number of microseconds by the time for the sound wave to travel through the acoustic media. Thus, the acousto-optic deflector may cause phase delays that could make the servo system unstable. The most desirable deflector for these purposes seems to be the KDP electro optic deflector [40]. This deflector can have response times as short as 1 ns.

However, it is rarely used because of the high voltage (thousands of volts) required to deflect the beam only one beam diameter. It is ideally suited for this application since a 1 μm deflection is only 10^{-3} beam diameters, making the required voltage swing only a few volts. The fast response of this deflector would make the limit on the phase delays dependent primarily on the servo amplifier, thus allowing a very high gain at the 150 kHz frequency before oscillation sets in. It is, of course, necessary to have two of these deflector servo systems in order to correct for displacements in both dimensions.

It is interesting to speculate as to whether the deflectors are needed at all. Since the spurious movements of the laser beam are very small, for a given position of the beam on the flats there may be a simple linear relationship between the motion of the beam and the noise output of the interferometer. This would occur only if the disturbing phase change phenomena, such as an index of refraction gradient, varied very slowly as a function of the micron sized displacements of the beam. The noise output from the interferometer could be balanced out by combining the interferometer signal with the output from a position sensing detector by means of some differential amplifier arrangement.

5.7 Conclusion

In conclusion, a very simple interferometry system has been described that can detect small phase changes: possibly smaller than any previously described in the literature. Real time phase changes on the order of 10^{-2} Å are readily observable. By means of signal averaging and

integration, phase changes on the order of 10^{-6} Å are observable. The closest result known to the author that approaches this sensitivity was a 10^{-5} Å phase change measured by Boersch et al. [41]. They used integration time constants similar to those used here in the measurement that achieved $\sim 10^{-6}$ Å. Their experimental setup was much more complicated and more difficult to set up than the one presented here. This technique requires no complicated alignment steps. Expensive vibration isolation systems do not appear necessary. Unlike the many sensitive interferometry techniques that can measure small phase changes inside a laser cavity, this technique can give superior performance even with lossy materials. Thus, expensive Brewster windows or anti-reflection coating are not required.

The present limitation of the system used here was not the fundamental shot noise limit. The source of excess noise has been located, and it should be correctable through simple electrical techniques.

CHAPTER 6

OPTICAL INDEX OF REFRACTION MEASUREMENTS

6.1 Introduction

This chapter describes the techniques and measurements that show the optical index of refraction changes as a function of space and time in the gas volume of the plasma display cell. These measurements were performed in hopes of being able to measure the plasma density distribution predicted in the computer simulation described in Chapter 2. The results of Chapter 5 have shown that a simple interferometer is capable of measuring the very small index of refraction changes caused by the plasma. However, the results of this chapter will show that index of refraction changes due to neutral atom density variations present a severe noise problem that makes the plasma density measurement difficult. On the other hand, considerable knowledge is obtained about the neutral atom density changes.

6.2 Experimental Cell Dimensions

To start with, special plasma cells had to be constructed to place in the interferometer. These cells had to be compatible with the interferometry measurement and still closely approximate the actual physical conditions found in typical plasma display panels. The most popular structure is that shown in Figure 1.1 which was developed at Owens-Illinois [1], and is presently being manufactured under the trade name of Digivue. The substrate is typically $\frac{1}{4}$ inch thick plate glass that gives the structure rigid support. The dielectric glass layer is usually about 25 μm thick and the gas discharge gap spacing is about 100 μm. These dimensions may vary by factors as great as 2 for various panels.

The electrode geometry used for experimental interferometry cells is shown in Figure 6.1. The length dimension of this cell is a major departure from the dimensions of an ordinary plasma cell, but it is necessary to make this cell as long as possible in order to maximize the phase change of the light through the interferometer. The maximum length of the cell is limited by the depth of focus of the optical beam. The depth of focus is determined by the focal length, f, and the diameter, D, of the colimated beam at the lens. These two quantities also affect the diameter, w, of the beam waist at the focal point by the well-known formula

$$w = \frac{4\lambda f}{\pi D} \quad . \tag{6.1}$$

The depth of focus, a, is approximately

$$a = \frac{2wf}{D} = \frac{8\lambda f^2}{\pi D^2} \quad . \tag{6.2}$$

From these two relations it can be shown that

$$w = \sqrt{\frac{2a\lambda}{\pi}} \quad . \tag{6.3}$$

It is seen that there is a compromise to be made between the depth of focus which determines the length of the cell and the beam waist diameter which determines the spatial resolution of the measurement. For the 1 cm depth of focus needed for Figure 6.1 the optimum beam waist of about 57 μm is smaller than the 180 μm discharge gap; making the spatial resolution reasonable for this measurement.

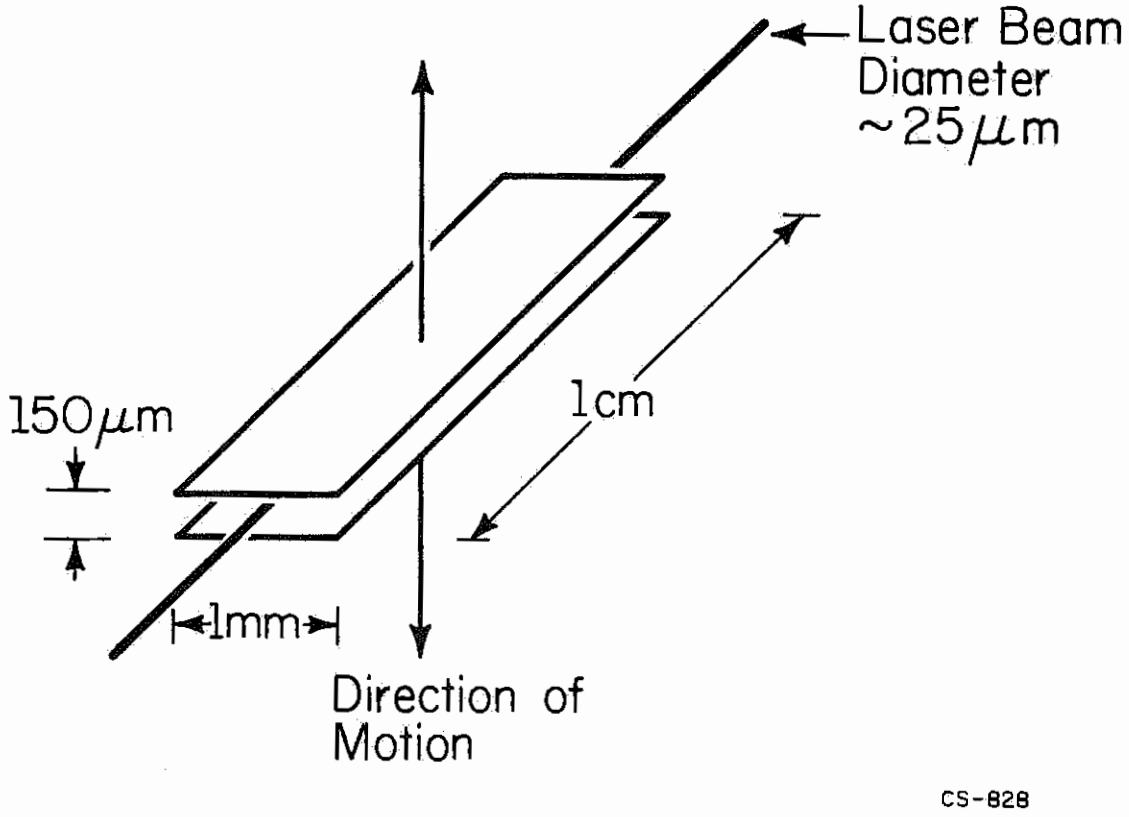

Figure 6.1. Electrode geometry for experimental plasma cell used to measure index of refraction variations.

6.3 Cell Construction

A considerable amount of effort went into developing the techniques necessary for making bakable, experimental plasma cells with an all glass structure. Although this process is done in industry on a routine basis, the techniques are regarded as a proprietary art. Thus the steps of construction, found here to be successful, will be presented in detail.

The cell was started by screen printing and firing the electrodes shown in Figure 6.1 on 3 mm thick window glass substrates. The electrode paste was Electro-Science 8080 which fires to a thin film gold that sticks very well to glass. Considerable experimentation showed that a 120 mesh stainless steel screen gave the proper thickness of the paste. A thicker paste would cause the gold to flake off after firing. A thinner paste would leave the gold too thin, causing it to be dissolved during the dielectric processing steps. The resulting gold film was measured to be about 3000 Å thick. A two zone belt furnace was used for firing. The first zone was set at 200°C and the second at 640°C. This is just below the temperature at which the window glass substrate begins to soften and sag.

The second step is to screen print the dielectric glass layer over the electrodes and substrate. This dielectric glass must soften at a much lower temperature than the substrate glass and also must have nearly the same expansion coefficient of 85×10^{-7} per degree celsius. Initially such a glass was made in the lab from raw chemicals. This was a rather involved and time consuming process. Later, Electro-Science 4011C paste was found to give good results. A 80 mesh stainless steel screen was found to give a final fired thickness of about 25 μm. The same 2 zone belt furnace

was used with a complete cycle of about 30 minutes. The first zone was set to 390°C and the second to 640°C. The result was a reasonably flat transparent dielectric layer over the thin film electrode. For electrical connection purposes, the total electrode geometry looked like a T. The horizontal bar of the T was the discharge cell electrode shown in Figure 6.1, and the vertical bar is for connecting the sustainer. Part of the connecting bar was left uncovered by dielectric so that electrical connection could be made.

Two of these substrate electrode structures are connected to make a cell. Two thin glass rods are used to separate the two substrates and define the discharge gap spacing of 150-200 μm. If a bakable cell is to be made, the two pieces must be connected together with another glass. This glass must meet all of the expansion coefficient requirements of the other glass materials and it must fire at a lower temperature than the dielectric glass so as not to disturb it. Because of the structure of this cell, a number of pieces must be attached during different firing cycles. Thus the solder glass from previous firing cycles must not soften. This problem is solved by using a devitrifying solder glass. This material has the properties that while it is being fired, it crystalizes and sets. On subsequent firings, the glass will remain set, and would have to be fired at a much higher temperature before it would soften. The solder glass used here was Owens-Illinois CV-97. It was mixed in powdered form with a solution of nitrocellous in amyl acetate, that acted as a binder. The resulting slury was placed in the areas to be sealed. The pieces were fired in an oven for one half hour at 390°C to burn out the binder and then at 470°C for 1½ hours to set the glass.

The first firing stage was used to connect the two substrates together at the proper gap spacing and orientation. The cell was then sawed at two ends in preparation for the entrance and exit window mounting. The laser beam shown in Figure 6.1 is normal to the saw planes. Both saw planes were positioned as close to the electrode as possible without touching. Two more solder glass sealing and firing steps were performed to attach the windows. A final solder glass sealing cycle was needed to connect the gas filling tubulation to a hole drilled in one of the substrates. The cell was then ready for evacuation, bake-out and gas filling. The cells were typically evacuated to better than 10^{-7} torr. The bakeout was usually about 350^{o}C. The filling gases were always research grade inert gases.

For some cells, where quick and easy results were desired, the substrates, windows and tubulation were all sealed using Torr Seal vacuum epoxy. These cells could not be baked out and thus the gas mixture would become contaminated after a few hours. However significant results can be obtained shortly after filling.

6.4 Cell Positioning in the Interferometer

The completed cells were positioned in the beam waist of the interferometer with standard micromanipulators having micrometer head drives. This alignment step is a little tricky, but with practice, the cell can be in complete alignment with the beam in less than 5 minutes. Figure 6.1 shows that the cell is moved in a vertical direction relative to the beam in order to probe the various regions of the space across the discharge gap. This is done very easily and accurately with the micrometer headscrew.

It should be noted that the cell can be placed in either leg of the interferometer as shown in Figures 5.1 and 5.2. However the leg shown in Figure 5.2 is preferred. For reasons discussed later in this chapter, it is desirable to be able to operate the interferometer at a number of different laser wavelengths. Because of dispersion in the optical flat material, the beam in the cell shown in Figure 5.1 will be in a different position for each wavelength. This is obviously a disadvantage if the wavelength response for a single point in the cell is desired. The cell positioning shown in Figure 5.2 does not have this problem since the beam arrives at the cell through a reflection that must have no angular dispersive properties.

6.5 Experimental Results

Figure 6.2 shows typical phase change results obtained with the Ar^+ laser in a cell with electrodes of approximately the geometry shown in Figure 6.1. The beam is positioned at the center of the discharge gap. Each discharge of the cell is seen to initiate a series of strong oscillations that damp out with time. These phase changes are not typical of electron density changes but rather of neutral atom density changes [42,43]. In a simple analysis, there are two density changes that can be measured by measuring the phase change of transmitted light. The phase change of the electrons, behaves as described by equation (5.1). When the phase change due to the neutral atoms is added, the total phase change in radians is

$$\Delta\varphi_{tot} = \frac{2\pi L\alpha\Delta N_a}{\lambda} - B\Delta n_e L\lambda \quad , \tag{6.4}$$

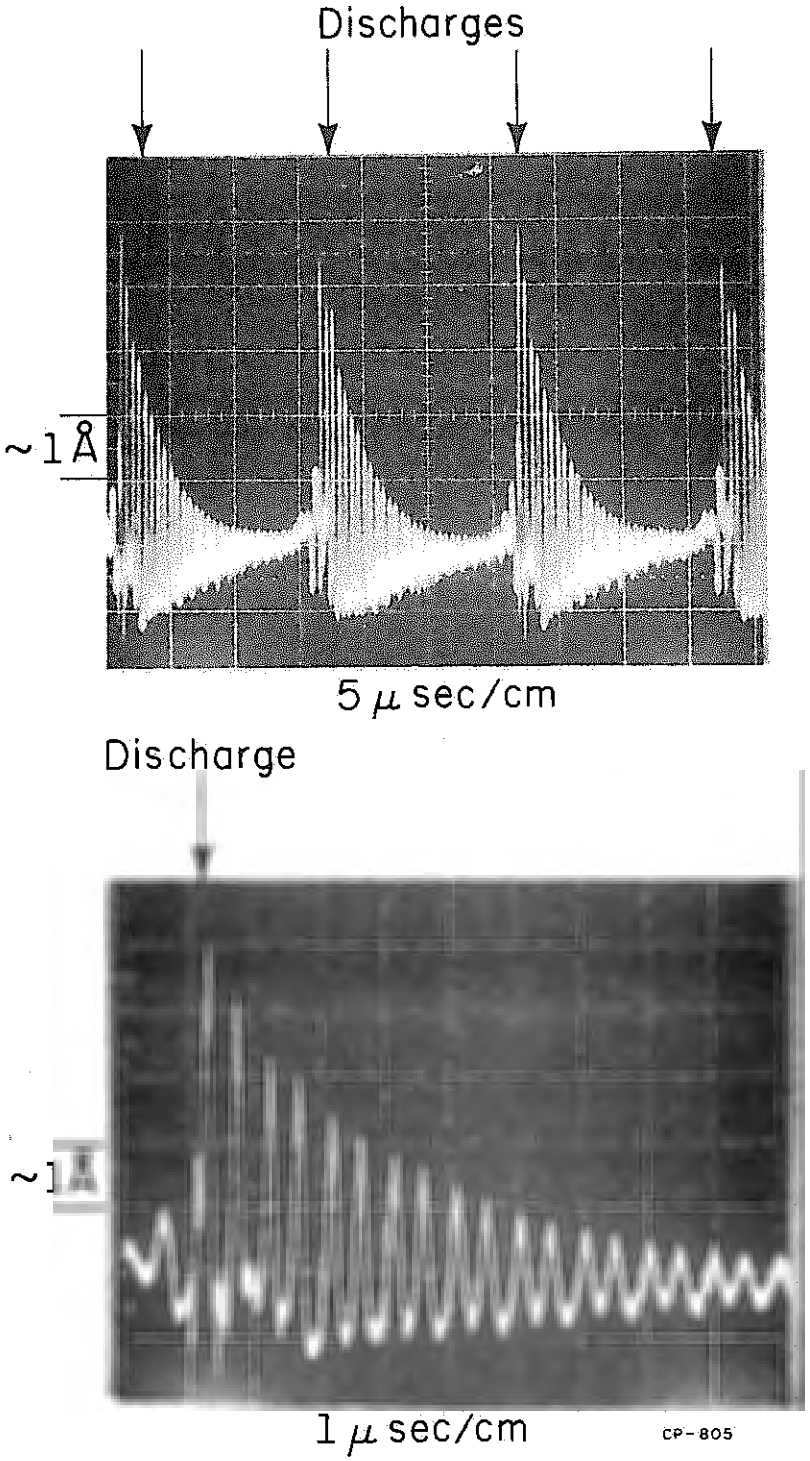

Figure 6.2. Typical phase changes observed in the experimental plasma cell. The index of refraction increases upward. The beam is positioned in the center of the cell.

where L is the length of the plasma cell which is 1 cm for this case, ΔN_a is the change in atomic number density, and α is a constant which is characteristic of the gas. It can be found from

$$\alpha = \frac{n_o p}{KTN_o} \tag{6.5}$$

where n_o is the gas index of refraction at STP, p is the pressure in pascals (1 torr = 134 pascals), K is Boltzman's constant, T is temperature, and N_o is the number density of atoms at STP. $N_o = 2.71 \times 10^{25}\ m^{-3}$.

Since both neutrals and electrons give a phase change, it is not easy to separate the two effects. Although the two terms in equation (6.4) have differing signs, there is no way of telling whether the electron or atom density is increasing or decreasing, making the sign information of little value. The standard solution used by most researchers is to perform the measurement at a number of wavelengths [35]. Because of the wavelength dependence of the two terms, there is a possibility of separating them.

The measurement of plasma display cell phase changes shown in Figure 6.2 shows rapid changes that are primarily due to atomic density changes. The density changes are due to sound waves that are initiated by the gas discharge. These sound waves travel back and forth from the anode to the cathode for many cycles before they are damped out by absorption. The exact nature of these sound waves can be determined by observing them for different positions along the discharge gap. Figure 6.3 shows the cell discharge current and the phase changes for five differing positions along the discharge gap. The lowest trace shows the discharge current. Progressing

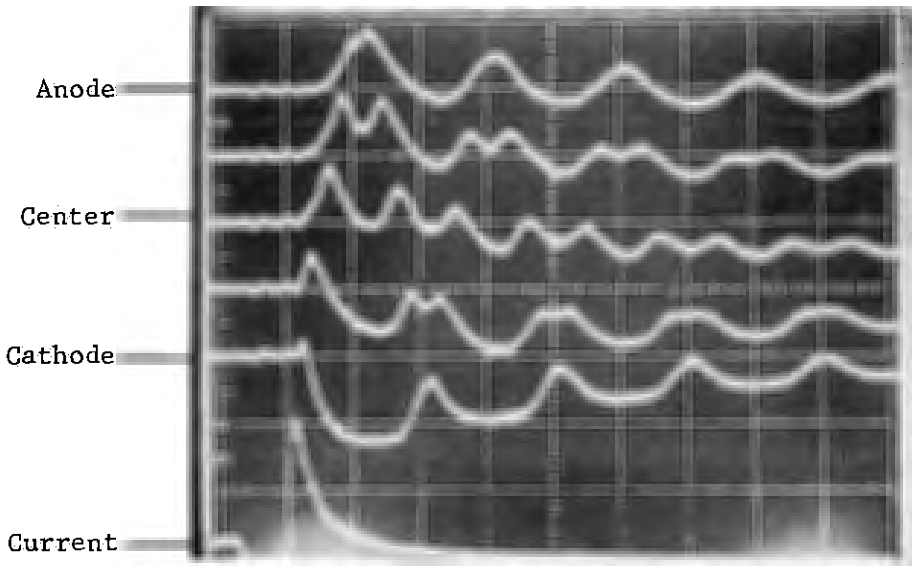

Figure 6.3. Measured phase changes for various positions along the discharge gap. The lowest trace is the discharge current. The 5 remaining traces show the phase changes for various regions. Index of refraction increases upward. The vertical scale is 5 Å per division and the horizontal is 0.5 μs per division.

upward, the next trace shows the phase change at the cathode. The third trace shows the phase change 54 μm from the cathode. The remaining traces are spaced by 54 μm, the top trace being at the anode. From Figure 2.16, it is seen that most of the discharge activity occurs near the high field region of the cathode. The hot electrons near the cathode will locally heat the neutral atoms. The more energetic neutral atoms will fly out of the cathode region and thus cause a decrease in density. This decrease is very clearly shown as a strong decrease in the index of refraction at the cathode at the time of the discharge. The impulse of atoms flying out of the cathode region sets up a sound wave that is first seen a short distance away from the cathode as an increase in index of refraction. The sound wave travels through space and time until it hits the anode in the top trace and is reflected back to the cathode. This bouncing between the cathode and anode continues for many microseconds as shown in Figure 6.2.

The question arises as to how much of the phase change shown in Figures 6.2 and 6.3 is due to electrons. Clearly the rapid oscillations are due to the neutral density changes since the waves observed in Figure 6.3 travel at the velocity of sound. However, Figure 6.2 shows lower frequency components that may be due to electron density changes. To check this, the interferometer was operated with a home built He Ne laser that oscillated simultaneously at 6328 Å and 1.15 μm. From equation (6.4), the ratio of the neutral phase change to the electron phase change should be 3.1 times smaller at 1.15 μm than 6328 Å. Thus any electron phase changes that are observable in Figure 6.2 should show up much more strongly at 1.15 μm. The sensitivity of the interferometer with less than a milliwatt coming from the He Ne laser,

was considerably less than that shown in Figure 6.2. However with a boxcar integrator, the phase changes due to the shock waves could be resolved as good as shown in Figure 6.2. As closely as could be measured, the phase changes in radians were inversely proportional to wavelength for both wavelengths. Thus to the resolution of Figure 6.2, all of the phase change is due to neutrals. This is not too surprising, since calculations presented in section 5.2 showed that an electron density of 10^{12} cm^{-3} should yield a phase change of only $\sim 10^{-2}$ Å. The data shown in Figure 6.2 is scaled at $\sim$1 Å per division. Thus one could hardly expect to see an electron phase change even at 1.15 μm with this resolution. The neutral atom phase changes seem to amount to a 5 Å shift. Thus there could easily be a ratio of 500 between the neutral and electron phase shifts. To separate these two by a two wavelength experiment will require an accuracy of the measurements much greater than that given by oscilloscope traces and possibly even by boxcar integrators. For the moment it appears that even with the very sensitive interferometry system described in Chapter 5, the electron density cannot be measured because of the neutral density noise.

6.6 Neutral Density Measurements

More will be presented later on in this chapter discussing ways to get around this noise problem, but for now lets examine what can be learned about the discharge from our ability to very accurately measure the neutral atom density in space and time.

A basic assumption that was used in all calculations presented in Chapters 2 and 3 was that the neutral atom density was constant. This is of

course an approximation, but how good of an approximation? From equation (6.4) and Figure 6.3, it can be easily calculated that a 5 Å phase shift represents only a 2×10^{16} cm^{-3} change in density. Since the atomic density at 250 torr and 25°C is 8.84×10^{18} cm^{-3}, it is seen that the perturbations are clearly very small, making the constant density approximation a good one for the neon + 0.1% Xe mixture.

This is probably not true for all gas mixtures, however. An example is shown for 250 torr xenon. Pure xenon is an attractive choice for color plasma display panels that use the ultraviolet light generated by the xenon to excite phosphorus [44]. Figure 6.4 shows the sound waves for a cell with 250 torr xenon. The sound waves give about a quarter wavelength phase change. Such a large phase distorts the approximate linear relation between the phase change and the output of the interferometer, however the $\cos^2$ relationship shown in Figure 5.3 still exists. This large phase change is partially due to the fact that the index of refraction at STP of xenon is 1.000708 [45] whereas that of neon is only 1.0000673 [46]. However the atomic density change due to the sound waves in xenon is also very much larger than that of neon. The data of Figure 6.4 shows density changes as great as 10% of the equilibrium density. The approximation of uniform neutral density starts to breakdown and thus the effects of the soundwaves must be included in the discharge simulation.

The measurements presented above show only the high frequency changes in neutral atom densities. There is, however, a steady state change that occurs depending on whether the cell is on or off. This density change is governed by the heating of each discharge and the thermal relaxation or

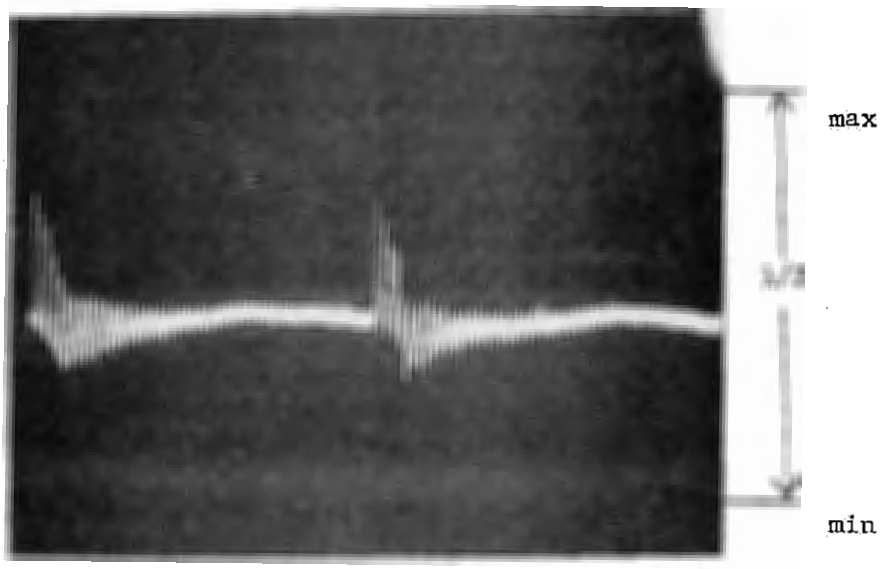

Figure 6.4. Sound waves observed in 250 torr Xe. The horizontal scale is 10 μs per division.

cooling of the gas. Thus this steady state change is established after a number of discharges and is strongly dependent on the repetition rate of the discharges. To measure this, the cell was effectively turned on and off by interrupting the sustain generator for many cycles. This data is shown in Figure 6.5 where the cell, which was initially sustained at a 50 kHz rate, was turned off by stopping the sustainer. The neutral density increases to its equilibrium value in a few hundred microseconds. After the equilibrium value is reached, there are still small fluctuations due to sound waves traveling long distances through the entire cell structure. After 9 milliseconds of interruption, the sustainer was again applied and the discharges caused a new steady state value to be achieved. The wide band structure of the second half of the trace is due to the high frequency sound waves bouncing between the anode and cathode in the manner shown in Figure 6.2. Figure 6.6 shows data for the same experiment but with only a 1 millisecond sustainer interruption. The time constant for the relaxation of the gas density to equilibrium appears to be about 100 μs. Figure 6.7 shows data for even a shorter time scale where the interruption of the sustainer was only about 150 μs. In this case the cell never reaches a steady state situation. The sound waves reflection between the cathode and anode are clearly visible here. With each discharge the neutral atom density decreases slightly due to the additional heating that each discharge introduces.

It is interesting to note that in the last 3 figures, the maximum and minimum of the light from the interferometer was set to be at the top and bottom lines of the scope grid. Thus again the scope traces do not have a linear relationship with the phase change. But clearly the phase change

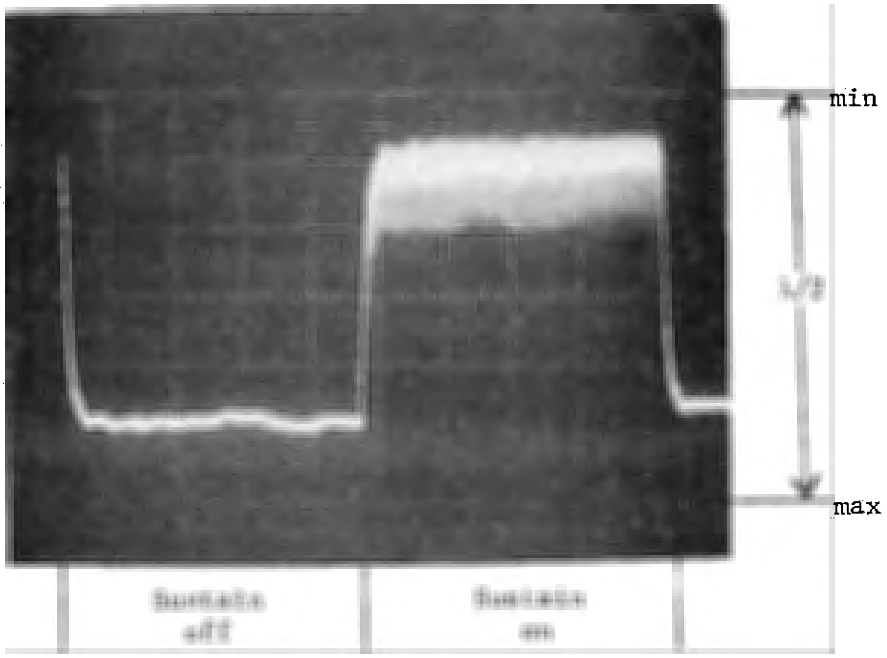

Figure 6.5. Steady state phase change component in 250 torr Xe due to interruption of the sustainer. The horizontal scale is 2 ms per division. The sustain frequency was 50 kHz. The index of refraction increases downward.

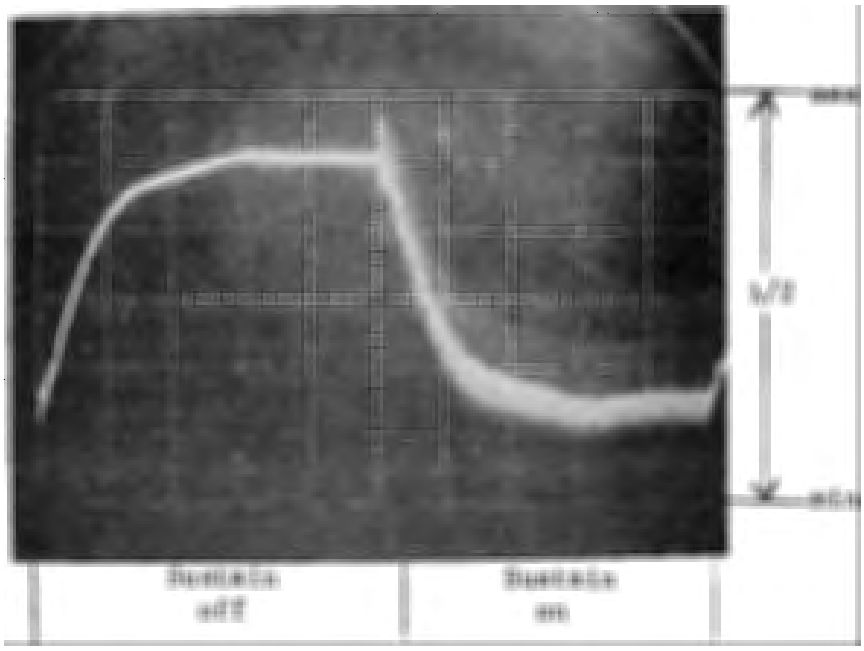

Figure 6.6. Phase change for the same conditions as in Figure 6.5, except with only a 1 ms interruption. The horizontal scale is 200 μs per division. The index of refraction increases upward.

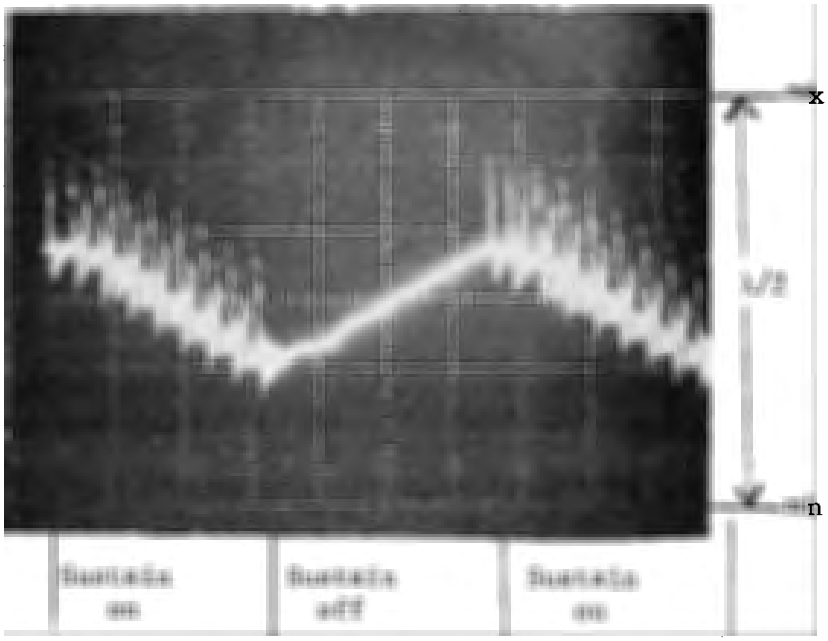

Figure 6.7. Phase change for only a 150 μs interruption. The horizontal scale is 50 μs per division. The index of refraction increases upward.

shown here is between a quarter and a half wavelength. Such large phase changes are easily observable with the eye. This could be done by turning the sustainer on and off at a rate below 10 Hz. These phase changes were observed at all frequencies down to DC, indicating that the relaxation time of 100 μs is the only one of importance.

The thermal conductivity of neon is much greater than that of xenon so that the cell reaches steady state much more quickly as seen in Figure 6.8. However because of this greater thermal conductivity, less thermal energy can be stored in the gas and thus the neon neutral atom temperature is much closer to the temperature of the glass wall. Thus the steady state density changes in neon are not as great as those for xenon.

6.7 Neutral Temperature Measurements

The above measurements indicate the nature of the neutral density changes in the gas. Some of these density changes are caused by temperature changes. The temperature changes are indirectly measurable by observing the density changes that they cause. For instance, in Figure 6.3, the trace of the phase change at the cathode shows that at the time of the discharge, the index of refraction dropped sharply. This is a decrease in neutral density directly attributable to a sharp increase in temperature near the cathode region. The traces of Figure 6.3 for regions away from the cathode do not show this sharp drop at the time of the discharge and thus there is not much heating. One problem with this technique is that the sound waves also cause similar changes in neutral density. Thus it is easy to misinterpret the observed phase changes. Nevertheless, this is a useful qualitative technique for observing the areas of heating.

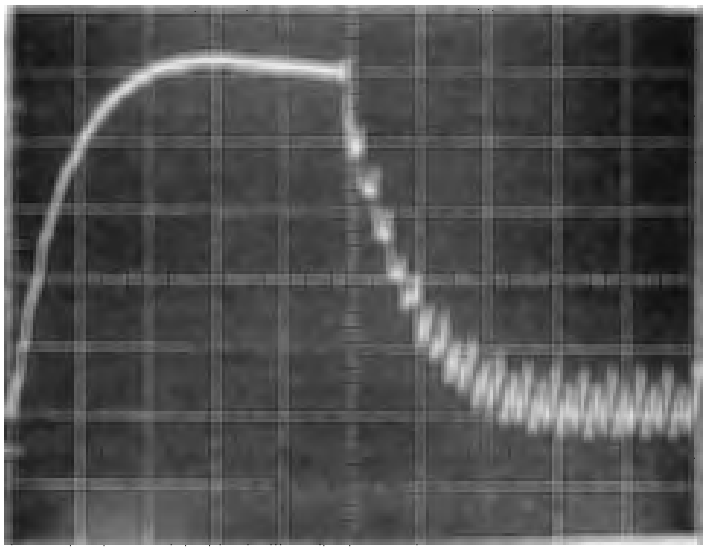

Figure 6.8. Steady state phase change data for a neon plus 0.1% xenon mixture. The vertical scale is 10 Å per division and the horizontal scale is 50 μs per division.

A second problem with determining the temperature change by watching the neutral density change is that one finds out only the temperature change and not the actual temperature. As indicated in Figures 6.5 through 6.8, it typically takes a number of discharge cycles before the gas comes to an equilibrium temperature. Thus a technique is needed to measure the absolute temperature of the gas. Fortunately a simple way of doing this is to measure the velocity of the sound waves bouncing between the cathode and the anode. The velocity of sound in a gas is proportional to the square root of temperature and very weakly dependent on gas pressure. This pressure dependence is too weak to be of concern for the following calculations. By measuring the time for the sound waves to make many cathode-anode transits, the velocity can be accurately determined with knowledge of the cathode-anode gap spacing. To make the temperature measurement less dependent on the gap spacing measurement, the sound wave velocity was measured at a number of different sustain frequencies. If the sustain frequency is very low like 1 kHz, then the temperature of the gas will be very close to the ambient temperature of the glass walls. This is true for most all gases since Figure 6.6 shows that even a low thermal conductivity gas like Xe reaches an equilibrium temperature after a few hundred microseconds. Once the velocity is measured at 1 kHz, the sustain frequency is then increased to the desired value, e.g. 50 kHz. Because of the dependence of velocity on temperature, the following relationship holds for the two velocities and temperatures:

$$\frac{T_H}{T_L} = \left(\frac{V_H}{V_L}\right)^2 \qquad (6.6)$$

where T_H and V_H are the temperature and velocity at the high sustain frequency, and T_L and V_L are for the low sustain frequency. T_L is assumed to be the ambient temperature of the glass panel. The velocities are not actually measured, but some convenient transit time which is proportional to the velocity. This might typically be the time for 10 round trip transists of the sound wave.

One would expect that a cell filled with xenon should show the largest temperature changes because of its poor heat conductivity and its intense discharge. The transit times were measured with 50 kHz and 1.5 kHz sustain frequencies. The results showed that the gas temperature at 50 kHz was 36°C above the temperature at 1.5 kHz. This was with 250 torr Xe and a 185 μm gap spacing. This is the same plasma cell used in Figures 6.4 through 6.7. Such a large temperature change is consistent with the ~10% density changes shown in Figure 6.5. Thus in the case of pure Xe, the effects of average gas temperature are significant and must be included in any theory of operation.

For more standard gas mixtures such as Ne + 0.1% Xe, the temperature change is much smaller and is not detectable with the sound velocity technique because of limited oscilloscope resolution. The resolution limits show that the temperature increase cannot be greater than 5°C. If one assumes that the density change such as shown in Figure 6.8 is completely due to a change in temperature at constant pressure, then the temperature change in Ne + 0.1% Xe at 500 torr and a gap spacing of 185 μm is 3.5°C. Thus for typically used gas mixtures in plasma display panels, the gas is always within a few degrees C of the ambient glass temperature. This is

not to say that the glass does not get well above the room ambient. It is well-known that a fully lit plasma panel may rise 10 or 15°C above ambient. However the gas temperature will always be within a few degrees C of this warmer glass ambient. Thus any model of Ne filled plasma panels can justifiably neglect the effects of neutral gas temperature change.

6.8 Electron Density Measurement

The laser interferometry technique seems to be an excellent way to measure the neutral atom density in the plasma display panel. However, these interferometry experiments were performed in hopes of measuring the electron density, a quantity much more important to the operation of the device. Since an electron density of 10^{12} cm^{-3} should give about a 10^{-2} Å phase change for this experimental setup, it is clear that the problem is not the signal to noise ratio of the system since, as shown in section 5.4, 10^{-5} Å phase changes are above the noise level of this system for reasonable integration times. Thus in theory, the electron density is measurable if the electron and neutral densities can be separated.

The standard technique for separating these two densities is to perform the measurement at two different laser wavelengths as discussed in section 6.5 [35]. From equation (6.4) it is desirable that the two wavelengths be as far apart as possible in order to maximize the difference of the resulting phase changes.

For signal to noise reasons discussed extensively in Chapter 5, an argon ion laser has been chosen for these experiments. For the available laser power the best choice is λ_1 = 5145 Å and λ_2 = 4579 Å. Unfortunately

these wavelengths are not very far apart. From the discussion of section 6.5, the neutral density term should be about 500 times larger than the electron density term of equation (6.4). Simple mathematics shows that in order to resolve an electron density change with a signal to noise ratio of one, the accuracy of the phase change measurement at each wavelength must be greater than 1 part in 10^3. This is virtually impossible to attain since most averaging instruments, such as boxcar integrators, only have a dynamic range of 10^3. Even if a suitable averaging instrument could be found, it would be extremely difficult to keep the interferometry system stable to 1 part in 10^3.

This great accuracy is required because of the large ratio between the neutral phase change and the electron phase change. One approach that gets around this problem is an attempt to cause an electron density to change in the panel without causing any neutral density perturbations. This technique relies on the ability to remove the electrons from the gas volume by placing appropriate voltage waveforms on the cell. As shown in Chapter 4, a significant change in sustain waveform has the effect of sweeping the plasma out of the volume. The desired signal is the change of phase due only to the removal of the electrons. After the sweep out pulse, all measured phase changes will be due to neutrals. In sustain cycles where no sweep out pulses occur, the phase changes will be due to both neutrals and electrons. By carefully subtracting the waveforms presented by these two types of sustain cycles, one can subtract out the neutral density changes and end up with only the electron density changes.

To perform this subtraction the equipment shown in Figure 6.9 was used. The delay line used was an Allen Avionics series HR, lumped constant delay line with 30 μs delay and 0.3 μs rise time. The sustain frequency was carefully adjusted so that one complete sustain cycle equaled the delay time of the delay line. Since the delay line attenuates the signal by about 8 db, a simple attenuator was used to balance the inputs to the differential amplifier. The RC filter takes out the frequency components that the delay line will not pass due to its limited rise time. This limited frequency response has a greater effect on attenuating the neutral atom phase changes than on the electron density phase changes since the electron density changes are much slower.

The technique was to use the sustain waveform shown in Figure 6.10. A perfect square wave sustainer was used in order to maintain the plasma for as long as possible. After a sufficiently long number of sustain cycles to insure that the discharge has stabilized, the premature fall of the sustain cycle is introduced to sweep out the plasma. For clarity, Figure 6.10 shows the expected electron density phase changes only. It must be remembered that the neutral density phase changes are superimposed on top of these electron phase changes. If the neutral density does not change due to the introduction of the sweep out pulse, then all of the neutral changes will be canceled our during the period of interest.

Thus assuming a perfect delay line, the electron density change due to the sweep out pulse should be easily observable. Unfortunately the delay line used here is by no means perfect. It introduces distortions on the order of a few percent. This is not enough to appreciably affect the

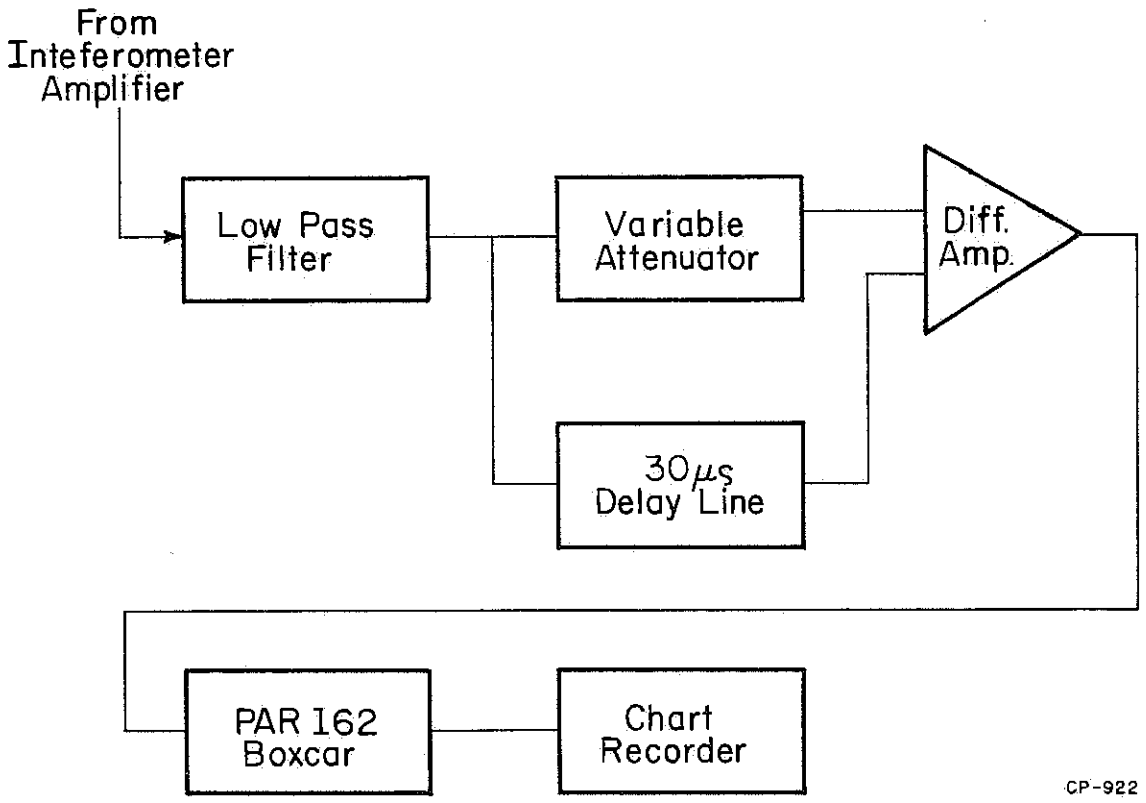

Figure 6.9. Experimental arrangement used to separate the neutral phase changes from the electron phase changes.

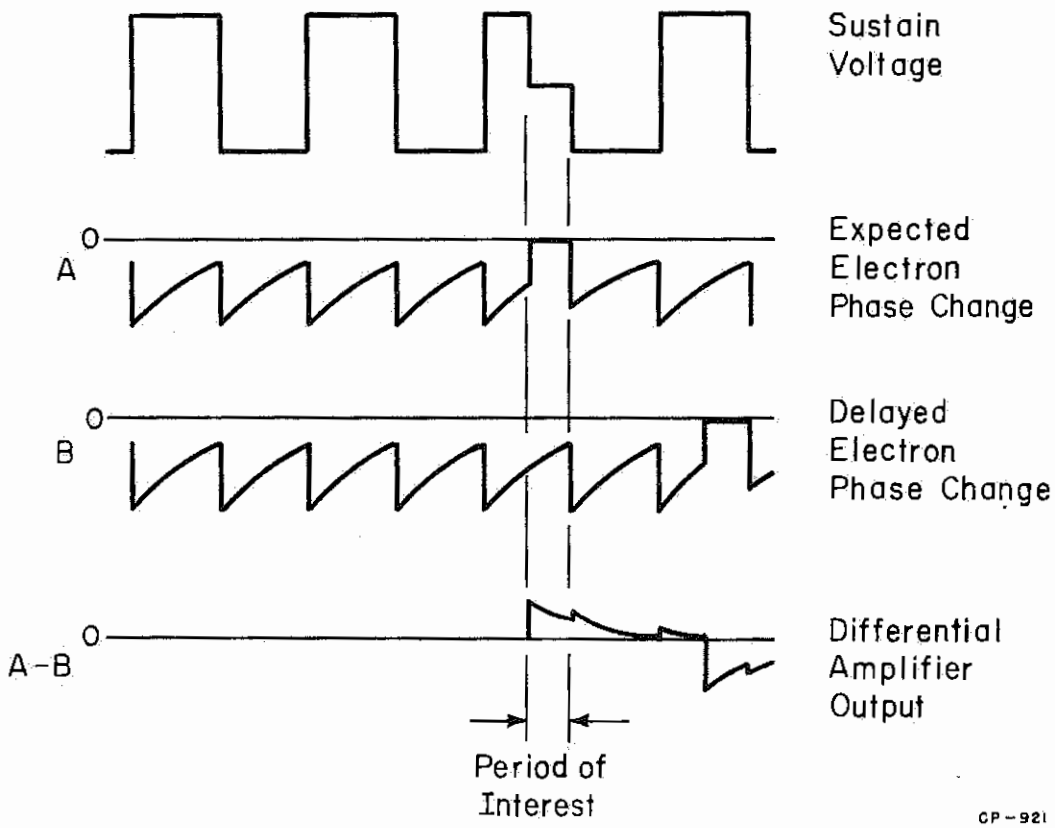

Figure 6.10. Diagram showing the various signals that produce the resultant electron phase change signal.

shape of the electron density curve, it however also changes the shape of the neutral density curve and thus the neutral changes do not cancel out in the differential amplifier. During the period of interest, the difference of the neutral density signal and the delayed distorted neutral density signal is a distorted neutral density signal that is still much greater than the expected electron density change. However this resultant distorted neutral signal is much smaller than the original undistorted neutral signal. Thus although the delay line does not solve the problem completely, it does decrease the neutral signal without decreasing the electron density signal, thus easing the dynamic range requirement on the averaging equipment. The boxcar integrator can again be used. For these experiments a P.A.R. 162 dual channel boxcar integrator was used. Since the delay line is made entirely of linear circuit elements, the distortion is primarily due to ringing and overshoot, thus it will be consistent from one discharge cycle to the next. The electron density change during the period of interest can be extracted from the distorted neutral signal by having one boxcar channel sample the period of interest, and having the second channel sample a period 30 μs before the period of interest. By subtracting the outputs of the two channels, one can cancel out the greatly distorted neutral changes and be left with only the electron density changes.

The above technique worked quite satisfactorily without limitation from dynamic range of the boxcar integrator. The noise limiting factors again became shot noise and laser plasma noise as discussed in Chapter 5. The output of the boxcar clearly shows the phase change due to the introduction of the sweep out pulse. The question that needs to be answered is:

is this phase change due to a decrease in electron density due to the sweep out mechanism, or is it due to a neutral density change similarly induced by the sweep out pulse? To answer this, the phase change data in various locations in the cell was measured for different sweep out pulse shapes in order to determine the characteristics of the sweep out mechanism. Also, two wavelength interferometry was used.

Figure 6.11 shows the typical phase changes in various regions of the plasma cell due to the sustain voltage fall. The index of refraction increases upward. At the fall, the field polarity in the gas volume reverses direction. Thus the cathode and anode functions of the two electrodes are exchanged. In Figure 6.11 the cathode trace refers to the polarity situation after the sustainer fall. The five traces show the changes at the cathode, 25 μm from the cathode, and so on to the bottom anode trace. The sustain fall seems to cause an index increase that is seen to be strongest at the anode. This soon gives way to a large decrease in index that lasts for at least 10 μs.

The complete interpretation of this data is not clear at this point. It seems reasonable to attribute the long lived decrease in index to a gas heating mechanism caused by the discharge activity that occurs when the sustain voltage falls. The fact that the index decrease is stronger for the traces near the new cathode confirms this theory. For the long decrease to be due to electrons, the electron density would have to increase considerably due to the sign of the electron term in equation (6.4). However from the capacitance and microwave measurements, this clearly cannot be true. Thus the neutral density decrease is the only possibility.

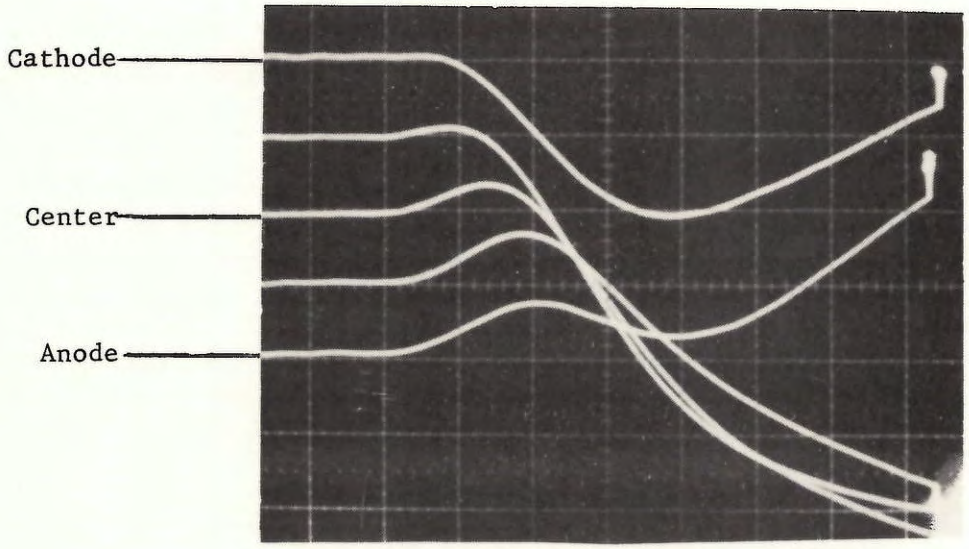

Figure 6.11. Phase changes due to the fall of the sustain pulse for various positions along the gap. The index of refraction increases upward. The horizontal scale is 1 μs per division. The vertical scale is 0.1 Å per division. The integration time constant for this data was about 1 μ s. Thus the phase change behavior shown here is smoothed out considerably.

The short increase in index, shortly after the sustain fall is much more difficult to assess. There is a reasonable possibility that it is due to electron density changes. When the electrons are swept out, their density decreases so that from equation (6.4), the index of refraction should increase. On the other hand, this increase could be due to a neutral density increase. If the density decreases due to the heating in the cathode region, then the atoms leaving the cathode region may go toward the anode and cause the observed increase. There are also other possibilities that are too detailed to mention here. However, it is clear that the only way to resolve this problem is to perform the two wavelength experiment. If the index rise is due to electrons only, it should be clearly resolvable with little or no interference from the neutrals.

Unfortunately, significant two wavelength data had not been obtained at the end of the experimental period. For signal to noise reasons, the most intense Ar^+ laser lines at 5145 Å and 4880 Å were used. From equation (6.4) the ratio of the electron phase changes to the neutral phase changes should change by about 10% between the two wavelengths. In spite of considerable effort, the accuracy of the measurements could not be maintained to greater than 10%. This problem appeared to be primarily due to the inability to position the laser beam to the same spot in the cell when the laser prism was moved to change wavelengths. Thus a better positioning system or a laser with a wider wavelength separation is needed.

If the index increase is totally due to electrons, then a 0.1 Å increase corresponds to about a 10^{13} cm^{-3} plasma density. This is about the value suggested by the computer calculations shown in Figure 2.9.

CHAPTER 7

CONCLUSION

A number of significant achievements have been presented in this thesis. A computer simulation has suggested the existence of a plasma that remains in the gas volume for many microseconds after the discharge peak. RF capacitance and microwave transmission experiments have demonstrated plasma lifetimes as long as 100 μs. The plasma decay can be accelerated by the application of small RF or microwave signals. More dramatic is the plasma sweep out effect observed when the sustain voltage makes a sudden amplitude change. The existence of this plasma has important consequences with regard to the memory margin and speed of operation of this device.

A major step has been taken in the theoretical understanding of the operation of the device. With the aid of a computer simulation, the final theoretical links have been found that provide an explanation of the memory characteristics of this device in terms of basic physical laws. Two independent physical mechanisms have been found that will provide memory. One is strongly dependent on the sustain waveform shape, and the other dependent on the value of the product of the gas pressure and the discharge gap spacing.

An important spinoff of this research has been the development of a very sensitive optical interferometry system that is capable of measuring phase changes smaller than 10^{-5} Å. This result is better than any known, previously published result. This system is extremely simple and requires no complex alignment steps.

This interferometer has been used to demonstrate the existence of strong sound waves that are generated by the intense discharge activity in the cathode region. These waves propagate back and forth across the gas volume for many microseconds after the discharge. Measurement of the sound velocity has aided in determining the absolute temperature of the gas in the cell. In typical gas mixtures it is no more than a few degrees centigrade above the glass wall temperature.

Unfortunately, the sound waves cause very large index of refraction changes that obscure the small changes due to the plasma. Although some clever techniques may have circumvented the sound wave noise problem, it is not possible, at the end of this study, to say with reasonable certainty that an index change due to the presence of a plasma has been observed.

Although a large number of significant results were achieved here, a full understanding of the plasma panel discharge dynamics is far from complete. The time when a design engineer can sit down and prescribe a panel geometry, sustain waveform and gas mixture to give him a desired electric and optical characteristic is very far off. However the results presented here should provide useful guides to direct further empirical work. For instance, from what was learned in Chapter 3, it is clear that the square wave sustain wave is inferior to the non-square wave with regard to memory margin. It is not at all clear that the waveform shown in Figure 3.8 will give the best margin achievable. Thus other waveforms must be tried with the guidance of the theories and experiments presented here. With the proper design parameters, it may be possible to achieve the ideal charge transfer curve, shown in Figure 7.1, that will allow the maximum possible memory margin.

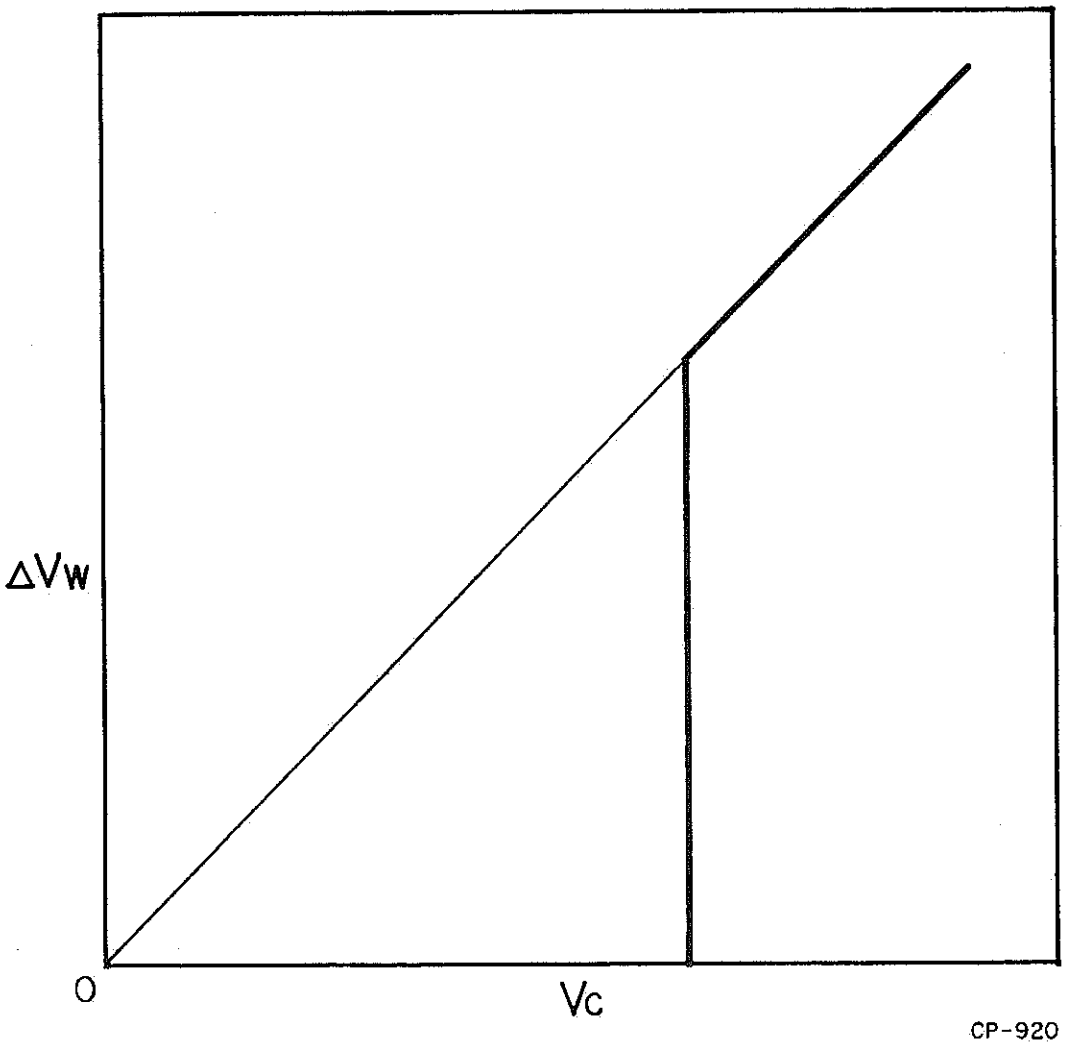

Figure 7.1. Ideal charge transfer curve.

The memory margins existing in present day panels are generally regarded as barely adequate. Any improvement would have the major benefit of lowering cost in a number of areas. Larger memory margins would increase panel yield, increase reliability, and thus lower maintenance costs, increase panel lifetime, and relax tight drive electronics specifications. With all of these potential benefits, it is surprising that many of the major corporations marketing plasma display panels do not have major research programs devoted to an understanding of the device physics.

Besides increasing memory margin, the discharge physics studies may play a major role in the reduction of drive circuitry costs. Recently, Schermerhorn [47] has shown that the plasma display cell can be used as a four input logic element that is capable of performing some of the decoding normally done by circuitry. He has demonstrated a large area panel that requires only 96 electrical connections instead of the usual number of 1024. This is sure to have an important impact in an industry where electrical connections are rapidly becoming the most expensive circuit elements. Unfortunately, Schermerhorn's technique will be useful only for a limited number of display applications because of slow update rates. However with knowledge of the discharge physics, there is a good chance that the gas discharge can be made to act as a logic element in other ways that will allow the normal high update rate.

In conclusion, a number of important advances in understanding the discharge dynamics of the plasma display panel have been made in this thesis. These advances represent only a start. Many of the experiments and theories

described here deserve a considerable amount of further development. Such research has a very encouraging potential for increasing device performance and reducing cost.

REFERENCES

1. H. J. Hoehn and R. A. Martel, "A 60 Line Per Inch Plasma DisplayPanel," IEEE Trans. on Electron Devices, Vol. ED-18, No. 9, p. 659, September 1971.

2. D. L. Bitzer and H. G. Slottow, "The Plasma Display Panel - A Digitally Addressable Display with Inherent Memory," Proc. of the Fall Joint Computer Conference, November 1966.

3. D. L. Bitzer and H. G. Slottow, "Principles and Applications of the Plasma Display Panel," Proc. of the O.A.R. Research Applications Conference, Office of Aerospace Research, Arlington, Virginia, March 1968 (Also appears in Proc. of the 1968 Micro-electronics Symposium, IEEE, St. Louis, Mo.)

4. R. L. Johnson, D. L. Bitzer, and H. G. Slottow, "The Device Characteristics of the Plasma Display Element," IEEE Trans. on Electron Devices, Vol. ED-18, No. 9, p. 642, September 1971.

5. R. H. Wilson, "A Capacitively Coupled Bistable Gas Discharge Cell for Computer Controlled Displays," Report R-303, Coordinated Science Laboratory, University of Illinois, Urbana, Illinois, June 1966.

6. B. M. Arora, "The Influence of Gas Composition and of Signal Waveforms on the Properties of the Plasma Display," Report R-377, Coordinated Science Laboratory, University of Illinois, Urbana, Illinois, May 1968.

7. H. Veron and C. C. Wang, "AC Electrical Breakdown of Neon with External Electrodes," J. Appl. Phys., Vol. 43, p. 2664 (1972).

8. A. L. Ward, "Calculations of Cathode-Fall Characteristics," J. Appl. Phys., Vol. 33, p. 2789 (1962).

9. A. L. Ward, "Effect of Space Charge in Cold Cathode Gas Discharge," Physical Review, Vol. 112, No. 6, pp. 1852-1857, December 1958.

10. A. L. Ward, "Effect of Space Charge Upon the Transport of Charged Carriers, J. Appl. Phys., Vol. 35, No. 3, part 1, pp. 469-474, March 1964.

11. A. L. Ward, "Ionization, Diffusion, and Drift Velocities in a Pulsed Townsend Discharge," J. Appl. Phys., Vol. 36, No. 4, pp. 1291-1294, April 1965.

12. W. Börsch-Supan and H. Oser, "Numerical Computation of the Temporal Development of Currents in a Gas Discharge Tube," J. of Research of NBS, Vol. 67B, No. 1, pp. 41-63, January 1963.

13. F. M. Lay, C. K. Chu, and P. H. Haberland, "Simulation of Cyclic Operation of Gas Panel Device," IBM J. Res. Develop. Vol. 18, p. 244 (1974).

14. C. Lanza, "A One-Dimensional Numerical Analysis for an AC Gas Display Panel," IBM J. Res. Develop. Vol. 18, p. 232 (1974).

15. C. Lanza, W. E. Howard, and O. Sani, "Numerical Simulation of AC Gas Display Discharges," Presented at 1974 Gaseous Electronics Conference, Houston, Texas, abstract in Bull. Am. Phys. Soc. Series II, Vol. 20, No. 2, p. 255.

16. J. D. Cobine, Gaseous Conductors (Dover Publications, Inc., New York, 1958).

17. H. Raether, Electron Avalanches and Breakdown in Gases (Butterworth & Co. Ltd., London, 1964).

18. P. L. Auer, "Transient Analysis of the Townsend Discharge," Physical Review, Vol. 111, No. 3, pp. 671-682, August 1958.

19. J. M. Anderson, "Electrodeless Discharge Modes in Neon-Nitrogen Mixture with Application to the Plasma Display Panel," Appl. Phys. Letters, Vol. 16, p. 531 (1970).

20. B. M. Arora and H. G. Slottow, Coordinated Science Laboratory, University of Illinois, Urbana, Illinois, Progress Report for March-August 1968, pp. 217-227.

21. H. G. Slottow and W. D. Petty, "Stability of Discharge Series in the Plasma Display Panel," IEEE Trans. on Electron Devices, Vol. ED-18, No. 9, p. 650, September 1971.

22. Data Sheet for Digivue Model 512-60 Display/Memory Unit, Owens-Illinois, Toledo, Ohio.

23. C. Lanza, private communication, April 1975.

24. J. K. Theobald, "Investigation of Back Diffusion of Photoelectrons in Various Standard Gases as It Affects Secondary Electron Emission Coefficients," J. Appl. Phys., Vol. 24, No. 2, pp. 123-127, February 1953.

25. F. M. Lay and C. K. Chu, "Simulation of a Transient DC Breakdown in a Penning Mixture Between Two Closely Spaced Parallel Electrodes," J. Appl. Phys., Vol. 44, No. 9, pp. 4008-4012, September 1973.

26. W. E. Coleman, "AC-Coupled Gas-Discharge Display Multiplexes Digits with Message Blocks," Electronics, pp. 123-128, January 10, 1974.

27. J. D. Schermerhorn, private communication, December 1973.

28. L. M. Jones, "A Study of Parallel Self-Shift Techniques in High Density Plasma Display/Memory Panels," M.S. thesis, University of Illinois, Urbana, Illinois, 1973.

29. L. M. Jones and R. L. Johnson, "A Parallel Self-Shift Technique for Plasma Display/Memory Panels," to be published in IEEE Trans. on Electron Devices, May 1975.

30. G. S. Weikart, private communication, November 1974.

31. R. H. Huddlestone and S. L. Leonard, Plasma Diagnostic Techniques (Academic Press, New York, 1965).

32. C. L. Chen, "Electron Collisions in Neon Plasma," Physical Review, Vol. 135, No. 3A, p. A627, 1964.

33. L. F. Weber and R. L. Johnson, "Direct Electrical Readout from Plasma Display/Memory Panels," IEEE Trans. on Electron Devices, Vol. ED-20, No. 11, pp. 1082-1091, 1973.

34. R. L. Johnson and W. J. Coates, Jr., "Optical Readout from Plasma Display/Memory Panels," IEEE Trans. on Electron Devices, Vol. ED-20, No. 1, p. 28, 1973.

35. W. B. Johnson, "Laser Interferometry and Photon Scattering in Plasma Diagnostics," IEEE Transactions on Antennas and Propagation, Vol. AP-15, No. 1, pp. 152-162, January 1967.

36. R. Balhorn, H. Kunzman, and F. Lebowsky, "Frequency Stabilization of Internal Mirror Helium-Neon Lasers," Applied Optics, Vol. 11, No. 4, p. 742, April 1972.

37. S. K. Gordon and Stephen F. Jacobs, "Modification of Inexpensive Multimode Lasers to Produce a Stabilized Single Frequency Beam," Applied Optics, Vol. 13, No. 2, p. 231, February 1974.

38. G. E. Moss, L. R. Miller, and R. L. Forward, "Photon Noise Limited Laser Transducer for Gravitational Antenna," Applied Optics, Vol. 10, No. 11, p. 2495, November 1971.

39. American Institute of Physics Handbook, D. E. Gray, ed., 3rd ed., McGraw-Hill, New York, 1972.

40. V. J. Fowler and J. Schlafer, "A Survey of Laser Beam Deflection Techniques," Proc. IEEE, Vol. 54, p. 1437, 1966.

41. H. Boersch, H. J. Eichler, M. Pfundstein, and W. Weisemann, "Measurement of Length Shifts Down to 10^{-5} Å with a Three-Mode Laser," IEEE Journal of Quantum Electronics, Vol. QE-10, No. 6, p. 501, June 1974.

42. J. Berlande, P. D. Goldan, and L. Goldstein, "Formation and Propagation of a Pressure Wave in a Weakly Ionized Gas," Applied Physics Letters, Vol. 5, No. 3., p. 51, August 1964.

43. J. B. Gerardo, J. T. Verdeyen, and M. A. Gusinow, "Spatially and Temporally Resolved Electron and Atom Concentration in an Afterglow Gas Discharge," Journal of Applied Physics, Vol. 36, No. 11, p. 3526, November 1965.

44. H. Joseph Hoehn and Richard A. Martel, "Recent Developments in Three-Color Plasma Display Panels," IEEE Transactions on Electron Devices, Vol. ED-20, No. 11, pp. 1078-1081, November 1973.

45. C. Cuthbertson and M. Cuthbertson, "The Refraction and Dispersion of Argon, and Redetermination of the Dispersion of Helium, Neon, Krypton, and Xenon," Proc. of Royal Society of London, Vol. A 84, p. 13 (1910).

46. C. Cuthbertson and M. Cuthbertson, "The Refraction and Dispersion of Neon and Helium," Proc. of Royal Society of London, Vol. A 135, pp. 40-47 (1932).

47. J. D. Schermerhorn, "Internal Random Access Address Decoding in an AC Plasma Display Panel," 1974 Digest of Papers, SID International Symposium, San Diego, CA, May 1974.

VITA

Larry Francis Weber was born in Anchorage, Alaska, on July 9, 1947. He graduated in 1965 from Joliet Catholic High School in Joliet, Illinois. He received the B.S. degree with highest honors and the M.S. degree, both in Electrical Engineering from the University of Illinois at Urbana-Champaign in 1969, and 1971, respectively. He is a member of Tau Beta Pi and Eta Kappa Nu, and received a University of Illinois Fellowship in 1969.

Mr. Weber has been employed as a research assistant at the Computer-based Education Research Laboratory and the Coordinated Science Laboratory at the University of Illinois since 1969. During this period he has been involved with research on the PLATO teaching system and on the AC plasma display panel.

Publications:

1. L. F. Weber, "Blind Student Power," Technograph, University of Illinois, October 1968, pp. 17-20.

2. L. F. Weber, "Optical Write-In Techniques for the Plasma Display Panel," Report R-510, Coordinated Science Laboratory, University of Illinois, May 1971, also appears as a M.S. Thesis.

3. L. F. Weber, "Optical Write-In for the Plasma Display Panel," IEEE Transactions on Electron Devices, Vol. ED-18, September 1971, pp. 664-672.

4. W. Coates, R. L. Johnson, and L. F. Weber, "Techniques for Optical and Electrical Data Sensing in Plasma Display/Memory Panels," presented at the 1971 IEEE International Electron Devices Meeting, October 21, 1971.

5. L. F. Weber and R. L. Johnson, "Simple Access Circuitry for Electrical Data Sensing of Plasma Display/Memory Panels," presented at the 1972 Society for Information Display International Symposium, June 1972, Digest of Technical Papers, Vol. III, pp. 136-137.

6. R. L. Johnson and L. F. Weber, "Graphic System Applications of Plasma Display/Memory Devices with Direct Electrical Readout," presented at the 1973 Society for Information Display International Symposium, May 1973, Digest of Technical Papers, Vol. IV, pp. 18-19.

7. L. F. Weber and R. L. Johnson, "Direct Electrical Readout from Plasma Display/Memory Panels," IEEE Transactions on Electron Devices, Vol. ED-20, No. 11, November 1973, pp. 1082-1091.

8. L. F. Weber, "Discharge Physics Studies for the AC Plasma Display Panel," 1974 Conference on Display Devices and Systems, 74CH0892-OED, Conference Record, pp. 20-26.